

Dispersion and phase control in microresonator frequency combs

**Dissertation
zur Erlangung des Doktorgrades
an der Fakultät für Mathematik, Informatik und Naturwissenschaften
Fachbereich Physik
der Universität Hamburg**

**vorgelegt von
Thibault Wildi**

**Hamburg
2024**

Gutachter der Dissertation:

Prof. Dr. Tobias Herr
Prof. Dr. Franz X. Kärtner

Zusammensetzung der Prüfungskommission:

Prof. Dr. Tobias Herr
Prof. Dr. Franz X. Kärtner
Prof. Dr. Ralf Riedinger
Dr. Christoph Heyl
Prof. Dr. Daniela Pfannkuche

Vorsitzende/r der Prüfungskommission:

Prof. Dr. Daniela Pfannkuche

Datum der Disputation:

06.02.2025

Vorsitzender Fach-Promotionsausschusses PHYSIK:

Prof. Dr. Markus Drescher

Leiter des Fachbereichs PHYSIK:

Prof. Dr. Wolfgang J. Parak

Dekan der Fakultät MIN:

Prof. Dr.-Ing. Norbert Ritter

Declaration on oath

I hereby declare and affirm that this doctoral dissertation is my own work and that I have not used any aids and sources other than those indicated.

Electronic resources based on generative artificial intelligence (gAI) were used in the course of writing this dissertation. I confirm that my own work was the main and value-adding contribution and that complete documentation of all resources used is available in accordance with good scientific practice. I am responsible for any erroneous or distorted content, incorrect references, violations of data protection and copyright law or plagiarism that may have been generated by the gAI.

Hamburg, 10.10.2024

A handwritten signature in blue ink is written over a horizontal line. The signature is stylized and appears to be 'M. P. ...'.



Acknowledgements

First and foremost, I want to thank my thesis supervisor, Prof. Tobias Herr, for providing me with such an exceptional opportunity. It was his enthusiasm for nonlinear photonics and microresonator frequency combs, in particular, that initially sparked my interest back at CSEM. His excitement was contagious, and I was hooked — little did I know that it would lead all the way to Hamburg. Throughout my PhD, I was able to benefit from his advice, guidance, constant availability, and extensive knowledge. His unwavering optimism and scientific integrity have been a source of inspiration. Beyond academic work, I enjoyed the occasional morning runs around the DESY campus.

I met Thibault Voumard on my very first day back at CSEM. I had started there only a handful of days after him — an (unfortunate) delay that would see me labeled "no. 2" from there onward in a vain attempt to avoid the many *qui pro quos* that have since ensued. Over the years, we've shared two (and $\frac{3}{4}$) labs, four offices, multiple publications, and countless hours both in and outside of work. A skilled theorist and talented experimentalist, Thibault has carried and supported this work from the bottom up. I always enjoyed our discussions, bouncing ideas off each other, troubleshooting our experiments, and exploring various aspects of our research together.

I am particularly grateful to Alexander Ulanov, who joined the group two years into my thesis, bumping up the microcomb team to a grand total of 2 people. I very much enjoyed our time in the lab together, collaborating on joint experiences, which were some of the highlights of my PhD. I like to think we complement each other well and make for an efficient team.

I want to thank Bastian Ruhnke, who significantly contributed to the development of our silicon nitride photonic chips, particularly in designing and developing pulley couplers for our microring resonators. He also taught me most of my tenuous football knowledge, enlightened me about northern German culture, and provided valuable comments on this thesis. I wish him the best of luck in his PhD endeavors.

I want to express my gratitude to my colleagues, Markus Ludwig, Mahmoud Gaafar, and Weichen Fan. Together, we took on the fun but challenging task of assembling a lab from scratch. The many discussions, collaborations, and shared experiences have made this thesis a rewarding and enjoyable experience. Your diverse expertise and assistance have greatly contributed to the success of this work.

I want to thank past and present members of the Ultrafast Optics and X-rays Group, including Felix Ritzkowsky, Maximilian Kubullek, Fabian Scheiba, Miguel Angel Silva Toledo, Roland Mainz, Giulio Rossi, Erwin Vargas, Milan Sinobad, Tobias Kroh among others — a continuous stream of engaging discussions and coffee made for a dynamic and stimulating working environment.

In no particular order, I would also like to thank Nicolas Englebert for our collaboration on soliton sideband injection; Erwan Lucas and the Microphotonics Research Group at the Max Planck Institute for the Science of Light in Erlangen, Germany, including Prof. Pascal Del’Haye, Toby Bi, Lewis Hill, and Shuangyou Zhang for insightful discussions; Victor Brasch who taught me most of the experimental methods used in this work; Maxim Karpov and John Jost from Enlightra for works related to laser self-injection locking (special thanks to Maxim for his advice on the characterization of solitons in Fabry-Perot microresonators); as well as Alexander Yu. Petrov and Hendrik Preuß for valuable discussion on photonic crystal design and analytical modeling.

From Ligentec, I thank Anton Stroganov, Henry Francis and Stijn Cuyvers. Their assistance, feedback, and advice were invaluable in the development of our silicon nitride chips. Their patience was especially appreciated during our (consistently eleventh-hour) submissions.

I also wish to thank Uta Freydanck for her administrative support, continuously ensuring everything ran smoothly.

I want to thank Will Curwen and Laetitia Martel for their valuable work during their internships within our group. I greatly appreciate their assistance in the characterization of silicon nitride resonators and in building our electro-optic comb.

I would also like to acknowledge the Maxwell computational resources operated at DESY, which have been instrumental for the simulations and computational work.

Finalement, j’aimerais remercier ma famille, mes parents, mon frère ainsi que Sonja pour leur soutien indéfectible au cours de ces dernières années.

Hamburg, 10.10.2024

T. Wildi

Abstract

Since their inception a little more than fifteen years ago, optical frequency combs based on Kerr-nonlinearity inside optical microresonators have enabled significant advancements in diverse applications, ranging from precision measurements in laboratory settings to the development of compact sources for telecommunications and laser ranging. Relying on high finesse dielectric microresonators, these so-called *microcombs* leverage the combination of a small mode area and resonant enhancement with strong Kerr optical nonlinearity to achieve efficient nonlinear frequency conversion with minimal power requirements. A particularly attractive type of such comb is based on dissipative Kerr solitons (DKS), where stationary solitonic attractors form inside the resonator, resulting in a stable, low-noise, high repetition rate optical frequency comb. Typically excited from a continuous wave pump laser forming the central comb tooth, such *soliton microcombs* rely on a careful double equilibrium between Kerr nonlinearity and dispersion on one hand and gain and loss on the other. Combining a small footprint with low power consumption and the ability to be produced at scale, integrated DKS sources have risen to the forefront of photonics research over the last decade. However, key challenges are yet to be addressed, including the extension of microcomb spectra to new wavelength ranges, improved comb actuation and control, robust initiation and operation, and the stabilization of comb lines.

In this thesis, we start by exploring the use of sub-wavelength nanoscale structures to address some of these challenges. A major prerequisite — and hence limitation — for generating soliton microcombs is that they require anomalous dispersion, which is only achievable within limited wavelength ranges due to material and waveguide properties. To overcome this limitation, we develop on-chip standing-wave cavities supporting DKSs. Based on carefully crafted uniaxial photonic crystal reflectors (PCR) with ultra-high reflectivity, these Fabry-Perot microresonators attain Q-factors on par with conventional ring-type microresonators. Critically, by controlling the phase of the reflected light, the PCR provides a precise mechanism for managing the dispersion

required for DKS formation. By decoupling dispersion control from the underlying waveguide geometry and material, this approach could extend DKS sources into new wavelength ranges and material platforms, complementing methods developed for ring-type devices. Beyond DKS, such standing-wave cavities introduce a novel topology that opens avenues for the exploration of new physics, such as Nyquist solitons and filter-driven pulse formation.

The versatility of DKS sources stems from their comb spectra, which consist of a set of equidistant optical lines. The frequency of these lines is defined by the comb's two degrees of freedom — namely, the repetition rate and offset frequencies — which connect the microwave and optical domains. In the second part of this thesis, we study *sideband injection locking*, an all-optical technique for precisely controlling these parameters. This method involves injecting a secondary continuous-wave laser into the resonator cavity, causing one of the comb lines to lock onto it. Relying on broadband characterization, we analyze the locking dynamics and derive analytic scaling laws for the comb's locking range and repetition rate control. Our findings show excellent agreement between theoretical predictions and experimental results and may inform the design of sideband injection-locked parametrically generated frequency combs. As an example, we demonstrate the optical frequency division of a >10 THz span, resulting in a drastic reduction of the repetition-rate phase-noise, 30 dB below that of a free-running system. This approach to microcomb control and actuation presents opportunities for low-noise microwave generation, compact optical clocks with simplified locking schemes, and, more generally, all-optically stabilized frequency combs from Kerr-nonlinear resonators.

Pushing our exploration of comb control techniques further, we demonstrate full-phase stabilization of a self-injection-locked soliton microcomb. Self-injection-locked (SIL) microcombs harness optical feedback from a high-Q microresonator to the driving laser to control the pump-to-cavity detuning, addressing one of the major challenges in soliton microcombs generation. This method allows the use of chip-scale diode lasers instead of complex table-top sources, significantly reducing operational complexity, system footprint, and cost. However, unlike conventional driving schemes, SIL-based systems do not allow independent control of the pump laser frequency and power — parameters typically used to stabilize the comb's degrees of freedom. In the final chapter of this thesis, we show that full phase stabilization of SIL microcombs is nevertheless possible by using an integrated electric microheater in addition to the laser pump current. We achieve an effective locking bandwidth of more than 100 kHz, enabling robust phase-locking of the repetition rate and offset frequencies to external

references. Importantly, our millimeter-scale system does not employ electro-optic, acousto-optic, or piezo-electric actuation. Instead, we rely solely on low-voltage (below 1.5V) CMOS-compatible control signals, meeting a critical requirement of chip-integrated technologies. Our results constitute the first demonstration of a chip-scale microresonator source for phase-coherent frequency metrology.

Zusammenfassung

Seit ihrer Einführung vor etwas mehr als fünfzehn Jahren haben optische Frequenzkämme, die auf Kerr-Nichtlinearität in optischen Mikroresonatoren basieren, bedeutende Fortschritte in verschiedenen Anwendungsbereichen ermöglicht, die von Präzisionsmessungen unter Laborbedingungen bis hin zur Entwicklung kompakter Quellen für Telekommunikation und schneller Entfernungsmessung reichen. Diese sogenannten *Mikrokämme* nutzen die große Finesse dielektrischer Mikroresonatoren und kombinieren einen kleinen Modenquerschnitt mit resonanter Verstärkung und starker optischer Kerr-Nichtlinearität, um eine effiziente nichtlineare Frequenzumwandlung bei minimalem Leistungsbedarf zu erreichen. Ein besonders attraktiver Typ solcher Kämme basiert auf dissipativen Kerr-Solitonen (DKS), bei denen sich stationäre Soliton-Attraktoren innerhalb des Mikroresonators bilden, was zu einem stabilen und rauscharmen optischen Frequenzkamm mit hoher Repetitionsrate führt. Meistens angetrieben von einem monochromatischen Pump Laser, der den zentralen "Kammzahn" bildet, basieren solche *Soliton-Mikrokämme* auf einem doppelten Gleichgewicht zwischen Kerr-Nichtlinearität und Dispersion einerseits und nichtlinearer Verstärkung und Verlust andererseits. Wegen ihrer geringen Größe, ihres niedrigen Energieverbrauchs und der Möglichkeit zur Massenproduktion sind integrierte DKS-Quellen in den letzten zehn Jahren in den Vordergrund der Forschung in der Photonik gerückt. Trotzdem bestehen weiterhin zentrale Herausforderungen, darunter die Erweiterung der Mikrokammspektren auf neue Wellenlängenbereiche, sowie zuverlässige Erzeugung, Betrieb und Stabilisierung der Kämme.

Diese Dissertation beschäftigt sich zunächst mit der Untersuchung von subwellenlängen nanoskaligen Strukturen, um zentrale Herausforderungen der Mikrokammetechnologie zu überwinden: Eine wesentliche Voraussetzung — und somit Einschränkung — für die Erzeugung von Soliton-Mikrokämmen ist, dass sie anomale Dispersion erfordern, die aufgrund der Material- und Wellenleiter-Eigenschaften nur innerhalb begrenzter Wellenlängenbereiche erreichbar ist. Um diese Einschränkung zu überwin-

den, entwickeln wir Chip-integrierte Fabry-Pérot-Mikroresonatoren, die DKS ermöglichen. Basierend auf sorgfältig gestalteten uniaxialen photonischen Kristallreflektoren (PCR) mit extrem hoher Reflektivität erreichen diese Fabry-Pérot-Mikroresonatoren Güten, die mit herkömmlichen ringförmigen Mikroresonatoren vergleichbar sind. Durch Kontrolle der Phase des reflektierten Lichts bieten PCR eine präzise Kontrolle der erforderlichen Dispersion. Indem die Dispersion von Wellenleitergeometrie und -material entkoppelt wird, zeigt unsere Arbeit einen neuen Ansatz komplementär zu Ring-Mikroresonatoren auf, der es ermöglicht DKS-Quellen auf neue Wellenlängenbereiche und Materialien auszudehnen. Solche Fabry-Pérot-Mikroresonatoren können möglicherweise in der Zukunft neuartige physikalische Phänomene wie Nyquist-Solitonen und filtergetriebene Pulsbildung ermöglicht.

Die Vielseitigkeit von DKS-Quellen liegt in ihren Kamm-Spektren, die aus einem Satz äquidistanter optischer Linien bestehen. Die Frequenz dieser Linien wird durch zwei Freiheitsgrade des Kamms — die Repetitionsrate und die Versatzfrequenz — definiert, die Mikrowellen und optische Wellenlängen verknüpfen. Im zweiten Teil dieser Arbeit untersuchen wir *Seitenband-Injektionsstabilisierung*, eine rein optische Technik zur präzisen Steuerung dieser Parameter. Diese Methode beinhaltet das Einkoppeln eines sekundären monochromatischen Pumpasers in die Resonatorhöhle, wodurch eine der Kammlinien auf dessen Wellenlänge stabilisiert wird. Mittels Breitbandcharakterisierung analysieren wir die Stabilisierungsdynamik und leiten analytische Skalierungsgesetze für den Stabilisierungsbereich des Kamms und die Steuerung der Repetitionsrate ab. Unsere Ergebnisse zeigen eine ausgezeichnete Übereinstimmung zwischen theoretischen Vorhersagen und experimentellen Ergebnissen und könnten das Design von Seitenband-injektionsstabilisierten parametrisch generierten Frequenzkämmen verbessern. Als Beispiel zeigen wir die optische Frequenzteilung einer Spanne von über 10 THz, was zu einer drastischen Reduktion des Repetitionsratenrauschens um 30 dB im Vergleich zu einem nicht stabilisierten System führt. Dieser Ansatz zur Kammsteuerung und -regelung bietet Möglichkeiten für rauscharme Mikrowellenerzeugung, für kompakte optische Uhren mit vereinfachten Stabilisierungsverfahren und generell für optisch stabilisierte Frequenzkämme in Resonatoren mit Kerr-Nichtlinearität.

In einer vertiefenden Untersuchung der Kammsteuerungstechniken, demonstrieren wir die vollständige Phasenstabilisierung eines selbstinjektionsstabilisierten Soliton-Mikrokamms. Selbstinjektionsstabilisierte (SIL) Mikrokämme nutzen die optische Rückkopplung eines Mikroresonators hoher Güte zum Pumpaser, um die Verstimmung zwischen Laser und Resonator zu kontrollieren und damit eine der großen Herausforderungen bei der Erzeugung von Soliton-Mikrokämmen zu bewältigen. Diese Metho-

de ermöglicht den Einsatz von Diodenlasern mit Chipgröße anstelle komplexer großer Quellen und reduziert sowohl die Komplexität der Bedienung als auch den Platzbedarf und die Kosten der Mikrokammsysteme erheblich. Im Gegensatz zu herkömmlichen Schemata bieten SIL-basierte Systeme jedoch keine unabhängige Steuerung der Frequenz und Leistung des treibenden Lasers — Parameter, die typischerweise zur Stabilisierung der Freiheitsgrade des Kamms verwendet werden. Im letzten Kapitel dieser Arbeit zeigen wir, dass eine vollständige Phasenstabilisierung von SIL-Mikrokämmen dennoch möglich ist, indem wir zusätzlich zum Laserpumpstrom eine integrierte elektrische Mikroheizung verwenden. Wir erreichen eine effektive Stabilisierungsbandbreite von über 100 kHz, die eine robuste Phasenstabilisierung der Repetitionsrate und Versatzfrequenz gegenüber externen Referenzen ermöglicht. Hervorzuheben ist, dass unser Millimeter großes System keine elektro-optische, akusto-optische oder piezoelektrische Regelung verwendet. Stattdessen verwenden wir ausschließlich CMOS-kompatible Steuersignale niedriger Spannung (unter 1.5 V), was eine entscheidende Anforderung für chipintegrierte Technologien erfüllt. Unsere Ergebnisse stellen die erste Demonstration einer chip-integrierten Mikroresonatorquelle für phasenkohärente Frequenzmetrologie dar.



List of publications

Main publications

1. **Wildi, T.**, Gaafar, M. A., Voumard, T., Ludwig, M. & Herr, T. Dissipative Kerr Solitons in Integrated Fabry–Perot Microresonators. *Optica* **10**, 650–656. ISSN: 2334-2536 (June 2023).
2. **Wildi, T.**, Ulanov, A., Englebert, N., Voumard, T. & Herr, T. Sideband Injection Locking in Microresonator Frequency Combs. *APL Photonics* **8**, 120801. ISSN: 2378-0967 (Dec. 2023).
3. **Wildi, T.***, Ulanov, A. *, Voumard, T., Ruhnke, B. & Herr, T. Phase-Stabilised Self-Injection-Locked Microcomb. *Nature Communications* **15**, 7030. ISSN: 2041-1723 (Aug. 2024).

Additional contributions

1. Voumard, T. *, **Wildi, T.***, Brasch, V., Álvarez, R. G., Ogando, G. V. & Herr, T. AI-enabled Real-Time Dual-Comb Molecular Fingerprint Imaging. *Optics Letters* **45**, 6583–6586. ISSN: 1539-4794 (Dec. 2020).
2. **Wildi, T.***, Voumard, T. *, Brasch, V., Yilmaz, G. & Herr, T. Photo-Acoustic Dual-Frequency Comb Spectroscopy. *Nature Communications* **11**, 4164. ISSN: 2041-1723 (Aug. 2020).
3. Charczun, D., Nishiyama, A., Kowzan, G., Cygan, A., Voumard, T., **Wildi, T.**, Herr, T., Brasch, V., Lisak, D. & Masłowski, P. Dual-Comb Cavity-Mode Width and Shift Spectroscopy. *Measurement* **188**, 110519. ISSN: 02632241 (Jan. 2022).

*These authors contributed equally.

-
4. Lisak, D., Charczun, D., Nishiyama, A., Voumard, T., **Wildi, T.**, Kowzan, G., Brasch, V., Herr, T., Fleisher, A. J., Hodges, J. T., Ciuryło, R., Cygan, A. & Masłowski, P. Dual-Comb Cavity Ring-down Spectroscopy. *Scientific Reports* **12**, 2377. ISSN: 2045-2322 (Feb. 2022).
 5. Moroney, N., Del Bino, L., Zhang, S., Woodley, M. T. M., Hill, L., **Wildi, T.**, Wittwer, V. J., Südmeyer, T., Oppo, G.-L., Vanner, M. R., Brasch, V., Herr, T. & Del’Haye, P. A Kerr Polarization Controller. *Nature Communications* **13**, 398. ISSN: 2041-1723 (Jan. 2022).
 6. Voumard, T., Darvill, J., **Wildi, T.**, Ludwig, M., Mohr, C., Hartl, I., Herr, T. & Herr, T. 1-GHz Dual-Comb Spectrometer with High Mutual Coherence for Fast and Broadband Measurements. *Optics Letters* **47**, 1379–1382. ISSN: 1539-4794 (Mar. 2022).
 7. Voumard, T., Ludwig, M., **Wildi, T.**, Ayhan, F., Brasch, V., Villanueva, L. G. & Herr, T. Simulating Supercontinua from Mixed and Cascaded Nonlinearities. *APL Photonics* **8**, 036114. ISSN: 2378-0967 (Mar. 2023).
 8. Zhao, L. L., Dumusque, X., Ford, E. B., Llama, J., Mortier, A., Bedell, M., Moulla, K. A., Bender, C. F., Blake, C. H., Brewer, J. M., Cameron, A. C., Cosentino, R., Figueira, P., Fischer, D. A., Ghedina, A., Gonzalez, M., Halverson, S., Kanodia, S., Latham, D. W., Lin, A. S. J., Curto, G. L., Lodi, M., Logsdon, S. E., Lovis, C., Mahadevan, S., Monson, A., Ninan, J. P., Pepe, F., Roettenbacher, R. M., Roy, A., Santos, N. C., Schwab, C., Stefánsson, G., Szymkowiak, A. E., Terrien, R. C., Udry, S., Weiss, S. A., Wildi, F., **Wildi, T.** & Wright, J. T. The Extreme Stellar-signals Project. III. Combining Solar Data from HARPS, HARPS-N, EXPRES, and NEID. *The Astronomical Journal* **166**, 173 (Sept. 2023).
 9. Ulanov, A. E., **Wildi, T.**, Pavlov, N. G., Jost, J. D., Karpov, M. & Herr, T. Synthetic Reflection Self-Injection-Locked Microcombs. *Nature Photonics*, 1–6. ISSN: 1749-4893 (Jan. 2024).
 10. Fan, W., Ludwig, M., Rousseau, I., Arabadzhiev, I., Ruhnke, B., **Wildi, T.** & Herr, T. Supercontinua from Integrated Gallium Nitride Waveguides. *Optica* **11**, 1175–1181. ISSN: 2334-2536 (Aug. 20, 2024).
 11. Ulanov, A. E., **Wildi, T.**, Bhatnagar, U. & Herr, T. *Laser Diode Self-Injection Locking to an Integrated High-Q Fabry-Pérot Microresonator* Aug. 2024. arXiv: [2408.08679 \[physics\]](https://arxiv.org/abs/2408.08679).
 12. Ludwig, M., Ayhan, F., Schmidt, T. M., **Wildi, T.**, Voumard, T., Blum, R., Ye, Z., Lei, F., Wildi, F., Pepe, F., Gaafar, M. A., Obrzud, E., Grassani, D., Hefti, O., Karlen, S., Lecomte, S., Moreau, F., Chazelas, B., Sottile, R., Torres-Company, V., Brasch, V., Villanueva, L. G., Bouchy, F. & Herr, T. Ultraviolet Astronomical Spectrograph

- Calibration with Laser Frequency Combs from Nanophotonic Lithium Niobate Waveguides. *Nature Communications* **15**, 7614. ISSN: 2041-1723 (Sept. 2024).
13. Gaafar, M. A., Ludwig, M., Wang, K., **Wildi, T.**, Voumard, T., Sinobad, M., Lorenzen, J., Francis, H., Carreira, J., Zhang, S., Bi, T., Del’Haye, P., Geiselmann, M., Singh, N., Kärtner, F. X., Garcia-Blanco, S. M. & Herr, T. Femtosecond Pulse Amplification on a Chip. *Nature Communications* **15**, 8109. ISSN: 2041-1723 (Sept. 16, 2024).

List of presentations (as speaker)

- 1. Conference on Lasers and Electro-Optics (CLEO) — San Jose, CA, USA, 15-20 May 2022**
Thibault Wildi, Mahmoud Gaafar, Thibault Voumard, Markus Ludwig & Tobias Herr
Detectable Low-Noise Microwave-Repetition Rate in Chip-Integrated Fabry-Pérot Resonators
- 2. Center for Free-Electron Laser Science Symposium — Timmendorfer Strand, Germany, 5-7 October 2022**
Thibault Wildi, Thibault Voumard, Weichen Fan, Mahmoud Gaafar, Markus Ludwig, Alexander Ulanov, Bastian Ruhnke & Tobias Herr
Photonic Chip-based Ultrafast Sources
- 3. Conference on Lasers and Electro-Optics (CLEO) — San Jose, CA, USA, 7-12 May 2023**
Thibault Wildi, Alexander Ulanov, Thibault Voumard, Markus Ludwig & Tobias Herr
Soliton Microcomb Repetition-rate through a Second CW Laser
- 4. Conference on Lasers and Electro-Optics (CLEO) — San Jose, CA, USA, 7-12 May 2023**
Alexander Ulanov, Nikolay Pavlov, Thibault Wildi, John D. Jost, Maxim Karpov, M. & Tobias Herr
Self-Injection Locked Microcombs in Photonic Crystal Microresonators
- 5. Conference on Lasers and Electro-Optics Europe (CLEO EUROPE) — Munich, Germany, 26-30 June 2023**
Thibault Wildi, Alexander Ulanov, Thibault Voumard, Markus Ludwig & Tobias Herr
Soliton Microcomb Repetition-Rate Locking via CW Laser Injection

-
6. **European Optical Society Annual Meeting (EOSAM) — Dijon, France, 11-15 September 2023 (INVITED)**
Thibault Wildi, Alexander Ulanov, Thibault Voumard, Markus Ludwig & Tobias Herr
All-Optical Stabilization of Soliton Microcomb via CW Laser Injection
 7. **European Optical Society Annual Meeting (EOSAM) — Dijon, France, 11-15 September 2023 (STUDENT AWARD)**
Thibault Wildi, Mahmoud Gaafar, Thibault Voumard, Markus Ludwig & Tobias Herr
Kerr Solitons in High-Q Integrated Fabry-Pérot Microresonators
 8. **SPIE Photonics Europe — Strasbourg, France, 7-11 Avril 2024 (INVITED)**
Thibault Wildi, Alexander Ulanov, Bastian Ruhnke, Markus Ludwig, Weichen Fan & Tobias Herr
Frequency Combs in Photonic Crystal Microresonators
 9. **SPIE Photonics Europe — Strasbourg, France, 7-11 Avril 2024**
Mahmoud A. Gaafar, Markus Ludwig, Kai Wang, Thibault Wildi, Thibault Voumard, Milan Sinobad, Jan Lorenzen, Henry Francis, Shuangyou Zhang, Toby Bi, Pascal Del'hayé, Michael Geiselmann, Neetesh Singh, Franz Kärtner, Sonia García-Blanco & Tobias Herr
Chip Integrated Ultrafast Pulse Amplification
 10. **SPIE Photonics Europe — Strasbourg, France, 7-11 Avril 2024**
Thibault Wildi, Alexander Ulanov, Thibault Voumard, Markus Ludwig & Tobias Herr
Kerr Comb Sideband Injection Locking

Contents

Acknowledgements	v
Abstract (English/Deutsch)	vii
List of publications	xv
List of presentations	xix
1 Microresonator-based Kerr frequency combs	1
1.1 Optical frequency combs	2
1.2 Dielectric microresonators	3
1.2.1 Coupling	4
1.2.2 Properties of resonators	5
1.2.3 Resonance lineshape	6
1.2.4 Dispersion	7
1.2.5 Dispersion engineering	9
1.3 Microresonator frequency combs	10
1.3.1 Optical nonlinearity	10
1.3.2 Modeling Kerr-nonlinear resonators	11
1.3.3 Modulation instability	13
1.3.4 Dissipative Kerr solitons	15
1.4 Laser self-injection locking	18
1.5 Thesis organization	19
2 Dissipative Kerr-solitons in integrated Fabry-Perot microresonators	21
2.1 Introduction	23
2.2 Resonator design and fabrication	25
2.3 Experiments	27
2.4 Discussion	32

Contents

2.5	Supplementary information	32
2.5.1	Sample fabrication	32
2.5.2	Comparison between ring and Fabry-Perot resonators: Q-factor and line splitting.	33
2.5.3	Resonator dispersion and coupling	34
2.5.4	Soliton generation and soliton spectra	36
2.5.5	Numerical simulation	37
3	Sideband injection locking in microresonator frequency combs	39
3.1	Introduction	41
3.2	Results	43
3.3	Conclusion	50
3.4	Supplementary information	51
3.4.1	Locking range equation in terms of the injection ratio	51
3.4.2	Measuring the comb's repetition rate	51
3.4.3	Analytic description of sideband injection locking	52
3.4.4	Numeric simulation of the sideband injection locking range	57
3.4.5	Effect of thermal resonance shifts	58
4	Phase-stabilised self-injection-locked microcomb	61
4.1	Introduction	63
4.2	Setup	65
4.3	Experiments	68
4.4	Conclusion	71
4.5	Methods	72
4.5.1	Sample fabrication.	72
4.5.2	Frequency stability measurements.	72
4.5.3	Frequency response measurement.	73
4.6	Supplementary information	73
4.6.1	Tuning of the offset frequency f_{off}	73
4.6.2	Tuning of the repetition rate f_{rep}	74
4.6.3	Actuator linearity	75
4.6.4	Microheater frequency response	75
4.6.5	Comparison of fully phase-locked microcombs	76
5	Summary and Outlook	79
A	Frequency comb assisted diode laser spectroscopy	83
A.1	Working principles	84

A.1.1	Generation of comb markers	85
A.2	Setup	86
A.3	Signal processing	87
A.4	Validation and performance	90
A.4.1	MZI dispersion	90
A.4.2	Hydrogen cyanide	91
B	Derivation of coupled mode equations	93
B.1	Definitions	93
B.2	Derivation	94
B.2.1	Removal of spatial dependencies	94
B.3	Projection	96
B.4	Normalization	97
B.5	Decay and pump	98
	Bibliography	101

Chapter 1

Microresonator-based Kerr frequency combs

In recent years, microresonator-based optical frequency combs, arising from parametric frequency conversion within Kerr-nonlinear dielectric cavities, have emerged as compact yet efficient high repetition rate sources complementing ultrafast lasers based on active gain media. Commonly referred to as *microcombs*, these sources leverage the tight optical confinement and strong field enhancement provided by high finesse microresonators to achieve efficient frequency conversion from a pump laser to a set of evenly spaced comb lines. Exhibiting rich and complex behavior, these systems have become a hotbed for the study of optical nonlinear phenomena. One such state is *dissipative soliton* formation, where one or more self-sustained localized pulses circulate inside the cavity, giving rise to a low-noise, fully coherent optical frequency comb.

Through their compatibility with chip-scale integration, small footprint, and low power consumption, microresonator-based frequency combs promise to bring frequency comb technology to applications where the size, weight, or cost of macro-scale conventional sources is prohibitive — a prospect that might see microcombs parallel, for industrial and consumer-oriented applications, the transformative impact of mode-locked lasers on scientific research. While early research showcased the potential of microcombs in relatively elaborate laboratory experiments for applications in astronomy, low-noise microwave signal generation, or optical clocks, recent advancements have increasingly focused on improving the efficiency, flexibility, and operational simplicity of these systems. Notably, the adoption of *self-injection locking*, utilizing optical feedback from the resonator to control the emission wavelength of the driving laser, has enabled the miniaturization of microcomb sources by replacing cumbersome tabletop pump lasers

with chip-scale laser diodes.

Despite their promise, significant hurdles remain that hinder the widespread adoption of microresonator-based combs. Limitations in wavelength range, inconsistent and unreliable operation, and the complexity of actuation and stabilization schemes render these sources largely inaccessible to non-experts. This thesis addresses several of these key challenges by exploring dispersion and coherent phase control methods in microresonator frequency combs. This chapter provides the reader with the necessary context, starting from a brief overview of laser frequency combs in Section 1.1 and dielectric microresonator in Section 1.2. Subsequently, microresonator-based frequency combs are introduced in Section 1.3 with a focus on the *dissipative soliton* regime in Section 1.3.4. The chapter concludes by introducing self-injection locking and discussing its application to microcombs in Section 1.4.

1.1 Optical frequency combs

Optical frequency combs [1–5] (OFCs) generated from stable mode-locked lasers were first established in the 1990s through the pioneering work of Theodor W. Hänsch and John L. Hall in precision spectroscopy of the hydrogen atom [6–9] which was recognized with the Nobel Prize in Physics in 2005 [1, 2]. These sources rely on ultra-short optical pulses circulating inside the laser cavity. At every round trip, a copy of the pulse is outcoupled, creating a regular train of pulses spaced by the cavity round-trip time T_r . When the emitting laser is sufficiently stable, such that subsequent pulses are phase-coherent, the periodic nature of the waveform results in a spectrum of evenly spaced discrete optical frequencies separated by the laser's *repetition rate* $f_{\text{rep}} = T_r^{-1}$ (coining the term *frequency comb*). The mismatch between the phase and group velocities stemming from chromatic dispersion within the cavity induces a pulse-to-pulse phase slippage of the optical carrier relative to the pulse envelope [2]. This leads to a global shift of the comb spectrum by the slippage rate — an amount aptly called the *carrier-envelope offset frequency* f_{ceo} [2]. Therefore, the comb line frequencies obey

$$\nu_m = f_{\text{ceo}} + m f_{\text{rep}}, \quad m \in \mathbb{N}^+. \quad (1.1)$$

In this trivial expression lies the remarkable capability of optical frequency combs: establishing a coherent link between radio and optical frequencies [3–5, 10–14]. This ability to count individual optical cycles by dividing the optical spectrum with a "ruler" of evenly spaced lines of known optical frequency has enabled unprecedented measurement precision and ultimately enabled a range of new applications. From preci-

sion metrology [15, 16], spectroscopy [17–24] and optical clockworks [25–27] to microwave frequency synthesis [28] and astronomical spectrograph calibration [29–32], optical frequency combs have had a profound transdisciplinary impact.

While mode-locked lasers were established shortly after the first demonstration of the laser itself during the 1960s [33], it took nearly three decades for them to emerge as reliable sources of optical frequency combs. Early mode-locked lasers suffered from excessive noise and were unable to produce a phase-coherent train of pulses, resulting in the underlying comb structure being washed out [2]. Low-noise sources suitable for frequency metrology only arrived with the advent of femtosecond lasers, which allowed individual comb lines to be resolved. With a high peak power, the emitted pulses also enabled octave-spanning spectra via self-phase modulation inside photonic crystal fibers. This capability allowed for *self-referencing* [5, 9–13]: by comparing a frequency-doubled portion of the comb with the comb itself, it is possible to measure the comb’s carrier-offset frequency directly. With the capability to measure the comb’s two defining radio frequencies, f_{rep} and f_{ceo} , came the ability to fully-stabilized optical frequency combs [34, 35]. Through electronic feedback loops actuating on the laser’s operating parameters — such as the cavity length and pump current — both the repetition rate and offset frequencies could be locked to external references, providing a direct link from radio to optical frequencies.

1.2 Dielectric microresonators

An optical resonator is formed when light is spatially confined by reflective and/or refractive elements inside an optical *cavity*. This confinement results in the creation of a discrete set of *longitudinal modes* and allows for light to be stored and resonantly enhanced when the circulating field is matched to the cavity round-trip length. When, in addition, light is confined perpendicularly to its propagation direction (e.g., inside an optical fiber), the spatial distribution of the electromagnetic field is restricted to one or more *transverse modes* (also called *guided modes*). One can distinguish between *standing wave* configurations, where light oscillates between two or more reflective elements (the interfering forward- and backward-propagating components resulting in a standing wave), and *traveling wave* configurations, where light propagates unidirectionally along a closed loop. In its simplest form, a standing wave resonator can be made from two parallel reflective surfaces, in which case it is known as a *Fabry–Perot* interferometer or *etalon*. While resonators can be found throughout optics, from etalons for the stabilization of narrow linewidth lasers to the calibration of astronomical spec-

tographs, one of their uses is to enhance light-matter interaction. Optical *microresonators* [36], which confine light to a very small mode volume, are particularly well suited for this task.

In particular, *dielectric microresonators*, which confine light via total internal reflection inside a higher-index dielectric *core* surrounded by a lower-index *cladding* material, allow for efficient probing of the dielectric's nonlinear susceptibility. Broadly speaking, they can be grouped into two distinct categories: *whispering gallery mode* (WGM) resonators, where light is guided on a circular trajectory along the outer perimeter of the resonator at the interface with the surrounding medium, and *waveguide* resonators, where light is confined within a waveguide which is closed onto itself. While WGMs usually allow for a higher resonant enhancement and are somewhat simpler to fabricate, waveguide resonators typically achieve stronger confinement and can be fabricated through scalable wafer-based processes. Both WGM and waveguide resonators can be fabricated using a range of different materials (although for WGM resonators, the surrounding material is usually air), and microresonator frequency combs have been demonstrated in such platforms as silica [37–39], calcium fluoride [40, 41], magnesium fluoride [42–45], aluminum nitride [46, 47], diamond [48] and gallium phosphide [49]. Silicon nitride (Si_3N_4) [50–54], in particular, has emerged as a popular option. With a relatively high Kerr nonlinearity and low propagation losses, the platform allows for efficient parametric frequency conversion while being compatible with complementary metal-oxide semiconductor (CMOS) technology and, as a result, is now offered by several foundry services. Within this work, Si_3N_4 microresonators were used.

1.2.1 Coupling

While coupling to and from free-space cavities typically relies on semi-reflective surfaces, microresonators utilize evanescent fields to couple light from a *bus* waveguide directly into the guided mode of the resonator¹ [36, 55]. By placing the bus waveguide next to the cavity waveguide, such that their spatial modes overlap, optical power is transferred in and out of the resonator at a *coupling rate* κ_{ex} . Similarly, WGM resonators commonly employ prisms [56, 57] or tapered fibers [58] for this purpose. By adjusting the distance between the bus and resonator waveguide, the extent of the mode overlap can be tuned, and the coupling rate adjusted. As we will see in Section 1.2.3, matching the coupling rate to the resonator's intrinsic decay rate is key to maximizing the resonant enhancement.

¹As we show in Chapter 2, *semi-reflective* waveguide Bragg structures can also be used for standing-wave microresonators.

1.2.2 Properties of resonators

The *resonant condition* defines the resonant frequencies ω_m of a resonator as the specific frequencies where the cavity round-trip length is an integer multiple of the wavelength:

$$\frac{L}{\lambda_m} = m, \forall m \in \mathbb{N}^+. \quad (1.2)$$

Where L is the resonator round-trip length and $\lambda_m = 2\pi c / (n_{\text{eff}}\omega_m)$ the wavelength of the m th mode. The frequency interval between two successive resonances is called the *free spectral range* (FSR):

$$\text{FSR} = \frac{\omega_{m+1} - \omega_m}{2\pi}. \quad (1.3)$$

Resonators are characterized by their *decay rate* κ , which is the rate at which the stored energy W decays in the absence of an external power source, corresponding to the inverse lifetime τ of the cavity:

$$W(t) = W(0)e^{-t\kappa} = W(0)e^{-t/\tau}. \quad (1.4)$$

We distinguish between the intrinsic decay rate κ_0 , resulting from internal loss mechanisms such as absorption and scattering within the cavity, and the previously introduced extrinsic decay rate κ_{ex} , resulting from the coupling of the resonator, such that $\kappa = \kappa_0 + \kappa_{\text{ex}}$. The *coupling ratio* is defined as the ratio of the extrinsic to total decay rate:

$$\eta = \frac{\kappa_{\text{ex}}}{\kappa} = \frac{\kappa_{\text{ex}}}{\kappa_0 + \kappa_{\text{ex}}}. \quad (1.5)$$

The *quality factor* (Q-factor) is given by

$$Q = \frac{\omega}{\kappa}, \quad (1.6)$$

and is, for any oscillator, a measure of the total stored energy to the energy lost per radian of oscillation. The quality factor is related to *finesse* of the cavity

$$\mathcal{F} = 2\pi \frac{\text{FSR}}{\kappa} = 2\pi \frac{\text{FSR}Q}{\omega}, \quad (1.7)$$

which is directly linked to the maximum resonant enhancement achievable in a resonator (see the following Section).

1.2.3 Resonance lineshape

By requiring the intracavity field E_{cav} to be continuous, such that the contribution from pump field E_{in} perfectly offsets the phase and losses accumulated over one round trip, we can state

$$E_{\text{cav}} = \sigma e^{i\phi} E_{\text{cav}} + i\theta E_{\text{in}}, \quad (1.8)$$

where $\theta^2 = \kappa_{\text{ex}} T_r$ is the fractional round-trip pump coupling, $\sigma^2 = (1 - \kappa_0 T_r)(1 - \kappa_{\text{ex}} T_r)$ is the round-trip transmission and ϕ is the phase accumulated over one round trip. We find that the cavity power enhancement follows

$$\frac{P_{\text{cav}}}{P_{\text{in}}} = \frac{|E_{\text{cav}}|^2}{|E_{\text{in}}|^2} = \frac{\theta^2/2\sigma}{(1 + \sigma^2)/2\sigma - \cos(\phi)}, \quad (1.9)$$

which is periodically maximized when the round-trip phase ϕ is a multiple of 2π , corresponding to the resonant condition first presented in Eq. 1.2. The on-resonance power enhancement is proportional to the finesse \mathcal{F} and follows

$$\left. \frac{P_{\text{cav}}}{P_{\text{in}}} \right|_{\phi=0} = \frac{\theta^2}{(1 - \sigma)^2} \approx 2\eta \frac{\mathcal{F}}{\pi}, \quad (1.10)$$

where we have assumed both $\kappa_0 T_r \ll 1$ and $\kappa_{\text{ex}} T_r \ll 1$ ². Note that the power enhancement is maximized for a given intrinsic loss rate κ_0 when $\eta = 1/2$. This occurs when $\kappa_{\text{ex}} = \kappa_0$, in which case the resonator is said to be *critically coupled*. By extension, a resonator where $\kappa_{\text{ex}} < \kappa_0$ is said to be *under-coupled* while $\kappa_{\text{ex}} > \kappa_0$ is said to be *over-coupled*.

Lorentzian lineshape

In a high finesse resonator, the round-trip transmission is nearly unity, and the pump coupling is weak ($\sigma^2 \simeq 1$ and $\theta^2 \ll 1$). Consequently, as can be seen from Eq. 1.9, the power enhancement factor is approximately zero outside of the immediate vicinity of the resonance (specifically, outside of $1 - \cos(\phi) < \theta^2$). The resonator's spectrum can hence be regarded as a series of distinct discrete resonances. If we consider only a single resonance, we can introduce the first-order Taylor approximation $\cos(x) \approx 1 - x^2/2$, which results in the well-known *Lorentzian* lineshape

$$\frac{P_{\text{cav}}}{P_{\text{in}}} = \frac{\theta^2/\sigma}{(1 - \sigma)^2/\sigma + \phi^2}, \quad (1.11)$$

²This assumption of low round-trip loss is valid for high finesse resonators.

with a full-width at a maximum (FWHM) of

$$2 \frac{1 - \sigma}{\sqrt{\sigma}} \approx \frac{2\pi}{\mathcal{F}}. \quad (1.12)$$

To a first-order approximation, the round-trip phase can be expressed as $\phi \approx \omega T_r$, meaning the optical linewidth is κ . Therefore, key resonator parameters can be extracted by recording the optical lineshape of its resonances, such as the total decay rate κ (from Lorentzian FWHM), the FSR (from the mode separation) and the finesse \mathcal{F} [59]. When considering additional interactions within the resonators and bus, more complex lineshapes can arise. For example, coupling-induced hybridization between counterpropagating modes in a traveling wave resonator or higher order transverse modes can lead to so-called *split-resonances* [60], while asymmetric *Fano* resonances can arise from reflective elements inside the bus waveguide [61] (such as the chip facet).

1.2.4 Dispersion

Somewhat confusingly, the term *dispersion* is often used quite liberally to designate slightly different facets of the same concept. In its broadest sense, dispersion designates the relation between the angular frequency ω and the propagation constant β :

$$\beta(\omega) = \frac{\omega}{c} n_{\text{eff}}(\omega) = \frac{2\pi}{\lambda_0} n_{\text{eff}}(\omega). \quad (1.13)$$

Often, *dispersion* will be used to refer specifically to the nonlinearity of $\beta(\omega)$, i.e., the frequency-dependence of the effective phase index $n_{\text{eff}}(\omega)$. In photonics, a Taylor expansion around a central frequency ω_0 is commonly used:

$$\beta(\omega) = \beta_0 + (\omega - \omega_0) \frac{\beta_1}{1!} + (\omega - \omega_0)^2 \frac{\beta_2}{2!} + \dots, \quad (1.14)$$

$$\text{where } \beta_n = \left. \frac{\partial^n \beta(\omega)}{\partial \omega^n} \right|_{\omega=\omega_0} \quad (1.15)$$

are the dispersion coefficient corresponding to *first* ($n = 1$), *second* ($n = 2$) and *higher-order* dispersion ($n \geq 2$). Specifically, $\beta_0 = \omega_0 / v_p$ is related to the *phase velocity* v_p at frequency ω_0 , $\beta_1 = v_g^{-1}$ is the inverse *group velocity* and β_2 is the *group velocity dispersion* (GVD). Depending on the sign of the β_2 , one distinguishes between *normal* GVD ($\beta_2 > 0$), where the group velocity decreases with optical frequency, and *anomalous* GVD ($\beta_2 < 0$) where the group velocity increases with optical frequency.

Dispersion in microresonators

In microresonators, dispersion affects the resonant frequencies ω_m via the resonant condition

$$L\beta(\omega_m) = 2\pi m, \forall m \in \mathbb{N}^+, \quad (1.16)$$

where L is the resonator's round-trip length and m is the *longitudinal mode number*. Similar to Eq. 1.14, the resonant frequencies can be described by an expansion around a central mode m_0 with frequency ω_0

$$\omega_\mu = \omega_0 + \mu \frac{D_1}{1!} + \mu^2 \frac{D_2}{2!} + \dots, \quad (1.17)$$

$$\text{where } D_n = \left. \frac{\partial^n \omega_\mu}{\partial \mu^n} \right|_{\mu=0}. \quad (1.18)$$

Here we have introduced the *relative mode number* $\mu = m - m_0$. The dispersion coefficients D_n and β_n are related through series reversion

$$D_1 = \frac{2\pi}{\beta_1 L}, \quad (1.19)$$

$$D_2 = -v_g D_1^2 \beta_2, \quad (1.20)$$

$$D_3 = 3 \frac{D_2^2}{D_1} - D_1^3 v_g \beta_3, \quad (1.21)$$

...

Here, $D_2 > 0$ corresponds to *anomalous* dispersion, and $D_2 < 0$, to *normal* dispersion.

Integrated dispersion

A common way of describing the dispersion of a dielectric microresonator is through the *integrated dispersion* [44], which is obtained by subtracting the constant and linear terms from Eq. 1.17:

$$D_{\text{int}}(\mu) = \omega - \omega_0 - \mu D_1 = \sum_{n \geq 2} \mu^n \frac{D_n}{n!}. \quad (1.22)$$

This representation describes the deviation of the resonance frequencies ω_μ from an equidistant (i.e., dispersionless) frequency grid $\omega_0 - \mu D_1$, isolating the effects of higher-order dispersion ($n \geq 2$).

1.2.5 Dispersion engineering

In nonlinear optical microresonators, and more generally for any nonlinear optical process, the photon flux between respective frequency components depends on their relative phase. Consequently, precisely managing the microresonator's dispersion is crucial for effectively controlling these nonlinear interactions. As we will discuss in Section 1.3, second-order dispersion, in particular, plays a key role in microcombs, impacting, for instance, the comb type, bandwidth, and formation dynamics.

Dispersion engineering aims to tailor the dispersion of dielectric microresonators, with a particular emphasis on the sign and strength of D_2 . Key parameters include the core and cladding materials and the resonator geometry [62]. While most materials exhibit normal GVD in the visible and near-infrared spectral regions due to electronic transitions in the ultraviolet range, the total microresonator dispersion can still be adjusted through *geometric dispersion*. As the wavelength λ increases, guided modes transition from a regime of strong confinement, where most of the electromagnetic field is contained within the waveguide core, to a regime of weak confinement, where the mode expands into the surrounding cladding. During this transition, the modes' effective index $n_{\text{eff}}(\lambda)$ shifts from that of the core to that of the cladding. By tailoring the waveguide cross-section, this transition can be adjusted such that anomalous GVD ($\partial^2 n_{\text{eff}}/\partial\lambda^2 < 0$) is obtained on the blue side of the transition, even if both the core and cladding materials exhibit normal dispersion [63]. In the case of dielectric microresonators fabricated through planar processes, this typically involves carefully controlling the width and height of a rectangular cross-section waveguide [64]. For silica-clad silicon nitride microresonators, such as those used in this thesis, anomalous group velocity dispersion is only accessible with a "thick" silicon nitride layer (>700 nm) [65–67]. Whispering gallery mode resonators, often shaped through manual polishing and/or laser ablation, can use constant radii or wedge-shaped profiles to achieve desirable dispersion characteristics [68]. In ring-type resonators, the bending of the waveguide also influences dispersion [69]. Although generally weak, this effect becomes significant for smaller radii ($< 25\mu\text{m}$) [70].

Recently, more advanced dispersion engineering techniques have emerged, typically relying on the hybridization of frequency-degenerate modes. The frequency shifts associated with the coupling between cross-polarized modes [71], fundamental and higher order spatial modes [72], counterpropagating modes [73, 74], or modes in distinct resonators [75–79] can enhance, flatten, or even reverse the sign of the dispersion over specific wavelength ranges. In addition, as we will see in Chapter 2, sub-

wavelength structures [80, 81] are particularly promising as they allow for broadband dispersion engineering.

1.3 Microresonator frequency combs

1.3.1 Optical nonlinearity

A medium is said to be optically nonlinear when its polarization responds nonlinearly to an incoming electromagnetic wave. Specifically, when a material's electrical susceptibility is itself a function of the electric field strength, it leads to a nonlinear relationship between the incident electric field $\tilde{E}(t)$ and the dielectric polarization of the medium $\tilde{P}(t)$ which can be described by a power series [82]

$$\tilde{P}(t) = \epsilon_0 \chi \tilde{E}(t) = \epsilon_0 (\chi^{(1)} \tilde{E}(t) + \chi^{(2)} \tilde{E}^2(t) + \chi^{(3)} \tilde{E}^3(t) + \dots), \quad (1.23)$$

where ϵ_0 denotes the vacuum permittivity and $\chi^{(n)}$ the material's n^{th} order electric susceptibility³. While higher-order ($n \geq 2$) contributions to the polarization are insignificant for the vast majority of applications, this is not the case when strong optical fields are present, such as in ultrafast lasers or high-Q microresonators. In such cases, the *nonlinear polarization*

$$\tilde{P}^{\text{NL}}(t) = \sum_{n \geq 2} \chi^{(n)} \tilde{E}^n(t) \quad (1.24)$$

can no longer be neglected and acts as a source term in the *nonlinear wave equation*

$$\nabla^2 \tilde{E} - \frac{n_0^2}{c^2} \frac{\partial^2 \tilde{E}}{\partial t^2} = \frac{1}{\epsilon_0 c^2} \frac{\partial^2 \tilde{P}^{\text{NL}}}{\partial t^2}, \quad (1.25)$$

which describes the propagation of light inside a nonlinear medium⁴. Such *parametric gain* can lead to the conversion of light between different frequencies and to the excitation of electromagnetic waves with new frequencies.

Kerr nonlinearity

In centrosymmetric media, $\chi^{(2)}$ vanishes [82], and the main contribution to the nonlinear polarization stems from $\chi^{(3)}$ -nonlinearity, also known as *Kerr nonlinearity*⁵. Let us

³In this expression, we have neglected the vector nature of both the electric and polarization fields.

⁴The nonlinear wave equation can be derived from the Maxwell equations accounting for the nonlinearity of the electric susceptibility.

⁵*Kerr nonlinearity* refers specifically to the real part of $\chi^{(3)}$, which is responsible for the *Kerr effect* — a change of refractive index in response to an applied electric field. Other effects such as nonlinear

explore *parametric frequency conversion* in such a medium by considering an incident electric field

$$\tilde{E}(t) = \sum_{n=1}^N E_n e^{-j\omega_n t} + c.c. \quad (1.26)$$

comprised of N different pure tones with frequency ω_n . In a Kerr-nonlinear medium, the nonlinear polarization is proportional to $\tilde{E}^3(t)$ and therefore, the product between the respective tones will contain terms at new frequencies

$$3\omega_n, \quad (1.27)$$

$$\omega_n + \omega_m + \omega_l, \quad (1.28)$$

$$\text{and } \omega_n + \omega_m - \omega_l, \quad (1.29)$$

where $n, m, l \in \{1, \dots, N\}$. These processes are known as *third harmonic generation*, *triple-sum generation*, and *four wave mixing*, respectively, and can lead to the excitation of electromagnetic waves at new frequencies. If these newly formed components build up to sufficient strength, they can themselves contribute to the mixing process — a phenomenon known as *cascaded four-wave mixing*.

1.3.2 Modeling Kerr-nonlinear resonators

The dynamics of Kerr-nonlinear resonators are commonly described using two different approaches: the *Lugiato-Lefever equation* (LLE) and its frequency domain counterpart, the *coupled-mode equations* (CME). These models are mathematically equivalent and can be transformed into each other using the Fourier transform [83, 84]. Both approaches are mean-field models that rely on the assumption that the system's evolution is slow relative to the cavity round-trip time. As a result, localized phenomena, such as point coupling or localized dispersion features, like those induced by gratings in a Fabry-Perot cavity, are average over the microresonator round trip. To capture these effects, methods like the *Ikeda map* [85] are available; however, they require simulating the field's evolution for every round trip when solved numerically, which is computationally expensive.

In the following Section, we introduce the LLE and CME in their dimensionless forms. This allows the system to be fully defined by the normalized pump power and detuning while parameters such as the resonator linewidth, dispersion, and nonlinearity are

absorption or *stimulated Raman scattering* stem from the complex part and frequency dependence of $\chi^{(3)}$, respectively.

incorporated into the dimensionless quantities and coordinates [86, 87]:

$$\begin{aligned}\tau &= \frac{\kappa}{2}t, & \theta &= \sqrt{\frac{\kappa}{2D_2}}\phi, \\ \zeta_0 &= \frac{2(\omega_0 - \omega_p)}{\kappa}, & f &= \sqrt{\frac{8\eta g_0}{\kappa^2}}s_{\text{in}}, \\ \psi &= \sqrt{\frac{2g_0}{\kappa}}A, & a_\mu &= \sqrt{\frac{2g_0}{\kappa}}A_\mu.\end{aligned}\tag{1.30}$$

Here, τ and θ are the normalized time and spatial coordinates, respectively, while ζ_0 is the normalized pump-to-resonance detuning. The normalized pump amplitude f is obtained by scaling the pump's photon flux $|s_{\text{in}}|^2$ by the effective nonlinear coefficient $g_0 = \hbar\omega_p^2 cn_2 / (n_0^2 V_{\text{eff}})$. The slow-varying complex field envelope $\psi(\theta, \tau)$ and the slow-varying complex mode amplitudes $a_\mu(\tau)$ are similarly normalized.

Lugiato-Lefever equation

The Lugiato-Lefever equation [88–90] is a detuned, driven, and damped (dissipative) version of the one-dimensional nonlinear Schrödinger equation [91, 92]:

$$\frac{\partial\psi}{\partial\tau} = -(1 + i\zeta_0)\psi + \frac{i}{2}\frac{\partial^2\psi}{\partial\theta^2} + i|\psi|^2\psi + f.\tag{1.31}$$

It describes how the slow-varying complex field envelope $\psi(\theta, \tau)$ evolves over time. The first term denotes the combined effects of cavity loss and pump detuning, while the second term accounts for the effects of group velocity dispersion through the second-order derivative of the field with respect to θ . The LLE can easily be generalized to higher-order dispersion by including higher-order derivatives. The third term describes Kerr-induced self-phase modulation, while the homogeneous pump field f acts as a source term. Spatially structured pump fields can also be used to describe pulse pumping or other types of multi-frequency excitation [93, 94].

Coupled-mode equations

The coupled-mode equations describe the evolution of the individual mode amplitudes as a system of coupled oscillators interacting through four-wave mixing [53, 95–97]. A derivation of the CME, beginning from the nonlinear wave equation, can be found in Appendix B. The dimensionless form of the CME is written as follows [44]:

$$\frac{\partial a_\mu}{\partial\tau} = -(1 + i\zeta_\mu)a_\mu + i \sum_{\mu', \mu''} a_{\mu'} a_{\mu''} a_{\mu'+\mu''-\mu}^* + \delta_\mu f.\tag{1.32}$$

Here, $a_\mu(\tau)$ denotes the slow-varying complex amplitude of the mode with index μ . The term $(1 + i\zeta_\mu)$ accounts for the loss and detuning associated with this mode, where $\zeta_\mu = 2(\omega_\mu - \omega_p - \mu D_1)/\kappa$ is the normalized detuning combining the effect of pump detuning and dispersion. It contains the integrated dispersion introduced in Eq. 1.22 and, therefore, can describe an arbitrary dispersion profile. The summation describes the nonlinear coupling between different modes via FWM by considering all possible frequency combinations. The Kronecker delta function δ_μ ensures the pump only drives the intended mode $\mu = 0$.

Standing-wave resonators

While both Eq. 1.31 and Eq. 1.32 apply to traveling-wave cavities, they can be generalized to Fabry-Perot type resonators by accounting for the cross-phase modulation between counterpropagating waves [93, 98]. This term is homogeneous and only depends on the average intracavity power, and thereby can be interpreted as an additional power-dependent detuning. Consequently, both traveling- and standing-wave resonators exhibit equivalent dynamics.

1.3.3 Modulation instability

Kerr-nonlinearity, specifically four-wave-mixing (FWM), governs the formation of optical frequency combs inside high-Q microresonators. When a continuous wave (CW) pump laser is tuned into a resonance of a Kerr-nonlinear resonator, the intracavity power can build up to exceed the threshold at which parametric gain overcomes the cavity round-trip loss. This initiates a process known as *modulation instability* [99] (MI), as small perturbations in the homogeneous intracavity field will grow for some spectral components, breaking spatial symmetry [100].

Specifically, through *degenerate* four-wave mixing — where the pump wave contributes twice in the mixing process ($\omega_n = \omega_m$ in Eq. 1.29) — small inhomogeneities in the field are amplified, resulting in the formation of a first pair of sidebands symmetrically spaced around the pump frequency [100]. At the threshold pump power, these sidebands emerge within the resonator modes $\pm\mu_{\text{th}}$, where

$$\mu_{\text{th}} = \sqrt{\frac{\kappa}{D_2}}, \quad (1.33)$$

is given by the resonator decay rate κ and second order dispersion D_2 ⁶ [53]. As soon as

⁶This result can be derived from the coupled mode equations by considering a three mode system [53,

they emerge, the *primary sidebands* act as seeds for further *non-degenerate* four-wave mixing, creating new frequency components in a cascading sequence [95]. As this cascade progresses, a broad set of evenly spaced frequency lines is formed, constituting the so-called *primary comb*. Energy conservation dictates that these comb lines are equidistant, matching the resonator's free spectral range or an integer multiple thereof. The presence of dispersion leads to a mismatch, or "walk-off," between the comb line frequencies and microresonator resonance frequencies, reducing the efficiency of the FWM process and limiting the overall extent of the comb. In practice, the presence of anomalous dispersion is a prerequisite for the initiation of the primary sidebands, as it compensates for the differential nonlinear resonance shift between the pump mode and other modes [100]. Consequently, the generation of combs from Kerr-nonlinearity (i.e., *Kerr frequency combs*) requires a resonator with anomalous dispersion, at least locally, around the pump frequency.

Chaotic states

When dispersion is strong relative to the linewidth such that $\mu_{\text{th}} = 1$ (as can occur in high FSR microresonators), the primary sidebands form within the resonances neighboring the pump mode, resulting in a *natively mode-spaced comb* [53, 102]. Conversely, if $\mu_{\text{th}} \geq 2$, the primary comb will have a spacing of two or more FSRs [103, 104]. In this case, further increasing the intracavity power — either by raising the power of the pump laser or by tuning the pump laser closer to resonance — causes the primary comb lines to initiate *sub-combs* (or *secondary combs*) as parametric gain exceeds losses in the previously unpopulated modes [53, 105].

These sub-combs are, in general, not commensurate with the primary comb, thereby introducing new frequency components to the system [37, 53, 106–108]. Consequently, through cascaded four-wave mixing, multiple lines can build up within each resonator mode, eventually populating each resonance with a continuum of optical frequencies, corresponding to a chaotic and unstable waveform often referred to as the *chaotic modulation instability* regime. These incoherent states yield a noisy radio-frequency signal and are not desirable for most Kerr frequency comb applications, which rely on pure and well-defined comb line frequencies.

87, 97, 101].

1.3.4 Dissipative Kerr solitons

The Lugiato-Lefever equation (or, equivalently, the coupled mode equations) supports a rich landscape of dynamic and stationary states that go far beyond the modulation instability regime. Particularly relevant to this thesis are *Dissipative Kerr Solitons* (DKS), a stationary state in the form of optical pulses that maintain their shape and energy indefinitely as they circulate within the cavity. Also called *cavity solitons* or *microresonator solitons*, they are distinct from conservative solitons, such as those found in optical fiber, which arise purely from a balance between nonlinearity and dispersion [90, 109, 110]. DKS, in addition, rely on the equilibrium between the cavity loss and the energy provided by the pump laser. As such, DKS form stable low-noise attractor states with well-defined optical frequency comb spectra.

While multiple soliton pulses can coexist within a cavity, the single DKS state is particularly interesting due to its optical power spectrum characterized by a smooth hyperbolic secant envelope.

Theoretical description

While an exact analytical solution is only available for conservative solitons, DKS can still be described approximately as the superposition of a continuous wave background and a hyperbolic secant pulse [44]:

$$\psi \simeq \psi_0 + B e^{i\varphi_0} \operatorname{sech}(B\theta) \quad (1.34)$$

In this expression, the term ψ_0 denotes the homogeneous solution of the lower stable branch of the bistability region [87, 92]:

$$\psi_0 \simeq \frac{f}{\zeta_0^2} - i \frac{f}{\zeta_0}, \quad (1.35)$$

The second term in Eq. 1.34 corresponds to the conservative soliton solution. The parameters are determined by substituting the soliton ansatz into the LLE, which yields:

$$B \simeq \sqrt{2\zeta_0}, \quad (1.36)$$

$$\cos(\varphi_0) \simeq \frac{8\zeta_0}{\pi f}. \quad (1.37)$$

The detuning interval $\zeta_0 \in [\zeta_0^{\min}, \zeta_0^{\max}]$ over which a soliton can be sustained is known as the *soliton existence range*. The lower limit ζ_0^{\min} directly derives from the bistability

criterion $f^2 < \frac{2}{27}\zeta_0(\zeta_0 + 9)$ [87, 92], while the upper limit stems from Eq. 1.37, requiring $\zeta_0 < \frac{\pi f}{8}$ [44]. Note that the soliton's amplitude and temporal width depend not on the pump power but the detuning. However, a stronger pump does extend the soliton range, hence providing access to larger detunings.

Transformed back into physical units, the soliton temporal profile can be written as [44]

$$\psi(t) = \sqrt{2\zeta_0} \operatorname{sech}(t/\Delta t), \quad (1.38)$$

$$\text{where } \Delta t = \frac{1}{D_1} \sqrt{\frac{D_2}{\zeta_0 \kappa}}, \quad (1.39)$$

while its optical spectrum is similarly given by

$$\tilde{\psi}(\omega) = \sqrt{D_2/2\kappa} \operatorname{sech}((\omega - \omega_p)/\Delta\omega), \quad (1.40)$$

$$\text{where } \Delta\omega = \frac{2D_1}{\pi} \sqrt{\frac{\zeta_0 \kappa}{D_2}}. \quad (1.41)$$

Thus, the soliton's spectral width directly scales with the inverse square root of the dispersion parameter D_2 as the walk-off between the equidistant lines of the soliton's spectrum and the resonances of the microresonator is reduced.

More generally, we see that for a given microresonator and pump detuning, the soliton's spectral width scales with $\sqrt{\kappa/D_2}$, and its temporal width, with the inverse thereof. This is the same expression as Eq. 1.33 defining the spacing of the primary comb in the MI regime and also approximately corresponds to the maximum number of soliton pulses that can be concurrently sustained within the resonator [44, 111].

DKS generation

While a specific set of operating parameters may support DKS, they cannot spontaneously arise due to the system's bistability⁷. To initiate them, they must first be seeded. This can be achieved either through an externally injected pulse waveform (i.e., *kick-starting*) — a technique commonly employed in optical fiber cavities [86, 112, 113] — or through a precursor state that contains pulses with sufficient energy to converge into the soliton attractor state [44, 54]. In the case of optical microresonators, the latter approach is usually employed, as explained below.

When tuning a continuous wave pump laser from the blue-detuned side of the resonance into the red-detuned soliton existence range, the system first passes through the

⁷The continuous wave background is, by itself, a stable solution.

modulation instability regime. In this regime, an unstable and chaotic waveform forms within the cavity as secondary sidebands emerge. This stochastic waveform contains transient pulses that can seed DKS when the pump detuning enters the DKS existence range. Transient pulses with sufficient energy converge into stationary soliton pulses, while most decay into the continuous wave background, resulting in a sharp drop in total intracavity power. The number of soliton pulses that ultimately form within the cavity depends on the number of transient pulses with sufficient energy at the system's transition. Given the chaotic nature of the preceding MI regime, this process is non-deterministic, often yielding a variable number of solitons — and sometimes none — when repeated.

As the pump detuning further increases, reaching the red boundary of the DKS existence range, the solitons decay. In practice, due to noise and slight variations in local conditions, the solitons do not all decay simultaneously. This results in a characteristic "staircase" pattern in the intracavity power as the number of solitons incrementally decreases. The initial sharp drop in power followed by *soliton steps* is a key signature of soliton formation that can be monitored during experiments [44, 114].

In practice, these abrupt changes in intracavity power pose significant experimental challenges. Most microresonator platforms exhibit a positive thermo-optic coefficient ($dn/dT > 0$), meaning that a given cavity's optical path increases with temperature. This leads to a redshift of the resonator's effective resonance frequencies, directly proportional to the cavity temperature and, therefore, intracavity power. Upon soliton formation, the sharp power drop leads to a rapid blueshift in the effective resonance frequency⁸, thereby increasing the pump detuning, often exceeding the soliton existence range. Several techniques have been developed to address this issue, including rapid tuning of the pump laser [54, 115–117] or microresonator [118–120], the use of auxiliary lasers [98, 121], as well as slow [122] and fast [93, 94] pump modulation. Despite these strategies, managing the thermal and detuning dynamics remains a significant challenge. As we will see in the next Section, laser self-injection locking offers a simple yet elegant solution by replacing the continuous-wave pump laser with a diode laser susceptible to optical feedback from the microresonator, eliminating the need for precise and rapid pump laser actuation.

⁸The thermal time constants for chip-integrated microresonators can be extremely short, of the order of a few μs .

1.4 Laser self-injection locking

Until now, we have considered microresonator nonlinear dynamics under the assumption of an independent, externally actuated continuous wave pump laser. A compelling alternative is offered by laser *self-injection locking* (SIL), a technique that leverages frequency-selective optical feedback from the microresonator to stabilize the laser emission frequency [123–126]. By coupling the driving laser to a high-Q microresonator without any form of optical isolation, Rayleigh scattering inside the microresonator caused by volumetric inhomogeneities and surface roughness reflects resonant light back into the pump laser cavity [127]. This coherent feedback causes the laser’s emission frequency to lock onto the resonance frequency of the microresonator. When operating inside this SIL regime, filtering by the high-Q resonator suppresses fluctuation in the laser emission frequency compared to free-running operation. This suppression is proportional to the square of the microresonator’s quality factor⁹ and results in a substantial reduction in the laser’s linewidth, which can reach several orders of magnitude — enabling, for example, sub-kHz linewidths from chip-scale semiconductor diode lasers [128].

In the context of microresonator frequency combs, laser self-injection locking possesses several advantages over conventional pumping schemes [45, 119, 129–133]. First, SIL permits replacing complex narrow-linewidth tabletop lasers with semiconductor diode lasers, providing a truly chip-scale optical frequency comb source. Secondly, in the SIL regime, the laser’s emission frequency is locked to the microresonator through fast optical feedback, automatically tracking fluctuation in the microresonator resonance frequency. This eliminates the need for a rapidly tunable laser and addresses many of the challenges associated with thermal instabilities, further reducing operational complexity.

One of the challenges associated with using SIL for DKS generation is the limited overlap between the *SIL range* — the span of pump-to-resonance detunings over which the laser remains self-injection locked to the microresonator — and the soliton existence range. Indeed, due to the random nature of defects and imperfections inside the cavity, optical feedback is typically unpredictable and weak, thus constraining the SIL range. We recently demonstrated that this limitation can be effectively addressed through the use of synthetic reflection [134], achieved by inscribing a photonic crystal structure into the microresonator waveguide [74, 80, 81, 135, 136]. This approach provides both strong (adjustable) and predictable levels of optical feedback, making it par-

⁹Thermorefractive noise inside the cavity can ultimately become a limiting factor.

ticularly well-suited to DKS generation. The coupling between frequency-degenerate counterpropagating modes at the pump frequency also results in hybridized modes with significant frequency shifts. These shifts are akin to strong anomalous dispersion, promoting the formation of single- over multi-DKS states without compromising the soliton's spectral width [74].

In Chapter 4, we demonstrate that such synthetic reflection SIL microcombs can be fully phase-locked to external microwave frequency references, thus achieving chip-scale, metrological-grade optical frequency combs [137].

1.5 Thesis organization

The remainder of this thesis is structured as follows:

Chapter 2 demonstrates, for the first time, dissipative Kerr soliton generation inside an integrated Fabry-Perot microresonator. Crucially, dispersion management of the cavity is dominated by the contribution of the photonic crystal reflectors forming the mirrors of the linear cavity. This work showcases the power of sub-wavelength nanostructuring for dispersion management in nonlinear integrated photonics and promises exciting new opportunities for bringing Kerr frequency combs to previously unattainable wavelength ranges and material platforms.

Chapter 3 explores *soliton sideband injection-locking*, a technique by which an external optical frequency is injected into the sidebands of a soliton comb, enabling full control of the comb's repetition rate and offset frequencies. This scheme enables new approaches to low-noise microwave generation, compact optical clocks with simplified locking schemes, and, more generally, stabilized low-noise frequency comb sources from Kerr-nonlinear resonators.

Chapter 4 presents a chip-scale, electrically-driven, metrology-grade SIL microcomb operating at CMOS-compatible voltages. Based on laser self-injection locking, the source combines a semiconductor laser diode and a high-quality factor silicon nitride microresonator equipped with an integrated microheater to achieve a small-footprint, low-complexity, low-cost, and CMOS-compatible frequency comb, which can be fully phase stabilized.

This thesis is a cumulative work combining the results of three different peer-reviewed publications. In the respective chapters, small changes have been made with respect to the published material to enhance clarity and uniformity, including adjustments to figures to better fit the format of this thesis.

Chapter 2

Dissipative Kerr-solitons in integrated Fabry-Perot microresonators

Thibault Wildi¹, Mahmoud A. Gaafar¹, Thibault Voumard¹, Markus Ludwig¹ and Tobias Herr^{1,2}

¹ *Deutsches Elektronen-Synchrotron DESY, Notkestr. 85, 22607 Hamburg, Germany*

² *Physics Department, Universität Hamburg UHH, Luruper Chaussee 149, 22761 Hamburg, Germany*

Published in *Optica* Vol. 10, Issue 6, pp. 650-656 on May 23, 2023

<https://doi.org/10.1364/OPTICA.480789>

Author contributions

T.W. and T.H. conceived the experiment. T.W. designed the setup and the photonic chip, performed the experiments, analyzed the data, and performed numerical simulations. M.G. supported the experiments. T.V. and M.L. assisted in data analysis. T.H. supervised the work. T.W. and T.H. prepared the manuscript with input from all authors.

Abstract

Dissipative Kerr solitons (DKSs) in integrated microresonators have enabled breakthroughs in sensing, communication, and signal processing. So far, integrated DKS sources have exclusively relied on ring-type resonators where the resonator's dispersion is defined by its waveguide. New means of dispersion engineering, beyond modifying the waveguide's cross-section, are critically needed for accessing new wavelength and operating regimes. Here, we demonstrate for the first time DKS generation in an integrated Fabry-Perot microresonator. In this topology, the dispersion is not dominated by the waveguide but by nano-structured photonic crystal mirrors. Leveraging wafer-level fabrication, high intrinsic Q-factors of 4 million are achieved in the absence of unintentional avoided-mode crossings, which can otherwise prevent DKS formation. This establishes a new integrated resonator topology for DKS generation and creates opportunities for new wavelength domains and novel approaches such as dispersion managed solitons or Nyquist-solitons.

2.1 Introduction

Dissipative Kerr solitons (DKSs) [110, 112, 138, 139] in laser-driven dielectric microresonators provide access to metrology-grade femtosecond sources and broadband frequency combs with repetition rates from tens of GHz to multiple THz. They are self-enforcing solutions to the Lugiato-Lefever equation (LLE) and can emerge in *high-quality factor* (Q) microresonators from the balance between *anomalous* group delay dispersion (GDD), loss and Kerr-nonlinearity under (typically) continuous-wave (CW) laser driving. Intriguing nonlinear dynamics including soliton crystals [140], soliton molecules [141], synchronization between resonators [142], and discrete photonic time crystals [143] have been observed. Owing to their potential for compact photonic integration [50, 139], DKS sources are a transformative technology, impacting a wide range of cross-disciplinary applications, including data transmission [144] and processing [145], ranging [146, 147], microwave photonics [148], dual-comb spectroscopy [149], and astronomical spectrograph calibration [150, 151]. To this day, integrated DKS sources have exclusively been pursued in traveling-wave ring-type resonators. Here criteria for DKS formation can be routinely met, including high Q-factor, anomalous dispersion (negative GDD), as well as a resonance spectrum free of unintentional avoided mode crossings (AMXs) [44]. Furthermore, the dispersion can be tuned (to some extent) by adjusting the width and height of the resonator waveguide, with significant impact on the DKS and their spectra. Future extension of DKS technology, including extension to new wavelength regimes (e.g. visible wavelengths), spectral

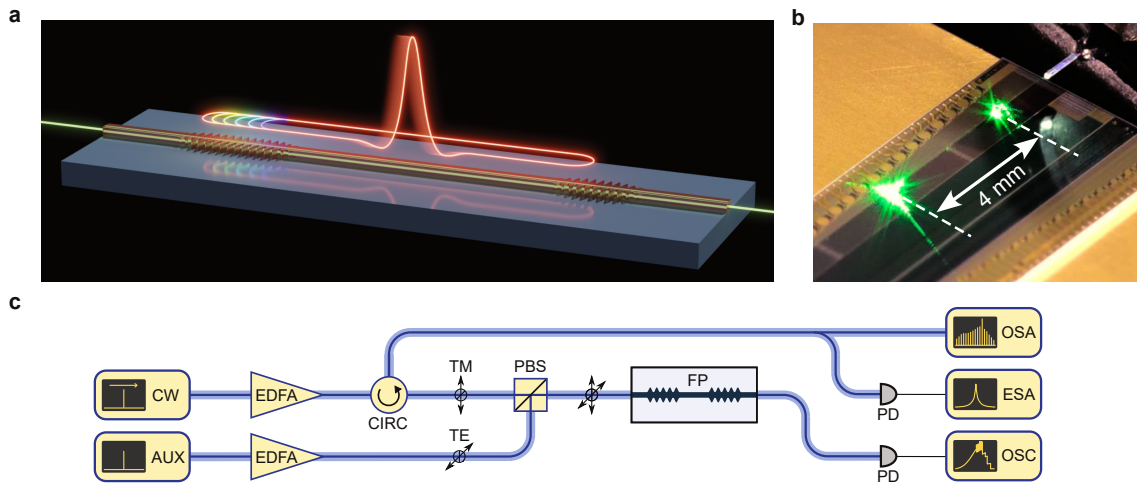


Figure 2.1 | Soliton generation in chip-integrated photonic crystal Fabry-Perot cavities. **a**, Illustration of a dissipative Kerr soliton (DKS) under continuous-wave pumping inside a chip-integrated photonic crystal Fabry-Perot (FP) microresonator with reflector-induced anomalous dispersion. **b**, Photograph of a CW-driven FP microresonator. Scattered coincidental third-harmonic generation indicates the position of the PCRs. **c**, Setup for exciting DKSs inside the FP microresonator. A transverse magnetic (TM) polarized continuous-wave (CW) pump laser is tuned into resonance while the resonator is thermally stabilized by an auxiliary continuous-wave laser (AUX) in the transverse electric (TE) mode. EDFA: erbium-doped fiber amplifier; CIRC: circulator; PBS: polarizing beam splitter; PD: photodetector; OSC: oscilloscope; ESA: electrical spectrum analyzer; OSA: optical spectrum analyzer.

engineering, as well as, exploration of new operating regimes (e.g. dispersion managed [152–154], sinc-, Nyquist- and zero-dispersion solitons [155–157]) will critically rely on the development of new approaches for dispersion engineering. Importantly, these modifications should be broadband (across hundreds of resonator modes), without jeopardizing the high Q-factor and without inducing unintentional AMXs.

Advanced techniques for *narrowband* dispersion modification in DKS-generating ring-type microresonators have been demonstrated including shifting of few resonance frequencies via mode-coupling between cross-polarized modes [71], fundamental and higher-order transverse modes [72], counter-propagating modes in corrugated resonators [74], as well as mode-hybridization in concentric resonators [77] and between modes in distinct resonators [75, 158]; these techniques have led to deterministic initiation of DKSs, higher-power efficiency, and novel nonlinear phenomena. Recently, the approach of coupling between counter-propagating modes in corrugated waveguide resonators has been extended, with single-mode control, to tens of resonator modes through inverse design [80] and Fourier-synthesis [81], representing a significant step

in broadband dispersion engineering, that may enable DKS in the future.

Complementary to methods developed for ring-type devices, Fabry-Perot (FP) microresonators with dispersive mirrors represent an attractive approach to broadband dispersion engineering: nearly 30 years ago, the advent of suitably designed Bragg mirrors for ultra-fast lasers represented a breakthrough in the field when faced with a similar challenge [159, 160]. So far, Bragg mirrors have also been applied to short fiber-based FP microresonators resulting in four-wave-mixing and stimulated Brillouin scattering [161], as well as the first demonstration of pulse-driven DKS [93]. Notably, recent advances led to the first integrated FP resonator with photonic crystal mirrors for comb generation [162] as well as FP microresonators with dispersion engineered reflecting structures, based on inverse design [163]. Despite all these major advances, a DKS-supporting platform whose broadband dispersion is not limited to effective waveguide (or whispering-gallery mode) dispersion has not yet been demonstrated.

Here, we demonstrate for the first time DKS generation in an integrated FP microresonator. Fabricated using a wafer-scale process, the microresonator is composed of two photonic crystal reflectors (PCRs) in a waveguide (Figure 2.1a). Significantly, across its entire bandwidth the dispersion of the resonator is dominated by the GDD contribution from the PCRs (not the waveguide), demonstrating new opportunities for dispersion engineering in a system capable of supporting DKSs. Further, the FP microresonator's intrinsic Q-factor, albeit not a record-high for an integrated device [164, 165], is on par with ring resonators fabricated in the same commercial platform. Our results establish integrated FP resonators as a powerful complement to ring resonators.

2.2 Resonator design and fabrication

The FP resonators are fabricated on-chip in a 800 nm thick silicon nitride layer and embedded in a fused silica cladding. The two PCRs are implemented as submicron-scale sinusoidal corrugations in a waveguide. Each corrugation period corresponds to a unit cell of the PCR, which is characterized by its length, mean width, and corrugation depth (Figure 2.2a ①). The periodic corrugation induces a photonic bandgap that defines the PCR's reflection bandwidth (Figure 2.2b); the length of the PCRs (~ 100 units cell per reflector) defines the reflectivity and thus the coupling strength to the waveguide that extends beyond the resonator to the chip's facets for light coupling. To design the PCRs, we employ finite element modeling to map the unit cell parameters to the photonic bandgap's opening and central frequency (Figure 2.2c), which permits choosing the desired parameters. In the present case, we choose a constant unit cell

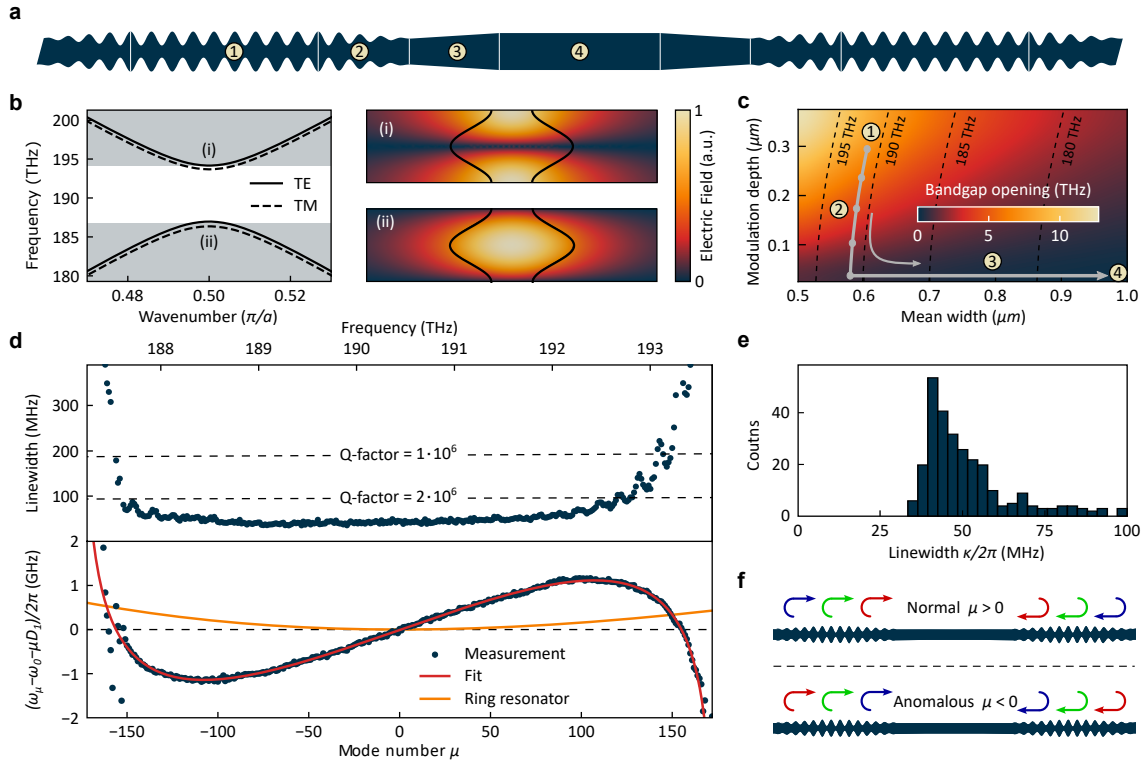


Figure 2.2 | Design of photonic crystal Fabry-Perot cavities. **a**, Schematic of a photonic crystal Fabry-Perot (FP) microresonator (not to scale), composed of photonic crystal reflectors (PCRs) ①, adiabatic tapers ②, linear tapers ③ and intracavity waveguide ④. **b**, Left panel: Illustration of a photonic band diagram for transverse electric (TE) and transverse magnetic (TM) modes. The wavenumber is given in units of π/a where a is the unit cell length. The bandgap, i.e. the reflection bandwidth is highlighted in white. Right panels: TM mode profiles (electric field strength) of upper and lower frequency modes of an example PCR unit cell with the corresponding cell contour overlaid in black (data based on finite element modeling) **c**, Map of the TM bandgap opening and center frequency as function of corrugation depth and mean width of the lattice cell for a fixed PCR period (i.e. cell length) of 475 nm (data based on finite element modeling). The PCR can be described by its trajectory through this design space (where the third dimension, the cell length, is not shown). **d**, TM mode family. Upper panel: Measured resonance linewidths as function of relative mode number μ (cf. main text). Lower panel: Measured dispersion (cf. main text) of a photonic crystal FP resonator with an mean free-spectral range $\overline{\text{FSR}} = D_1/2\pi = 18.55$ GHz. For comparison, the dispersion of an equivalent ring resonator with same $\overline{\text{FSR}}$ and waveguide cross-section identical to the FP's intracavity waveguide is plotted in orange, corresponding to the intracavity waveguide contribution to the FP resonator's total dispersion. A fit based on a coupled-mode description of the PCRs is shown in red (cf. [Supplementary information](#)). **e**, Histogram of the intrinsic resonance linewidths from **d** with a median value of 47 MHz corresponding to an intrinsic Q-factor of 4.0 million. **f**, Normal (anomalous) round-trip GDD corresponds to an increasing (decreasing) effective resonator length with increasing frequency.

for the main region of the PCR to create a bandgap centered around 1570 nm, the middle wavelength of our tunable CW laser. Note, that in principle each unit cell could have a different set of defining parameters, creating a large design space and permitting crafting of highly-customized resonators. An adiabatic taper (Figure 2.2a ②) connects the PCRs on both sides to an uncorrugated waveguide and suppresses losses due to the overlap mismatch between the fundamental guided mode of the uncorrugated waveguide and the PCR's fundamental Bloch mode [166, 167]. Transitioning from the PCR to the uncorrugated waveguide proceeds by gradually reducing the corrugation depth while simultaneously adjusting the mean width such that the bandgap center frequency is kept constant [168]. Finally, upon reaching zero-corrugation, the waveguide linearly tapers up to a width of 1.6 μm over length of 200 μm to reduce loss from sidewall-roughness scattering while still keeping a strong mode-confinement (Figure 2.2a ③). A 3400 μm long waveguide section forms the resonator cavity between the 2 PCRs (Figure 2.2a ④), defining the resonator's free-spectral range (FSR), in this case ~ 19 GHz which is within the K-frequency band and directly detectable by a photodiode and a microwave spectrum analyzer.

2.3 Experiments

To characterize the fabricated resonators, we first measure the intrinsic linewidths in a strongly undercoupled resonator (Figure 2.2d); undercoupling assesses the intrinsic cavity loss and permits direct comparison to (equally undercoupled) ring-type resonators fabricated through the same process. The PCR unit cell of this resonator is designed to have a period of 475 nm, width of 600 nm and corrugation depth of 300 nm. Owing to the narrow width of the unit cell, the PCR only supports the fundamental TE and TM transverse modes, which is desirable for reproducible resonator characteristics. The resonator's spectrum extends over 300 longitudinal modes and an intrinsic linewidth of 100 MHz or below is maintained over a bandwidth of 5 THz (40 nm), sufficient to support ultrashort femtosecond pulses. The median intrinsic (undercoupled) linewidth over the mirror bandwidth (here defined as the spectral interval where the linewidth is consistently below 100 MHz) is 47 MHz (Figure 2.2e). This corresponds to a median intrinsic Q-factor of $4.0 \cdot 10^6$, which is only limited by the ~ 0.1 dB cm^{-1} propagation loss inherent to the commercial platform used to fabricate the samples (cf. [Supplementary information](#)), and thus on-par with ring-resonators fabricated through the same commercial wafer-scale process.

Next, we measure the resonator's dispersion as shown in Figure 2.2d in terms of the

integrated dispersion $D_{\text{int}} = \omega_{\mu} - \omega_0 - \mu D_1$, which quantifies the deviation of the resonance frequencies ω_{μ} from a dispersion-free equidistant frequency grid as a function of the relative mode-number μ . In this representation, anomalous (normal) dispersion appears as a convex (concave) curve. The strength of the local dispersion at a specific frequency can be estimated by choosing $D_1/(2\pi)$ to be the local FSR and expand $D_{\text{int}} \approx \frac{1}{2}\mu^2 D_2$ around this frequency. Anomalous (normal) dispersion is then indicated by positive (negative) D_2 . Here, μ is chosen such that $\mu = 0$ coincides with the center of the reflector's bandwidth and $D_1/(2\pi)$ is chosen to be approximately the average $\overline{\text{FSR}}$ over the reflector's bandwidth. For comparison, Figure 2.2d also shows the dispersion curve of an equivalent ring-type resonator (with the same $\overline{\text{FSR}}$, the same waveguide cross-section as the FP intracavity waveguide and negligible effect of curvature on dispersion), corresponding to the intracavity waveguide contribution to the FP resonator's total dispersion; the marked difference between both dispersion curves shows the dominating impact of the PCRs on the FP resonator's dispersion. The exact contribution of the PCRs to the dispersion can be calculated through their complex reflection coefficient (cf. [Supplementary information](#)), which matches well the observations (also indicated in Figure 2.2d as "Fit"). With the current PCR design, the resonator provides both normal and anomalous dispersion regimes, independently of the anomalous background contribution from the intracavity waveguide. This may be understood as a wavelength-dependent effective reflection depth in the PCRs (Figure 2.2f).

Moreover, the measured dispersion of the resonance frequencies in Figure 2.2d is free of strong local deviations such as AMXs which can arise from coupling between frequency degenerate counter-propagating modes or coupling between different transverse mode families. Here, these two mechanisms are absent: in contrast to rings, the FP resonator has no distinct counter-propagating mode, which leads to the striking absence of unintentional mode-splitting often observed in rings (cf. [Supplementary information](#)); higher order transverse mode are efficiently suppressed by the single-mode nature of the PCRs. These features contribute to achieving a smooth anomalous dispersion, which in conjunction with the high-Q provide favorable conditions for DKS formation [44].

To generate DKSs, a more strongly coupled resonator with a 15% shorter input PCR (but with otherwise identical geometry) and a 56 MHz median total linewidth is used for more efficient operation. The setup for this experiment is shown in Figure 2.1c: The resonator is pumped using a tunable laser in the transverse-magnetic (TM) polarization in the anomalous dispersion regime (local $D_2/(2\pi) = 210$ kHz) at a wavelength

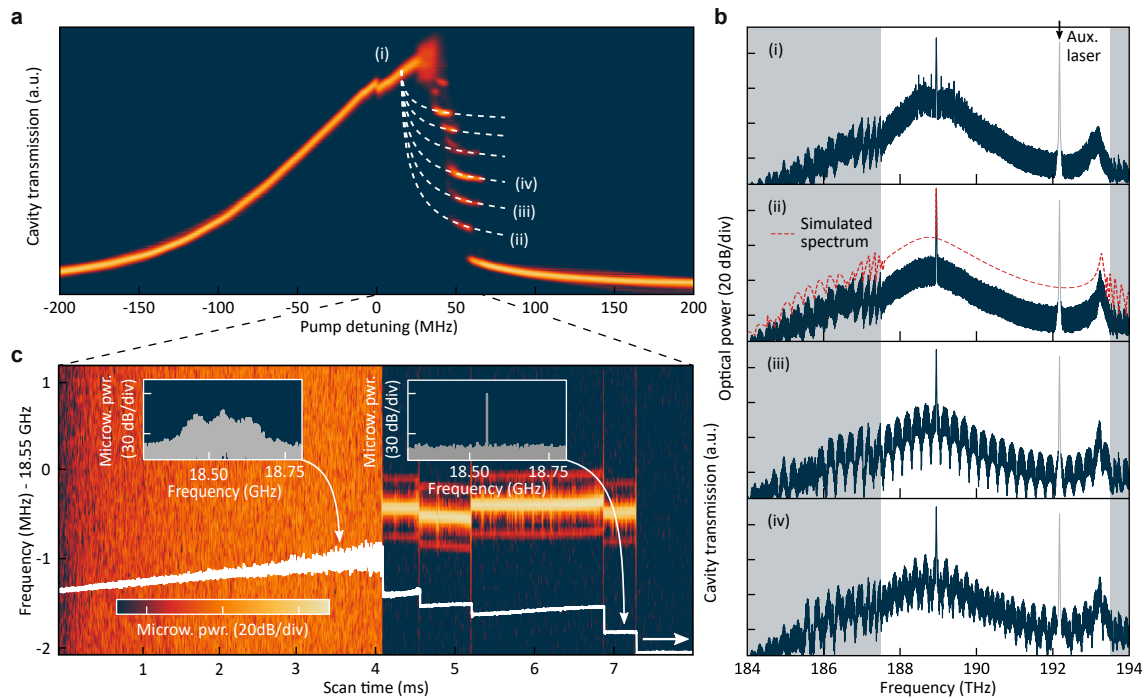


Figure 2.3 | Dissipative Kerr soliton in a photonic crystal Fabry-Perot resonator. **a**, Heat-map compiled from a 100 transmission traces, highlighting multiple possible intracavity power evolutions as a function of pump detuning. The step-like features present at ~ 50 MHz detuning indicate quantized power levels, a canonical signature of DKS formation. **b**, Optical spectra of modulation instability (i), single (ii), 2- (iii) and 3- (iv) soliton states. A dispersive wave is present on the blue-side of the spectra, due to the local presence of strong normal dispersion. The auxiliary laser's line (cf. [Supplementary information](#)), is grayed out for clarity; the nominal PCR bandwidth is highlighted in white. The spectrum obtained from numerical simulations based on the measured cavity parameters (cf. [Supplementary information](#)) is shown in red, offset by +10 dB, corresponding to a pulse of ~ 300 fs. **c**, Spectrogram showing the evolution of the microwave beatnote signal (~ 18.5 GHz) as a function of the pump detuning. Overlaid in white is the corresponding resonator transmission signal. The insets show the beatnote in the modulation instability and soliton regime respectively (resolution bandwidth: 100 kHz).

of 1587 nm (188.9 THz). Repeatedly scanning the pump laser (150 mW on-chip) from blue- to red-detuned across a resonance, we record the resonator transmission signals and superpose them in Figure 2.3a. After an initial modulation instability (MI) state (i), characteristic step-features (ii-iv etc.) are visible, which are indicative of DKS formation [138]; each step corresponding to an integer numbers of solitons in the resonator that can be generated during a laser scan. The corresponding MI spectrum, the comb spectrum of a single soliton, as well as more structured comb spectra of multiple-soliton states are shown in Figure 2.3b where the white background highlights the nominal PCR bandwidth.

Initially all spectra exhibit a periodic modulation of their envelope caused by reflections between PCR and chip facet, which has been removed before plotting (cf. [Supplementary information](#)); although of no concern here, the modulation could be avoided by anti-reflection coating the chip's facet, index-matching fluid or evanescent waveguide coupling if necessary. From fitting the single DKS's spectrum with a sech^2 envelope (Figure 2.3b (ii)) we estimate the transform-limited soliton pulse duration to be ~ 300 fs. Close to the blue-edge of the resonator's bandwidth, we observe a dispersive wave [54] as expected from the normal dispersion in this spectral region. Due to a relaxed phase-matching condition outside the high-reflectivity bandwidth, all spectra extend beyond the nominal PCR bandwidth, strongly modulated by the sidelobes of the PCRs (cf. [Supplementary information](#)). To further confirm DKS generation, we record the microwave pulse repetition rate beatnote as a function of detuning (Figure 2.3c). As expected, the beatnote transitions from a high-noise to a narrow-linewidth signal, when entering into a DKS state (with each subsequent transition to a lower number of solitons corresponding to a slight change of the repetition rate). Finally, we also observe the formation of soliton crystals [140] (Figure 2.4a), a state commonly observed in traveling-wave microresonators where a self-organized train of equidistant soliton pulses circulates inside the resonator, (effectively increasing the pulse repetition rate and hence the comb line spacing by an integer factor). These observations further establish the standing-wave FP resonator as a DKS platform and strengthen the link to travelling-wave ring-type resonators.

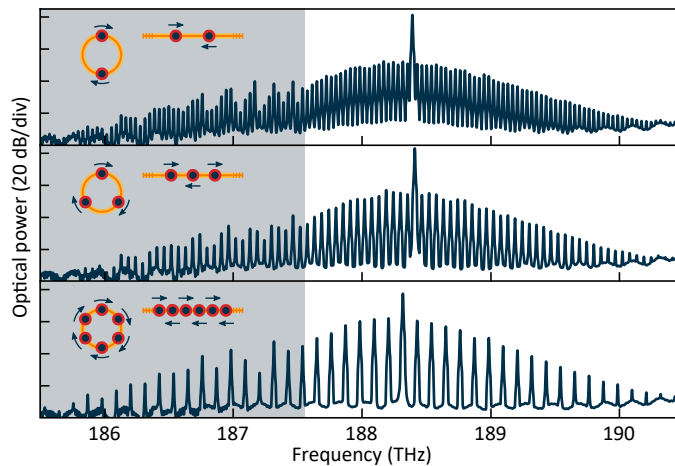


Figure 2.4 | Soliton crystals. Recorded spectra of 2, 3 and 6-soliton crystal states obtained by pumping at slightly different frequencies. The PCR’s nominal bandwidth is highlighted by a white background. A snap-shot crystalline distribution of DKSs in a linear FP cavity is shown as an inset along with an equivalent ring configuration.

Indeed, the nonlinear dynamics of standing wave-resonators is similar to the travelling-wave case, with an additional phase-shift due to cross-phase modulation between counter-propagating waves proportional to the average intracavity power [93, 169]; this effect can be compensated by a slight change in the pump laser detuning. Different from a conventional ring-type resonator, the dispersion in the present resonator includes localized and distributed contributions from the PCRs and the connecting waveguide, respectively (cf. [Supplementary information](#)). Here, as the impact of both, a single reflection off of a PCR or a single propagation through the waveguide, have negligible effect on the DKS pulse, they can be lumped together. This implies that established mean-field models for ring resonators can also be used for describing the present FP resonators, with the inclusion of the aforementioned phase-shift.

Complementing the experimental study of DKS formation in the new resonator platform we perform numeric simulations based on the frequency-domain formulation of the LLE [84, 96], which readily permits inclusion of the spectrally-dependent measured dispersion and linewidths. The simulated spectrum and pulse shape of a single soliton state are shown in Figure 2.4b. The simulation reproduces all spectral features (compared to the general envelope in Figure 2.3b (ii-iv) and Figure 2.4a) including the dispersive wave and the spectral extension beyond the nominal PCR bandwidth. The simulated pulse shows only minor deviations from DKSs generated in resonators with unlimited spectral support, corroborating that the reflectors’ bandwidth is sufficient to support femtosecond DKS pulses.

2.4 Discussion

In summary, we have shown for the first time DKS formation in a chip-integrated FP resonator. The resonator's dispersion is not defined by waveguide dispersion, but by its PCR mirrors. Through careful design, we achieve a high intrinsic Q-factor of 4 million, matching that of traveling wave-type resonators fabricated in the same wafer-scale commercial foundry process. The absence of distinct frequency degenerate counter-propagating modes in the FP geometry and the single mode nature of the PCRs avoids unintentional AMXs that can inhibit DKS formation. Under CW-driving, we observe single, multiple (hence colliding) DKS pulses, as well as soliton crystals. This establishes integrated FP resonators as a new topology for DKS generation that can add to and complement existing ring-resonator based approaches. As each unit cell of the PCRs can, in principle, be individually adjusted, this opens a large design space for future tailoring of dispersion, spectrally dependent Q-factors and filters, bandwidth extension through chirped reflectors or broadband phase-matching, while allowing for compact integration. Future efforts may benefit from insights obtained in the context of mirrors for ultrafast laser [159, 160] and inverse design approaches [80, 163]. With relevance to quantum photonics, bio-chemical sensing and astronomical spectrograph calibration, the presented results provide a resonator platform that, through customized PCRs, may lead to DKSs at visible wavelengths, and at other wavelengths that are currently inaccessible due to unsuitable effective waveguide dispersion. Besides DKS, the integrated FP platform could also prove useful for microresonator frequency combs via cascaded four-wave mixing [37] and switching waves [170–172], as well as integrated optical parametric oscillators [173] and optical harmonic generation [174]. Immediate further research opportunities leveraging the specific characteristics of the new resonators include dispersion managed solitons [152–154], sinc-, Nyquist- and zero-dispersion solitons [155–157], nonlinear ‘gain-through-loss’ [175], slow-light [135], spectral engineering [80, 81] and filter-driven pulse formation [176, 177], which bodes well for integrated broadband and ultrafast light sources.

2.5 Supplementary information

2.5.1 Sample fabrication

The samples were fabricated commercially by LIGENTEC SA using UV optical lithography. When fabricating devices with features close to the resolution limit of optical lithography, deviations between designed and fabricated geometry can arise that, if

unaccounted for, can significantly alter device performance. In the case of the PCRs presented in this work, this results in a shift in the mean waveguide width and a reduction of the effective corrugation depth of the cells. The parameterized geometry of the PCRs enables us to correct for this by establishing an interpolation table between designed and fabricated geometries, which is used to preemptively adjust the mask in order to achieve the targeted final geometry. Thus, through careful process calibration, it is possible to fabricate the microresonators in a wafer-level process using optical lithography without the need for e-beam lithography, which photonic crystal devices often require.

2.5.2 Comparison between ring and Fabry-Perot resonators: Q-factor and line splitting.

The maximum propagation loss specified by the foundry is 0.2 dB cm^{-1} at 1550 nm for a single-mode waveguide (cross-section $1.0 \times 0.8 \text{ }\mu\text{m}^2$), corresponding to a minimum intrinsic resonator Q-factor of 1.7 million. We establish our own baseline by characterizing a set of ring resonators with a waveguide cross-section of $1.6 \times 0.8 \text{ }\mu\text{m}^2$, identical to the intracavity waveguide of our FP microresonators, and measure a median intrinsic Q-factor of 3.6 million for the TM mode corresponding to a propagation loss of $\sim 0.1 \text{ dB cm}^{-1}$. With a radius of $151.5 \text{ }\mu\text{m}$ (150 GHz free spectral range), the effect of the ring's waveguide's curvature on propagation loss and dispersion is negligible. In the manuscript, we show that the FP microresonators' intrinsic Q-factor exceeds this, demonstrating the negligible additional losses induced by the photonic crystal reflectors. We attribute the marginal higher Q-factor in the FP microresonators to the absence of random back-scattering to distinct frequency degenerate counter-propagating modes, a phenomenon which induces mode-splitting and broadens the apparent lineshape if the splitting is unresolved.

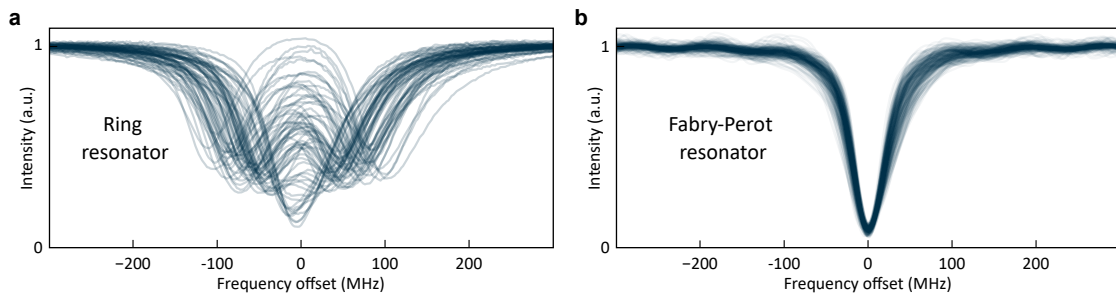


Figure 2.5 | Superposed normalized line shapes of 150 GHz ring (a) and Fabry-Perot microresonators (b).

The difference between the ring and FP microresonator can be observed in Figure 2.5 where superpositions of the lineshapes recorded between 1520 nm and 1605 nm in either geometry are shown. While both ring and FP microresonators have similar intrinsic linewidths, the ring resonator (Figure 2.5b) exhibits strong and random line splitting (caused by random backscattering e.g. from surface roughness) whereas the FP microresonator is virtually free of such effects due to the absence of frequency degenerate counter-propagating modes.

2.5.3 Resonator dispersion and coupling

The introduction of a sub-wavelength periodic perturbation via the PCR couples the forward- and backward-propagating waves together through a coupling coefficient κ which can be estimated from the half-bandgap opening $\delta\omega/2$ divided by the group velocity of the unperturbed waveguide [178]:

$$|\kappa| \approx \frac{\delta\omega}{2} \frac{d\beta}{d\omega} \Big|_{\omega=\omega_0} \quad (2.1)$$

where ω_0 is the bandgap center frequency such that $\beta(\omega_0) = \pi/\Lambda$, Λ being the PCR period. Within the bandgap the eigenvalues of the coupled system are real, and the waves decay exponentially with rate $\gamma = -\sqrt{|\kappa|^2 - \delta^2}$ where $\delta = \beta(\omega) - \pi/\Lambda$ is the detuning parameter. By introducing the appropriate boundary conditions, the reflection and transmission coefficients can be obtained as a function of the PCR length l :

$$r = \frac{\kappa^* \cdot \sinh \gamma l}{\gamma \cdot \cosh \gamma l + j\delta \cdot \sinh \gamma l} \quad (2.2)$$

$$t = \frac{\gamma}{\gamma \cdot \cosh \gamma l + j\delta \cdot \sinh \gamma l} \quad (2.3)$$

$$\tan \angle r = -\frac{\delta}{\gamma} \cdot \tanh \gamma l \quad (2.4)$$

$$\tan \angle t = -\frac{\delta}{\gamma} \cdot \tanh \gamma l \quad (2.5)$$

The round-trip phase of the FP microresonator is then given by the sum of the PCRs' reflection and the waveguide's contributions:

$$\phi = 2L\beta + 2 \arctan \left(\frac{\delta}{\gamma} \cdot \tanh \gamma l \right) \quad (2.6)$$

where L is the one-way length of the intracavity waveguide, and the input and output PCRs are assumed to be identical.

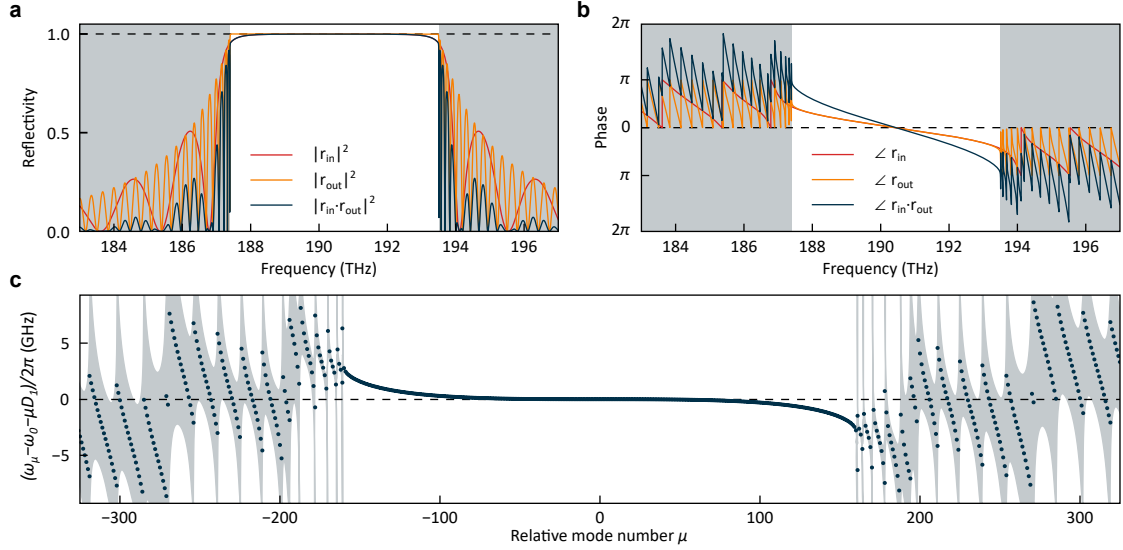


Figure 2.6 | Photonic Crystal Reflector. Magnitude (a) and phase (b) of the reflection coefficients of the Fabry-Perot microresonator’s input PCR (red), output PCR (orange) and a combination thereof computed from eq. 2.2. c, Integrated dispersion computed from the complex PCR reflection coefficients shown in b. The associated resonance linewidths are displayed as a grey zone, showing the region of relaxed phase matching condition.

The resonator roundtrip GDD = $\partial^2 \phi / \partial \omega^2$ therefore also contains the sum of the contributions from the PCRs (two reflections) and of the waveguide between the PCRs (back and forth). It is related to the microresonator dispersion D_2 via $\text{GDD} = -2\pi D_2 / D_1^3$. For DKS generation we drive the resonator at a wavelength where the waveguide single pass contribution to the GDD is -445 fs^2 , and the contribution of the PCR from a single reflection is -2170 fs^2 . For both values, $\tau_0^2 \gg |\text{GDD}|$ for a DKS duration of $\tau_0 \approx 100 \text{ fs}$, i.e. the effect of a single reflection or a single pass through the waveguide has negligible impact on the pulse; therefore the effect of both contributions of the dispersion can be lumped together.

The fit in Figure 2d of the main manuscript is obtained by fitting the resonance frequencies against their mode number $\mu_0 + \mu = \phi / (2\pi)$ using eq. 2.6 and expanding the wavenumber as $\beta(\omega) = \beta_0 + \beta_1(\omega - \omega_0) + \frac{1}{2}\beta_2(\omega - \omega_0)^2$. The input and output PCR contributions are accounted for individually as they have different lengths (the input PCR is shorter to optimize coupling). The PCR reflection magnitude and phase computed from the fit parameters are shown in Figure 2.6a and Figure 2.6b respectively, while

the integrated dispersion (computed by numerically inverting of eq. 2.6) is shown in Figure 2.6c.

The coupling coefficient κ_e to the FP microresonator can be obtained from the transmission coefficient t :

$$\kappa_e \approx \frac{|t|^2}{T_R} = \frac{c|t|^2}{2Ln_g} \quad (2.7)$$

where T_R is the microresonator round-trip time. The coupling coefficient of an FP microresonator is

$$\eta = \frac{\kappa_e}{\kappa_0 + \kappa_e + \kappa'_e} < 1 \quad (2.8)$$

where κ_0 describes the propagation loss and κ'_e the finite reflectivity of the second reflector; it can be adjusted to $0 < \eta < 1$ and critical coupling ($\eta = 1/2$) can be reached. For symmetric reflectors the coupling coefficient is

$$\eta = \frac{\kappa_e}{\kappa_0 + 2\kappa_e} < 0.5 \quad (2.9)$$

and critical coupling can only be achieved asymptotically in the limit of strong external coupling ($\kappa_e \gg \kappa_0$). Note that eq. 2.9 also holds for evanescent coupling (e.g. via a directional coupler), where the light in the microresonator encounters the coupler characterized by κ_e twice per roundtrip; in this case the finite reflectivity of both reflectors is included in κ_0 .

2.5.4 Soliton generation and soliton spectra

In order to tune into the respective solitons states without the requirement for a rapid tuning scheme (i.e. faster than the resonator thermal decay rate), we use the established auxiliary laser method [121]. In this scheme a secondary auxiliary laser (1560 nm) coupled to the blue-side of a resonance of the TE mode family (main manuscript, Figure 1c), of similar on-chip power (150 mW) and orthogonal to the TM-polarized pump light, is used to thermally stabilize the resonator and conveniently mitigate thermal shifts occurring when tuning the main pump laser by keeping the total intracavity power nearly constant.

All soliton spectra show a modulated spectral envelope (Figure 2.7a) with a period and amplitude of ~ 207 GHz and ~ 1.8 dB respectively. We attribute this to reflections between the chip facet and the PCR, forming a low-Q cavity in the connecting waveguide. Indeed, the period and amplitude of the modulation correspond to a cavity of length $\sim 380 \mu\text{m}$ and a facet reflectivity of approximately 4.5% respectively, which is in

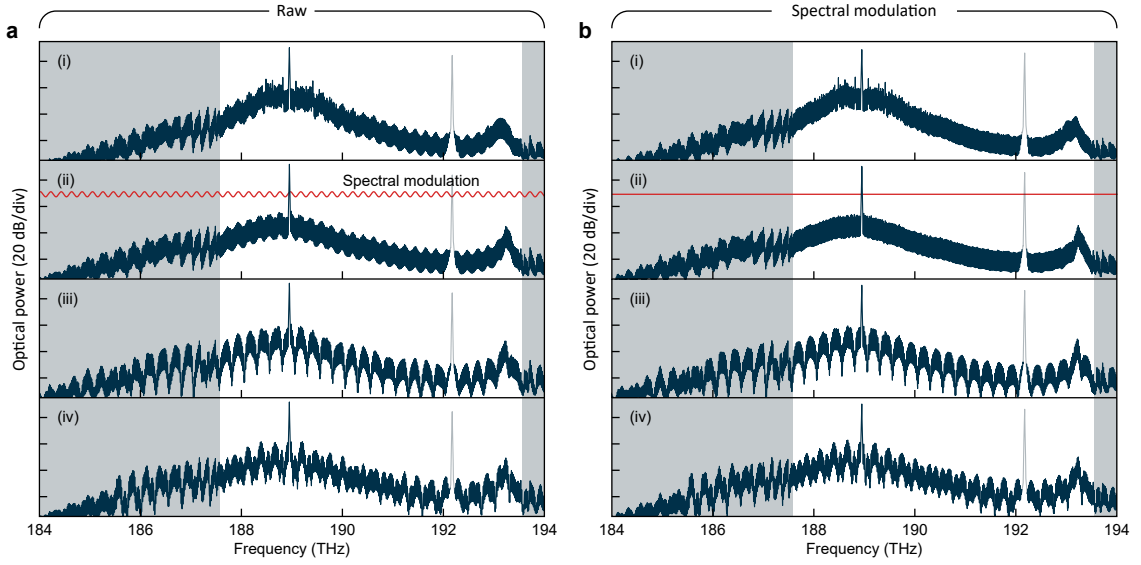


Figure 2.7 | Fabry-Perot microresonator comb spectra. Optical spectra of modulation instability (i), single (ii), 2- (iii) and 3- (iv) soliton states before (a) and after (b) subtraction (in dB scale) of the spectral modulation from the low-Q cavity shown in red in panel (ii).

excellent agreement with the true facet distance and the expected Fresnel reflection at the chip-air interface. Figure 2.7 shows the modulation instability and DKS spectra before and after numerical subtraction (in dB scale) of the modulation envelope. As can be seen, subtracting this modulation yields the smooth spectra expected of DKS states while, the remaining structuration of the spectra outside of the nominal PCR bandwidth (highlighted in white) is inherent to the intracavity spectra and arises from the discontinuous dispersion profile created by the PCR side-lobes (see. Figure 2.6c). The correction described above is applied to all spectra in Figure 3b and 4 of the main manuscript.

2.5.5 Numerical simulation

For the numerical simulation presented in the manuscript, the frequency-domain formulation of the Lugiato–Lefever Equation (LLE) for standing wave resonators was used [93]:

$$\frac{\partial a_\mu}{\partial \tau} = - \left[\kappa_\mu / \kappa_0 + i\zeta_\mu - 2i \sum_{\mu'} |a_{\mu'}| \right] a_\mu + i \sum_{\mu', \mu''} a_{\mu'} a_{\mu''} a_{\mu' + \mu'' - \mu}^* + \delta_{0\mu} f \quad (2.10)$$

where a_μ denote the normalized field amplitudes, κ_μ the total linewidth of mode μ and f the normalized pump power. This equation only differs from the traveling wave case by the additional phase shift $-2i \sum_{\mu'} |a_{\mu'}|$, which arises from the cross-phase modu-

lation between counter-propagating waves and which can be compensated for by the normalized pump detuning ζ_μ . The use of this frequency-domain formulation of the LLE enables straight-forward inclusion of arbitrary dispersion and linewidth profiles — such as those exhibited by our FP microresonators and shown in Figure 2.6c — though the mode-dependent loss κ_μ/κ_0 and detuning $\zeta_\mu = 2(\omega_\mu - \omega_p - \mu D_1)/\kappa_0$ terms respectively.

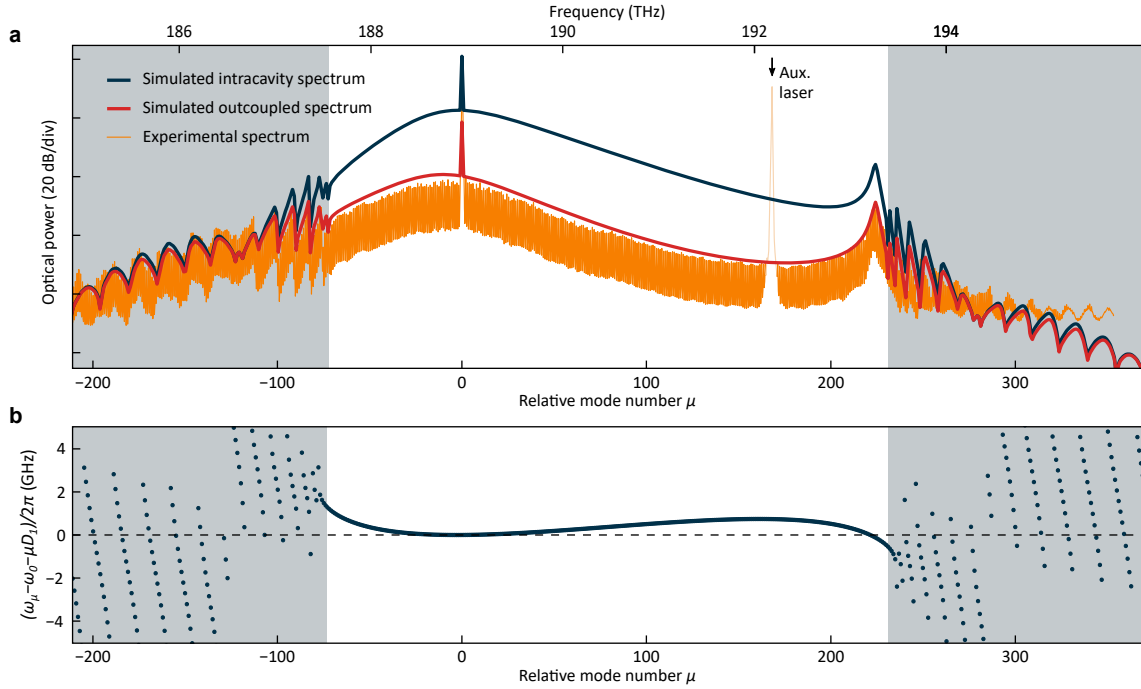


Figure 2.8 | Numerical Simulation. **a**, Simulated intracavity (blue), simulated outcoupled (red) and experimentally measured (orange) spectra. **b**, Integrated dispersion expanded around the pumped mode, as used in eq. 2.10 for the simulation results shown in **a**.

To obtain the outcoupled spectrum as measured experimentally, one must multiply the intracavity spectrum by the output PCR transmission ($|t_{out}|^2 = 1 - |r_{out}|^2$). The simulated intracavity and outcoupled spectra as well the experimentally recorded spectrum are compared in Figure 2.8a showing excellent match between simulation and experiment. Figure 2.8b shows the integrated dispersion profile expanded around the pumped mode as used in eq. 2.10.

Chapter 3

Sideband injection locking in microresonator frequency combs

Thibault Wildi¹, Alexander E. Ulanov¹, Nicolas Englebert², Thibault Voumard¹ and Tobias Herr^{1,3}

¹ *Deutsches Elektronen-Synchrotron DESY, Notkestr. 85, 22607 Hamburg, Germany*

² *OPERA-Photonics, Université libre de Bruxelles (U.L.B.), 50 Avenue F. D. Roosevelt, CP 194/5, B-1050 Brussels, Belgium*

³ *Physics Department, Universität Hamburg UHH, Luruper Chaussee 149, 22761 Hamburg, Germany*

Published in *APL Photonics* Vol. 8, Issue 12, pp. 120801 on December 12, 2023

<https://doi.org/10.1063/5.0170224>

Author contributions

T.W. and T.H. conceived the experiment. T.W., T.H., and N.E. developed the analytical model. T.W. designed the setup and the photonic chip, performed the experiments, analyzed the data, and performed numerical simulations. A.U., B.R., and T.V. supported the experiments and provided insight into the data analysis. T.H. supervised the work. T.W. and T.H. prepared the manuscript with input from all authors.

Abstract

Frequency combs from continuous-wave-driven Kerr-nonlinear microresonators have evolved into a key photonic technology with applications from optical communication to precision spectroscopy. Essential to many of these applications is the control of the comb's defining parameters, i.e., carrier-envelope offset frequency and repetition rate. An elegant and all-optical approach to controlling both degrees of freedom is the suitable injection of a secondary continuous-wave laser into the resonator onto which one of the comb lines locks. Here, we study experimentally such sideband injection locking in microresonator soliton combs across a wide optical bandwidth and derive analytic scaling laws for the locking range and repetition rate control. As an application example, we demonstrate optical frequency division and repetition rate phase-noise reduction to three orders of magnitude below the noise of a free-running system. The presented results can guide the design of sideband injection-locked, parametrically generated frequency combs with opportunities for low-noise microwave generation, compact optical clocks with simplified locking schemes and more generally, all-optically stabilized frequency combs from Kerr-nonlinear resonators.

3.1 Introduction

Continuous-wave (CW) coherently-driven Kerr-nonlinear resonators can create temporally structured waveforms that circulate stably without changing their temporal or spectral intensity profile. The out-coupled optical signal is periodic with the resonator roundtrip time T_{rep} and corresponds to an optical frequency comb [4, 37, 179–181], i.e. a large set of laser frequencies spaced by the repetition rate $f_{\text{rep}} = T_{\text{rep}}^{-1}$. One important class of such stable waveforms are CW-driven dissipative Kerr-solitons (DKSs), which have been observed in fiber-loops [112], traveling- and standing-wave microresonators [44, 98] and free-space cavities [182]. In microresonators these soliton microcombs [110] provide access to low-noise frequency combs with ultra-high repetition rates up to THz frequencies, enabling novel applications in diverse fields including optical communication [144, 183], ranging [146, 147, 184], astronomy [150, 151], spectroscopy [149], microwave photonics [45, 148], and all-optical convolutional neural networks [185].

In a CW-driven microresonator, the comb's frequency components are defined by $f_{\mu} = f_{\text{p}} + \mu f_{\text{rep}}$, where f_{p} denotes the frequency of the central comb line and μ is the index of the comb line with respect to the central line (μ is also used to index the res-

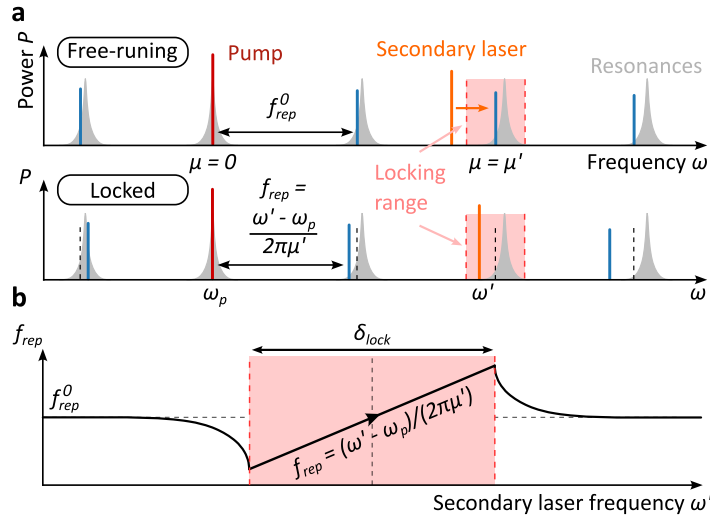


Figure 3.1 | Principles of sideband injection locking. **a**, In a free-running comb, the central comb line is defined by the pump laser around which equidistant comb lines, spaced by the free-running repetition rate f_{rep}^0 , are formed. If a secondary injection laser of frequency ω' is brought close to one of the comb lines (within injection locking range), then the comb locks to the injecting laser, modifying the repetition rate as indicated. **b** Outside the locking range, $f_{\text{rep}} = f_{\text{rep}}^0$ is unaffected by the secondary laser. Inside the locking range, it follows a characteristic tuning behavior with a linear dependence on the injecting laser frequency ω' .

onances supporting the respective comb lines). For many applications [4, 181], it is essential to control both degrees of freedom in the generated frequency comb spectra, i.e. the repetition rate f_{rep} and the central frequency f_p (which together define the comb's carrier-envelope offset frequency). Conveniently, for Kerr-resonator based combs, f_p is defined by the pump laser frequency $f_p = \omega_p / (2\pi)$. However, the repetition rate f_{rep} depends on the resonator and is subject to fundamental quantum mechanical as well as environmental fluctuations.

A particularly attractive and all-optical approach to controlling f_{rep} is the injection of a secondary CW laser of frequency ω' into the resonator, demonstrated numerically [186] and experimentally [187]. If ω' is sufficiently close to one of the free-running comb lines (sidebands) $f_\mu \approx \omega' / (2\pi)$, i.e., within *locking range*, the comb will lock onto the secondary laser, so that $f_\mu \rightarrow \omega' / (2\pi)$. The repetition rate is then $f_{\text{rep}} = (\omega_p - \omega') / (2\pi\mu')$, with μ' denoting the index of the closest resonance to which the secondary laser couples, cf. Figure 3.1a. This frequency division [188] of the frequency interval defined by the two CW lasers (as well as their relative frequency noise) by the integer μ' can give rise to a low-noise repetition rate f_{rep} . In previous work, sideband injection locking has been leveraged across a large range of photonic systems, including

for parametric seeding [189, 190], dichromatic pumping [191], optical trapping [186, 192, 193], synchronization of solitonic and non-solitonic combs [142, 194], soliton crystals [187], soliton time crystals [143], multi-color solitons [195] and optical clock-works by injection into a DKS dispersive wave [81]. Related dynamics also govern the self-synchronization of comb states [196, 197], the binding between solitons [198], modified soliton dynamics in the presence of Raman-effect [199] and avoided mode-crossings [200], as well as the respective interplay between co- [201] and counter-propagating solitons [202–204] and multi-soliton state-switching [205]. Moreover, sideband injection locking is related to modulated and pulsed driving for broadband stabilized combs [93, 94, 150], as well as spectral purification and non-linear filtering of microwave signals [206, 207] via DKS. Despite the significance of sideband injection locking, a broadband characterization and quantitative understanding of its dependence on the injecting laser are lacking, making the design and implementation of such systems challenging.

In this work, we study the dynamics of sideband injection locking with DKS combs. Our approach leverages high-resolution coherent spectroscopy of the microresonator under DKS operation, enabling precise mapping of locking dynamics across a large set of comb modes, including both the central region and wing of the comb. We derive the sideband injection locking range’s dependence on experimentally accessible parameters and find excellent agreement with the experimental observation and with numeric simulation. Specifically, this includes the square dependence on the mode number, the square-root dependence on injection laser and DKS spectral power, as well as, the associated spectral shifts.

In addition, we demonstrate experimentally optical frequency division and repetition rate phase-noise reduction in a DKS state to three orders of magnitude below the noise of a free-running system.

3.2 Results

To first explore the sideband injection locking dynamics experimentally, we generate a single DKS state in a silicon nitride ring-microresonator. In the fundamental TE modes, the resonator is characterized by a quality factor of $Q \approx 2$ million (linewidth $\kappa/(2\pi) \approx 100$ MHz), a free-spectral range (FSR) of $D_1/(2\pi) = 300$ GHz and exhibits anomalous group velocity dispersion $D_2/(2\pi) = 9.7$ MHz so that the resonance frequencies are well-described by $\omega_\mu = \omega_0 + \mu D_1 + \mu^2 \frac{D_2}{2}$ ($1.6 \times 0.8 \mu\text{m}^2$ cross-section, $76 \mu\text{m}$ radius). To achieve deterministic single soliton initiation, the microresonator’s inner perimeter is weakly corrugated [74, 134]. The resonator is critically coupled and driven by a CW

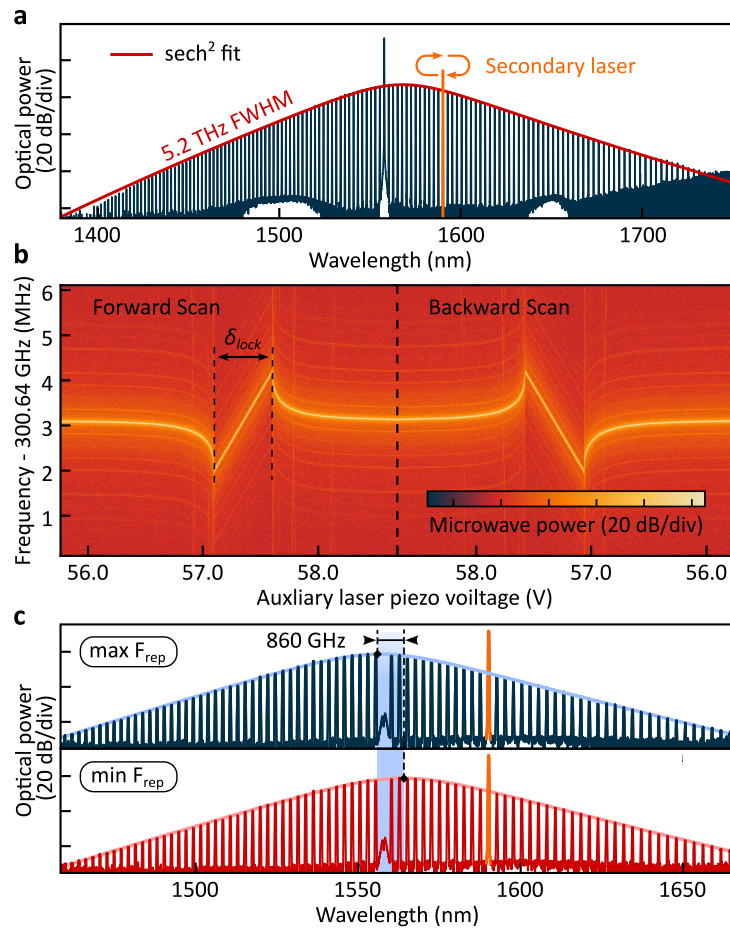


Figure 3.2 | Soliton sideband injection locking. **a**, Single DKS comb spectrum, following a sech^2 envelope, with a full-width-at-half-maximum (FWHM) of 5.2 THz, corresponding to a ~ 60 fs pulse. The secondary laser is introduced in the spectral wing of the soliton and scanned across the μ' th sideband. **b**, Repetition rate beatnote observed while the secondary laser is scanned across the μ' th sideband. The locking bandwidth corresponds to the region of linear evolution of the repetition rate beatnote. **c**, Spectra of two sideband injection-locked DKS states from either end of the locking range, exhibiting a differential spectral shift of 860 GHz. Note that a filter blocks the central pump component ω_p .

pump laser (~ 300 kHz linewidth) with on-chip power of 200 mW at 1557 nm (pump frequency $\omega_p/(2\pi) = 192.5$ THz) [44]. The generated DKS has a 3 dB bandwidth of approximately 5.2 THz (cf. Figure 3.2a) corresponding to a bandwidth limited pulsed of ~ 60 fs duration. The soliton spectrum closely follows a sech^2 envelope and is free of dispersive waves or avoided mode crossings. The spectral center of the soliton does not coincide with the pump laser but is slightly shifted towards longer wavelengths due to the Raman self-frequency shift [208, 209].

A secondary CW laser (~ 300 kHz linewidth), tunable both in power and frequency (and not phase-locked in any way to the first CW laser), is then combined with the pump laser upstream of the microresonator and scanned across the μ' th sideband of the soliton microcomb, as illustrated in Figure 3.2a. The spectrogram of the repetition rate signal recorded during this process is shown in Figure 3.2b, for $\mu' = -13$, and exhibits the canonical signature of locking oscillators [210] (see Section 3.4.2 of the [Supplementary information](#), for details on the measurement of f_{rep}). Specifically, the soliton repetition rate f_{rep} is observed to depend linearly on the auxiliary laser frequency ω' over a locking range δ_{lock} following $f_{\text{rep}} = \frac{1}{2\pi} \frac{\omega_p - \omega'}{\mu'}$. Within δ_{lock} , the soliton comb latches onto the auxiliary laser, such that the frequency of the comb line with index μ' is equal to the secondary laser frequency. The locking behavior is found to be symmetric with respect to the scanning direction, and no hysteresis is observed. Figure 3.2c shows the optical spectra of two sideband injection-locked DKS states, with the secondary laser positioned close to the respective boundaries of the locking range. A marked shift of the spectrum of 860 GHz is visible when going from one state to the other. As we discuss below and in Section 3.4.3 of the [Supplementary information](#), the spectral shift in the presence of non-zero group velocity dispersion modifies the soliton's group velocity and provides a mechanism for the DKS to adapt to the repetition rate imposed by the driving lasers.

Having identified characteristic features of sideband injection locking in our system, we systematically study the injection locking range and its dependence on the mode number μ' to which the secondary laser is coupled. To this end, a frequency comb calibrated scan [211] of the secondary laser's frequency ω' across many DKS lines is performed. The power transmitted through the resonator coupling waveguide is simultaneously recorded. It contains the ω' -dependent transmission of the secondary laser as well as the laser's heterodyne mixing signal with the DKS comb, which permits retrieving the locking range δ_{lock} .

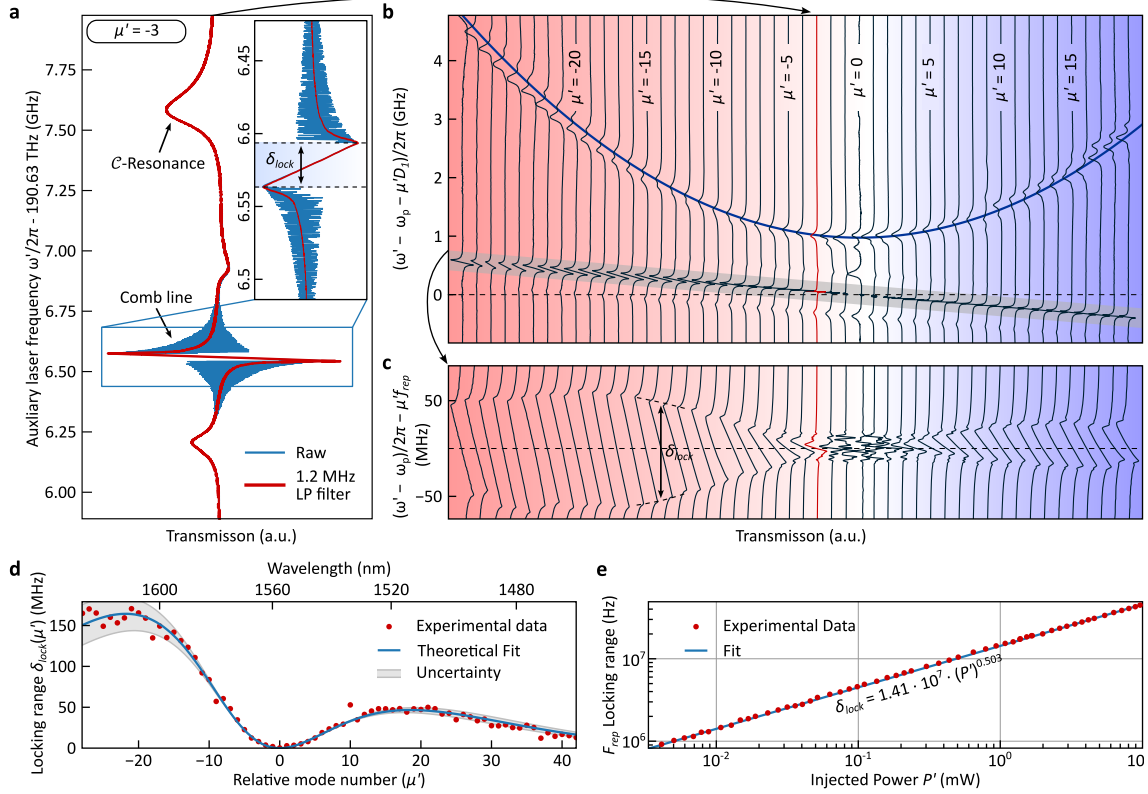


Figure 3.3 | DKS sideband injection locking dynamics. **a**, Transmission obtained when the secondary laser frequency ω' is scanned in the vicinity of comb line $\mu' = -3$. The trace contains features indicating the position of the microresonator resonance frequency $\omega_{-3}/(2\pi)$ and of the soliton comb line frequency f_{-3} as well as the sideband injection locking range (see main text for details). **b**, Similar to **a** but for all μ' that can be reached by the scanning laser frequency ω' . In this representation, the resonance frequencies form a quadratic integrated dispersion profile (due to anomalous dispersion) while the equidistant soliton microcomb lines (highlighted in gray and expanded in panel **b**) form a straight line, enabling retrieval of pump laser detuning and microcomb repetition rate (see main text for details). **c**, Zoom into **b**, focusing on the vicinity of the comb lines. The spectral dependence of the locking range can be observed (cf. panel **a** and see main text for details). **d**, Locking range as a function of the relative mode number μ' . The measured data closely follows the predicted scaling (cf. main text). The grey area indicates the uncertainty we expect from 10% detuning fluctuations during the recording procedure. **e**, Locking range in terms of the repetition rate f_{rep} for $\mu' = -13$ as a function of secondary pump power (estimated on-chip power). Analogous to **d**, the uncertainty is approx. $\pm 4\%$.

Figure 3.3a shows an example of the recorded transmission signal where the scanning laser's frequency ω' is in the vicinity of the comb line with index $\mu' = -3$. When the laser frequency ω' is sufficiently close to the DKS comb line, the heterodyne oscillations (blue trace) can be sampled; when ω' is within the locking range δ_{lock} , the heterodyne oscillations vanish, and a linear slope is visible, indicating the changing phase between the comb line and the secondary laser across the injection locking range. In addition to the heterodyne signal between the comb line and laser, a characteristic resonance feature, the so-called *C*-resonance [212, 213], representing (approximately) the resonance frequency ω_μ is observed.

The set of equivalent traces for all comb lines μ' in the range of the secondary (scanning) laser is presented in Figure 3.3b as a horizontal stack. For plotting these segments on a joint vertical axis, $\omega_p + \mu'D_1$ has been subtracted from ω' . In this representation, the parabolic curve (blue line in Figure 3.3b) connecting the *C*-resonances signifies the anomalous dispersion of the resonator modes ω_μ . In contrast, the equidistant comb lines form a straight feature (grey highlight), of which a magnified view is presented in Figure 3.3c. Due to the Raman self-frequency shift, the free-running repetition rate of the DKS comb f_{rep}^0 is smaller than the cavity's FSR $D_1/(2\pi)$, resulting in the negative tilt of the line. Here, to obtain a horizontal arrangement of the features, $\omega_p + \mu'2\pi f_{\text{rep}}^0$ has been subtracted from ω' . The locking range δ_{lock} corresponds to the vertical extent of the characteristic locking feature in Figure 3.3c. Its value is plotted as a function of the mode number in Figure 3.3d, revealing a strong mode number dependence of the locking range with local maxima (almost) symmetrically on either side of the central mode. The asymmetry in the locking range with respect to $\mu' = 0$ (with a larger locking range observed for negative values of μ') coincides with the Raman self-frequency shift of the soliton spectrum (higher spectral intensity for negative μ). Next, we keep μ' fixed and measure the dependence of δ_{lock} on the power of the injecting laser P' . As shown in Figure 3.3e, we observe an almost perfect square-root scaling $\delta_{\text{lock}} \propto \sqrt{P'}$, revealing the proportionality of the locking range to the strength of the injected field.

The observed scaling of the locking range may be understood in both the time and frequency domain. In the time domain, the beating between the two driving lasers creates a modulated background field inside the resonator, forming an optical lattice trap for DKS pulses [186, 192]. Here, to derive the injection locking range δ_{lock} , we extend the approach proposed by Taheri et al. [190], which is based on the momentum $p = \sum_\mu \mu |a_\mu|^2 = \bar{\mu} \sum_\mu |a_\mu|^2$ of the waveform (in a co-moving frame), where a_μ is the complex field amplitude in the mode with index μ , normalized such that $|a_\mu|^2$ scales with the photon number and $\bar{\mu}$ the *photonic center of mass* in mode number/photon

momentum space. As we show in the [Supplementary information](#), Section 3.4.3, the secondary driving laser modifies the waveform's momentum, thereby its propagation speed and repetition rate. For the locking range of the secondary laser, we find

$$\delta_{\text{lock}} = \frac{2}{\pi} \mu'^2 \eta D_2 \frac{\sqrt{P' P_{\mu'}}}{\sum_{\mu} P_{\mu}} \frac{\omega_p}{\omega_{\mu'}}, \quad (3.1)$$

and for the repetition rate tuning range

$$\delta f_{\text{rep}} = \delta_{\text{lock}} / |\mu'|, \quad (3.2)$$

where η is the coupling ratio, and the P_{μ} refer to the spectral power levels of the comb lines with index μ measured outside the resonator. The spectral shift of the spectrum in units of mode number μ is $2\pi\delta f_{\text{rep}}/D_2$. In the [Supplementary information](#), Section 3.4.1, we recast eq. 3.2 in terms of the injection ratio $\text{IR} = P'/P_{\mu'}$ to enable comparison with CW laser injection locking [214]. The results in Eqs. 3.2 and 3.1 may also be obtained in a frequency domain picture (see [Supplementary information](#), Section 3.4.3), realizing that the waveform's momentum is invariant under Kerr-nonlinear interaction (neglecting the Raman effect) and hence entirely defined by the driving lasers and the rate with which they inject photons of specific momentum into the cavity (balancing the cavity loss). If only the main pump laser is present, then $\bar{\mu} = 0$. However, in an injection-locked state, depending on phase, the secondary pump laser can coherently inject (extract) photons from the resonator, shifting $\bar{\mu}$ towards (away from) μ' . This is equivalent to a spectral translation of the intracavity field, consistent with the experimental evidence in Figure 3.2c.

To verify the validity of eq. 3.1 and 3.2, we perform numeric simulation based on the Lugiato-Lefever Equation (see Section 3.4.4 of the [Supplementary information](#)). We find excellent agreement between the analytic model and the simulated locking range. We note that eq. 3.1 and 3.2 are derived in the limit of low injection power, which we assume is the most relevant case. For large injection power, the spectrum may shift substantially and consequently affect the values of P_{μ} . Interestingly, while this effect leads to an asymmetric locking range, the extent of the locking range is only weakly affected as long as the spectrum can locally be approximated by a linear function across a spectral width comparable to the shift. Injection into a sharp spectral feature (dispersive wave) is studied by Moille et al. [81]

The values of P_{μ} do not generally follow a simple analytic expression and can be influenced by the Raman effect and higher-order dispersion. While our derivation accounts

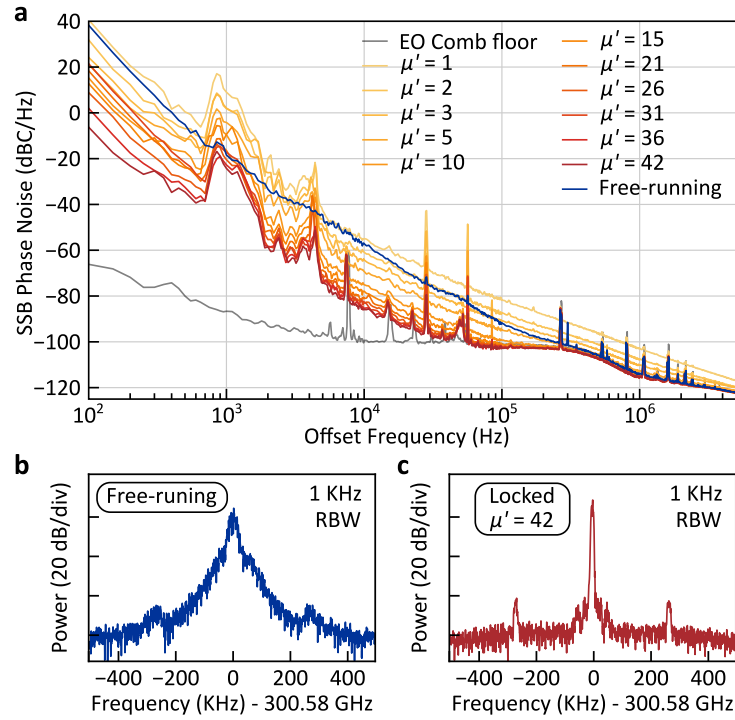


Figure 3.4 | Optical frequency division. **a**, Repetition rate phase noise of the soliton microcomb in the free-running and locked states, with values of μ' ranging from 1 to 42. At higher offset frequencies (>100 kHz), the phase noise of the electro-optic modulation used to down-mix the 300 GHz repetition rate signal to detectable frequencies (see [Supplementary information](#)) limits the measurement. **b**, Repetition rate beat note recorded in the free-running state. **c**, Repetition rate beatnote recorded in the locked state ($\mu' = 42$). The sidebands at approx. ± 300 kHz are an artifact of the electro-optic modulation-based repetition rate detection scheme.

for the values of P_μ (e.g., for the Raman effect a_μ and P_μ are increased (reduced) for μ below (above) $\mu = 0$), it does not include a physical description for Raman- or higher-order dispersion effects; these effects may further modify the locking range.

Taking into account the spectral envelope of the DKS pulse as well as the power of the injecting laser (which is not perfectly constant over its scan bandwidth), we fit the scaling $\delta_{\text{lock}} \propto \mu'^2 \sqrt{P' P_{\mu'}}$ to the measured locking range in Figure 3.3d, where we assume $P_{\mu'}$ to follow an offset (Raman-shifted) sech^2 -function. The fit and the measured data are in excellent agreement, supporting our analysis and suggesting that the Raman shift does not significantly change the scaling behavior. Note that the effect of the last factor in eq. 3.1 is marginal, and the asymmetry in the locking range is due to the impact of the Raman effect on P_μ . It is worth emphasizing that our analysis did not assume the intracavity waveform to be a DKS state and we expect that the analytic ap-

proach can in principle also be applied to other stable waveforms, including those in normal dispersion combs [194, 215]. Indeed, as we show numerically in Section 3.4.4 of the [Supplementary information](#), sideband-injection locking is also possible for normal dispersion combs. Here, in contrast to a DKS, sideband laser injection is found to have a strong impact on the spectral shape (not only spectral shift). Therefore, although the underlying mechanism is the same as in DKS combs, eq. 3.1 and eq. 3.2 do not generally apply (in the derivation, it is assumed that the spectrum does not change substantially).

Finally, as an example application of sideband injection locking, we demonstrate optical frequency division, similar to previous work [81], and measure the noise reduction in f_{rep} (Figure 3.4a). With a growing separation between the two driving lasers (increasing μ'), the phase noise is lowered by a factor of μ'^2 , resulting in a phase noise reduction of more than 3 orders of magnitude (with respect to the free-running case) when injecting the secondary laser into the mode with index $\mu' = 42$ (limited by the tuning range of the secondary laser), and this without any form of stabilization of either the pump or secondary laser. Figure 3.4b and c compare the repetition rate beatnote of the free-running and injection-locked cases.

3.3 Conclusion

In conclusion, we have presented an experimental and analytic study of sideband injection locking in DKS microcombs. The presented results reveal the dependence of the locking range on the intracavity spectrum and on the injecting secondary laser, with an excellent agreement between experiment and theory. While our experiments focus on the important class of DKS states, we emphasize that the theoretical framework from which we derive the presented scaling laws is not restricted to DKSs and may potentially be transferred to other stable waveforms. Our results provide a solid basis for the design of sideband injection-locked, parametrically generated Kerr-frequency combs and may, in the future, enable new approaches to low-noise microwave generation, compact optical clocks with simplified locking schemes, and more generally, stabilized low-noise frequency comb sources from Kerr-nonlinear resonators.

3.4 Supplementary information

3.4.1 Locking range equation in terms of the injection ratio

Eqs. 1 and 2 of the main text can be recast in terms of the injection ratio $IR = P'/P_{\mu'}$ and read:

$$\delta_{\text{lock}} = \frac{2}{\pi} \mu'^2 \eta D_2 \frac{P_{\mu'}}{\sum_{\mu} P_{\mu}} \frac{\omega_p}{\omega_{\mu'}} \sqrt{IR} \propto \sqrt{IR} \quad (3.3)$$

$$\delta f_{\text{rep}} = \frac{2}{\pi} |\mu'| \eta D_2 \frac{P_{\mu'}}{\sum_{\mu} P_{\mu}} \frac{\omega_p}{\omega_{\mu'}} \sqrt{IR} \propto \sqrt{IR} \quad (3.4)$$

3.4.2 Measuring the comb's repetition rate

The soliton comb's repetition rate, too high for direct detection, is measured by splitting off a fraction of the pump light and phase-modulating it with frequency $f_m = 17.68$ GHz, creating an electro-optic (EO) comb spanning ~ 600 GHz which is then combined with the DKS light (Figure 3.5). A bandpass filter extracts the 17th line of the EO comb and the first sideband of the DKS comb, resulting in a beatnote at a frequency $f_s = f_{\text{rep}} - 17 f_m$ from which the soliton repetition rate f_{rep} can be recovered, similar to [216].

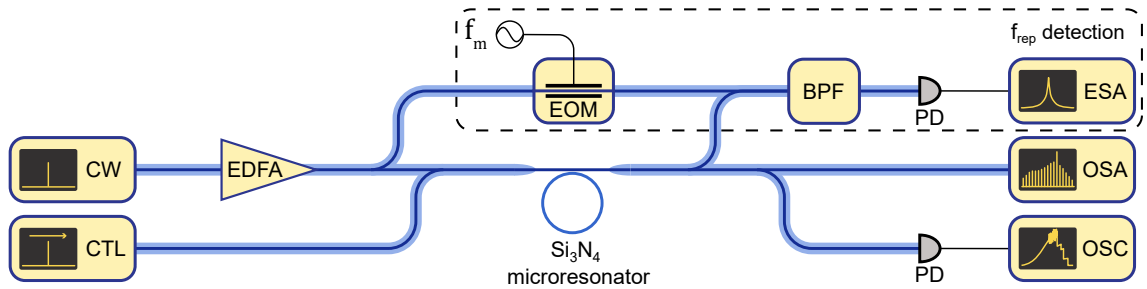


Figure 3.5 | Experimental setup. A single-DKS state is generated inside a silicon nitride microring resonator using approximately 200 mW of pump power. A secondary continuously tunable laser is combined with the pump light before the cavity in order to investigate the sideband injection locking dynamics. In order to monitor the ~ 300 GHz DKS repetition rate, we use a hybrid electro-optic detection scheme, similar to [216]. EDFA: erbium-doped fiber amplifier; CW: continuous wave laser; CTL: continuously tunable laser; PD: photodetector; OSC: oscilloscope; ESA: electrical spectrum analyzer; OSA: optical spectrum analyzer; EOM: electro-optic modulator; BPF: band-pass filter.

3.4.3 Analytic description of sideband injection locking

Definitions

We start from the dimensionless form of the Lugiato-Lefever equation (LLE) [83, 88], describing the dynamics in a frame moving with the (angular) velocity d_1 (the angular interval $[0, 2\pi]$ corresponds to one resonator round-trip):

$$\frac{\partial \Psi}{\partial \tau} = -(1 + i\zeta_0)\Psi + i|\Psi|^2\Psi + i \sum_{n=2}^{N \geq 2} (-i)^n \frac{d_n}{n!} \frac{\partial^n \Psi}{\partial \theta^n} + f, \quad (3.5)$$

where θ is the azimuthal coordinate, $\tau = \kappa t/2$ denotes the normalized time (κ being the cavity decay rate/total linewidth), $\Psi(\theta, \tau)$ is the waveform, $\zeta_0 = 2(\omega_0 - \omega_p)/\kappa$ the normalized pump detuning, $d_n = 2D_n/\kappa$ the normalized dispersion coefficients and $f = s\sqrt{8\eta g/\kappa^2}$ a pump field where $|s|^2 = \frac{P_p}{\hbar\omega_p}$ is the pump photon flux. The microresonator's coupling rate to the bus waveguide is κ_{ext} and $\eta = \kappa_{\text{ext}}/\kappa$ is the microresonator's coupling coefficient. Let $a_\mu(\tau)$ be the normalized complex mode amplitudes such that:

$$\Psi(\theta, \tau) = \sum_{\mu} a_\mu(\tau) e^{i\mu\theta}, \quad (3.6)$$

$$a_\mu(\tau) = \frac{1}{2\pi} \int_0^{2\pi} \Psi(\theta, \tau) e^{-i\mu\theta} d\theta, \quad (3.7)$$

where μ is the relative mode number and a_μ is related to the circulating intracavity power P_μ via $|a_\mu|^2 = \frac{2g}{\kappa} \frac{P_\mu}{\hbar\omega_\mu} \frac{2\pi}{D_1}$. Here $g = \hbar\omega_0^2 c n_2 / (n_0^2 V_{\text{eff}})$ is the nonlinear coupling coefficient, where c is the speed of light, n_0 the refractive index, n_2 the nonlinear index, and V_{eff} the mode volume.

The momentum p of the intra-cavity field $\Psi(\theta, \tau)$ is defined as:

$$p := \frac{1}{2} \frac{1}{2\pi} \int_0^{2\pi} \left[\Psi^* \left(i \frac{\partial \Psi}{\partial \theta} \right) + c.c. \right] d\theta \quad (3.8)$$

$$= \sum_{\mu} \mu |a_\mu|^2 \quad (3.9)$$

$$= \bar{\mu} \sum_{\mu} |a_\mu|^2 = \bar{\mu} N \quad (3.10)$$

where we used eq. 3.6, $\bar{\mu}$ denotes the *photonic center of mass* and $N = \sum_{\mu} |a_\mu|^2$ scales with the number of photons in the cavity.

Waveform velocity, spectral shift and repetition rate

We assume a waveform Ψ with a stable non-flat temporal intensity profile inside the resonator, i.e. the shape of the intensity profile does not change. The Waveform Ψ may not be static (in the frame moving with angular velocity d_1), but move with an additional angular velocity component $\dot{\theta}$, so that

$$|\Psi(\theta, 0)|^2 = |\Psi(\theta + \dot{\theta}\tau, \tau)|^2. \quad (3.11)$$

In a new coordinate frame ($\theta' = \theta - \dot{\theta}\tau$, $\tau' = \tau$, $\Psi'(\theta', \tau') = \Psi(\theta, \tau)$) that is co-moving with the intensity envelope, $|\Psi'|^2$ will be static so that $\partial|\Psi'|^2/\partial\tau' = 0$. For the derivatives we find

$$\frac{\partial\Psi'}{\partial\theta'} = \frac{\partial\Psi}{\partial\theta} \frac{\partial\theta}{\partial\theta'} + \frac{\partial\Psi}{\partial\tau} \frac{\partial\tau}{\partial\theta'} = \frac{\partial\Psi}{\partial\theta} \quad (3.12)$$

and

$$\frac{\partial\Psi'}{\partial\tau'} = \frac{\partial\Psi}{\partial\theta} \frac{\partial\theta}{\partial\tau'} + \frac{\partial\Psi}{\partial\tau} \frac{\partial\tau}{\partial\tau'} = \dot{\theta} \frac{\partial\Psi}{\partial\theta} + \frac{\partial\Psi}{\partial\tau} \quad (3.13)$$

so that

$$\begin{aligned} 0 = \frac{\partial|\Psi'|^2}{\partial\tau'} &= \frac{\partial\Psi'}{\partial\tau'} \Psi'^{*} + \Psi' \frac{\partial\Psi'^{*}}{\partial\tau'} \\ &= \frac{\partial\Psi}{\partial\tau} \Psi^* + \dot{\theta} \frac{\partial\Psi}{\partial\theta} \Psi^* + \Psi \frac{\partial\Psi^*}{\partial\tau} + \dot{\theta} \Psi \frac{\partial\Psi^*}{\partial\theta} \\ &= \left(\frac{\partial\Psi}{\partial\tau} \Psi^* + \Psi \frac{\partial\Psi^*}{\partial\tau} \right) + \dot{\theta} \left(\frac{\partial\Psi}{\partial\theta} \Psi^* + \Psi \frac{\partial\Psi^*}{\partial\theta} \right) \\ &= \left(\frac{\partial\Psi}{\partial\tau} \Psi^* + \Psi \frac{\partial\Psi^*}{\partial\tau} \right) + \dot{\theta} \frac{\partial|\Psi|^2}{\partial\theta}. \end{aligned} \quad (3.14)$$

By replacing the time derivatives with the right side of the LLE and only accounting for second-order dispersion ($d_n = 0, \forall n \geq 3$), one finds

$$\begin{aligned} \frac{\partial\Psi}{\partial\tau} \Psi^* + \Psi \frac{\partial\Psi^*}{\partial\tau} &= -2|\Psi|^2 + f\Psi^* + \\ & f^*\Psi + \frac{id_2}{2} \left(\Psi \frac{\partial^2\Psi^*}{\partial\theta^2} - \Psi^* \frac{\partial^2\Psi}{\partial\theta^2} \right). \end{aligned} \quad (3.15)$$

Under the assumption that the pump and loss term cancel in eq. 3.15, eq. 3.14 becomes

$$\begin{aligned} 0 &= \frac{id_2}{2} \left(\Psi \frac{\partial^2\Psi^*}{\partial\theta^2} - \Psi^* \frac{\partial^2\Psi}{\partial\theta^2} \right) + \dot{\theta} \frac{\partial|\Psi|^2}{\partial\theta} \\ &= \frac{id_2}{2} \frac{\partial}{\partial\theta} \left(\Psi \frac{\partial\Psi^*}{\partial\theta} - \Psi^* \frac{\partial\Psi}{\partial\theta} \right) + \dot{\theta} \frac{\partial|\Psi|^2}{\partial\theta}. \end{aligned} \quad (3.16)$$

Considering the indefinite integral $\int d\theta$ results in

$$\frac{id_2}{2} \left(\Psi \frac{\partial \Psi^*}{\partial \theta} - \Psi^* \frac{\partial \Psi}{\partial \theta} \right) + const = \dot{\theta} |\Psi|^2. \quad (3.17)$$

In the following, we take $const = 0$, which in case of a non-zero value corresponds to a suitable (re-)definition of the moving frame. Next, integrating according to $\frac{1}{2\pi} \int_0^{2\pi} d\theta$ and using Parseval's theorem $\sum_{\mu} |a_{\mu}|^2 = \frac{1}{2\pi} \int_0^{2\pi} |\Psi|^2 d\theta = N$ gives

$$\dot{\theta} = d_2 \frac{p}{N} = d_2 \bar{\mu} \quad (3.18)$$

The change in the repetition rate $\delta f_{\text{rep}} = \frac{\kappa}{2} \frac{\dot{\theta}}{(2\pi)}$, hence

$$\delta f_{\text{rep}} = \frac{D_2}{2\pi} \frac{p}{N} = \frac{D_2}{2\pi} \bar{\mu}, \quad (3.19)$$

the change of the repetition rate is proportional to the shift of the photonic center of gravity $\bar{\mu}$ away from $\mu = 0$.

Sideband injection locking: Time domain description

In the case of a pump laser at frequency ω_p and a secondary laser at frequency ω' close to $\omega_{\mu'}$, the pump field takes the form:

$$f \rightarrow f(\theta, \tau) = f_p + f' e^{i\mu'\theta} e^{-i2/\kappa(\omega' - \omega_p - \mu'D_1)\tau} \quad (3.20)$$

$$= f_p + f' e^{i\mu'\theta} e^{-i\tilde{\zeta}\tau} \quad (3.21)$$

where $\tilde{\zeta} = 2/\kappa(\omega' - \omega_p - \mu'D_1)$ is a term describing the mismatch between the microresonator FSR and the grid defined by the pump and secondary lasers.

From ref. [186], eq. 26, it follows that the force on the waveform Ψ due to the presence of the secondary pump line is:

$$\frac{dp}{d\tau} = -2p + \mu' \left[f' e^{-i\tilde{\zeta}\tau} \frac{1}{2\pi} \int_0^{2\pi} \Psi^* e^{i\mu'\theta} d\theta + \text{c.c.} \right] \quad (3.22)$$

We recognize that the integral term is the Fourier transform of the intracavity field, such that:

$$\frac{dp}{d\tau} = -2p + \mu' \left[f' e^{-i\tilde{\zeta}\tau} a_{\mu'}^* + \text{c.c.} \right] \quad (3.23)$$

$$= -2p + 2\mu' |f'| |a_{\mu'}| \cos(\tilde{\zeta}\tau + \angle a_{\mu'} - \angle f') \quad (3.24)$$

We assume that Ψ is a stable waveform, moving at an angular velocity $\dot{\theta}$ within the LLE reference frame, which itself moves with d_1 . In a suitable (θ', τ') -coordinate system, the waveform $\Psi'(\theta', \tau')$ is static (does not move), as described in Section 3.4.3. For the relation between the Fourier transforms of Ψ and Ψ' we find that $a_\mu = a'_\mu \exp(-i\mu\dot{\theta}\tau)$ and therefore $\angle a_{\mu'} = \angle a'_{\mu'} - \mu'\dot{\theta}\tau$. After substitution of the angle we find

$$\frac{dp}{d\tau} = -2p + 2\mu'|f'|\|a_{\mu'}\| \cos(\angle a'_{\mu'} - \angle f' + (\tilde{\zeta} - \mu'\dot{\theta})\tau) \quad (3.25)$$

We search for a steady state solution in which the momentum is constant $dp/d\tau = 0$. As, in a steady comb state $\frac{\partial a'_\mu}{\partial \tau} = 0$ (and f' does not depend on time), time independence is achieved when $\dot{\theta} = \tilde{\zeta}/\mu'$, i.e. the waveform must be moving at the velocity fixed by the pump and auxiliary laser detuning. Therefore, the momentum is purely a function of the relative phase between the secondary laser and the waveform's respective spectral component μ' :

$$p = \mu'|f'|\|a_{\mu'}\| \cos(\angle a'_{\mu'} - \angle f') \quad (3.26)$$

hence

$$\begin{aligned} p \in [-\mu'|f'|\|a_{\mu'}\|; \mu'|f'|\|a_{\mu'}\|] \\ \text{OR} \\ \bar{\mu} \in \left[-\mu' \frac{|f'|\|a_{\mu'}\|}{N}; \mu' \frac{|f'|\|a_{\mu'}\|}{N} \right] \end{aligned} \quad (3.27)$$

With eq. 3.19, this means that the repetition rate range in the injection-locked state is

$$\begin{aligned} \delta f_{\text{rep}} &= 2|\mu'| \frac{D_2 |f'|\|a_{\mu'}\|}{2\pi N} \\ &\approx 4|\mu'| D_2 \frac{\sqrt{\kappa_{\text{ext}}}}{\kappa} \frac{\sqrt{P' P_{\mu'}}}{\sum_{\mu} P_{\mu}} \frac{\omega_0}{\omega_{\mu'}} \\ &= 4|\mu'| \eta D_2 \frac{\sqrt{P' P_{\mu'}}}{\sum_{\mu} P_{\mu}} \frac{\omega_0}{\omega_{\mu'}} \end{aligned} \quad (3.28)$$

and the locking range is given by

$$\delta_{\text{lock}} = |\mu'| f_{\text{rep}} = 4\mu'^2 \eta D_2 \frac{\sqrt{P' P_{\mu'}}}{\sum_{\mu} P_{\mu}} \frac{\omega_0}{\omega_{\mu'}} \quad (3.29)$$

where the power levels P' and P_{μ} are the power levels measured outside the resonator.

The approximation in the second line of eq. 3.29 assumes that the mean frequency of the photons in the cavity is approximately ω_0 . Note that $P_{\mu'}$ and P_0 can readily be measured via a drop port; however, in a through-port configuration such as the one used in our experiment, it may be buried in residual pump light. For a smooth optical spectrum, their values may also be estimated based on neighboring comb lines for a smooth optical spectrum.

Sideband injection locking: Frequency domain description

In the sideband injection-locked state, the nonlinear dynamics in the resonator may be described by the following set of coupled mode equations:

$$\begin{aligned} \frac{\partial a'_\mu}{\partial \tau} = & - \left(1 + i \frac{2}{\kappa} (\omega_\mu - \omega_p - \mu \omega_R) \right) a'_\mu \\ & + i \sum_{\alpha, \beta} a'_\alpha a'_\beta a'^*_{\alpha+\beta-\mu} \\ & + \delta_{0\mu} f_p + \delta_{\mu'\mu} f' \end{aligned} \quad (3.30)$$

Here, the a'_μ represent the modes with the frequencies $\omega_p + \mu \omega_R = 2\pi f_{\text{rep}}$, where ω_R is the actual repetition rate of the comb that may be different from D_1 . Note that the a'_μ correspond to the a'_μ of Section 3.4.3. In a steady comb state $\frac{\partial a'_\mu}{\partial \tau} = 0$, so that a fixed phase relation between modes a'_μ and the external driving fields f and f' exists. We now consider only the field of the waveform, which we again denote with a'_μ for simplicity (Note that in a DKS, the separation of the DKS field at mode $\mu = 0$ from that of the background is formally possible owing to their approximate phase shift of $\pi/2$). The rate at which photons are added to the waveform by the driving lasers is

$$\begin{aligned} \left. \frac{\partial N_0}{\partial \tau} \right|_{f_p} &= a_0'^* \partial_t a'_0 + c.c. = a_0'^* f_p + c.c. \\ &= 2|a'_0| |f_p| \cos(\angle a'_0 - \angle f_p) \end{aligned} \quad (3.31)$$

for the main driving laser, and

$$\begin{aligned} \left. \frac{\partial N_{\mu'}}{\partial \tau} \right|_{f'} &= a_{\mu'}'^* \partial_t a'_{\mu'} + c.c. = a_{\mu'}'^* f' + c.c. \\ &= 2|a'_{\mu'}| |f'| \cos(\angle a'_{\mu'} - \angle f') \end{aligned} \quad (3.32)$$

for the secondary driving laser. Photons are added or subtracted from the respective mode depending on the relative differential phase angles $\angle a'_0 - \angle f_p$ and $\angle a'_{\mu'} - \angle f'$. While $\angle a'_0 - \angle f_p \approx 0$ for the main driving laser, $\angle a'_{\mu'} - \angle f'$ (for the secondary laser) can

take all values from 0 to π during sideband injection locking. In the steady state, the cavity losses are balanced by the lasers so that

$$N = \sum_{\mu} N_{\mu} = \left. \frac{\partial N_0}{\partial \tau} \right|_{f_p} + \left. \frac{\partial N_{\mu'}}{\partial \tau} \right|_{f'} \quad (3.33)$$

The photonic center of gravity of the photons injected into the cavity is

$$\bar{\mu} = \frac{0 \cdot \left. \frac{\partial N_0}{\partial \tau} \right|_{f_p} + \mu' \cdot \left. \frac{\partial N_{\mu'}}{\partial \tau} \right|_{f'}}{\left. \frac{\partial N_0}{\partial \tau} \right|_{f_p} + \left. \frac{\partial N_{\mu'}}{\partial \tau} \right|_{f'}} = \mu' \frac{|a_{\mu'}| |f'| \cos(\angle a'_0 - \angle f')}{\sum_{\mu} N_{\mu}} \quad (3.34)$$

For clarity, we note that $\bar{\mu}$ does not change when photons are transferred through Kerr-nonlinear parametric processes from one mode to another mode. This is a consequence of (angular) momentum and photon number conservation (implying total mode number conservation) in Kerr-nonlinear parametric processes. Hence the photonic center of gravity of the injected photons (by main and secondary pump) is the same as the photonic center of gravity for the entire spectrum of the waveform. For the injection-locked state we find

$$\bar{\mu} \in \left[-\mu' \frac{|a_{\mu'}| |f'|}{\sum_{\mu} N_{\mu}}; \mu' \frac{|a_{\mu'}| |f'|}{\sum_{\mu} N_{\mu}} \right] \quad (3.35)$$

so that with eq. 3.19 we obtain the same result as in the time domain description for δf_{rep} and δ_{lock} (eq. 3.28 and eq. 3.29).

3.4.4 Numeric simulation of the sideband injection locking range

To complement our experimental and theoretical results, we run numerical simulations based on the coupled mode equation framework [96, 191] (a frequency-domain implementation of the LLE). In order to observe the sideband injection locking dynamic, a single DKS is first initialized inside the cavity and numerically propagated. In the absence of a secondary laser, the soliton moves at the group velocity of the pump wavelength and appears fixed within the co-moving frame (Figure 3.6a). The secondary laser f' is then injected as per eq. 3.20, where $\tilde{\zeta}$ controls the detuning of the secondary laser with respect to the free-running comb line a_{μ} . For $0 < |\tilde{\zeta}| < \delta_{\text{lock}}/\kappa$ (i.e., within the locking range), we observe that soliton moves at a constant velocity with respect to the co-moving frame (Figure 3.6b). Beyond the locking range, the soliton is no longer phase-locked to the pump, which can readily be identified by tracking the

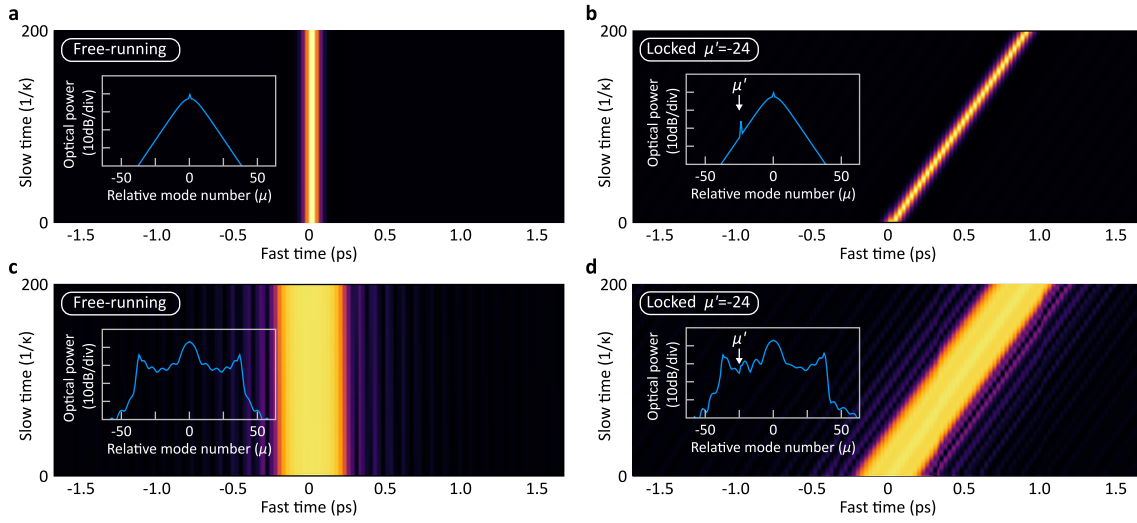


Figure 3.6 | Sideband injection locking simulation. Evolution of the intracavity intensity profile in the free running (**a**, **c**) and locked states (**b**, **d**) for both DKS (**a**, **b**) and normal-dispersion combs (**c**, **d**). Inset: corresponding intracavity spectra.

relative phase between $a_{\mu'}$ and f^l . We use this signature to identify the locking range from our simulations and compare it to our theoretical prediction from eq. 3.29; as can be seen in Figure 3.7, simulation and theory agree with striking fidelity.

We also study sideband injection locking dynamics inside normal-dispersion combs (Figure 3.6c and d). Here as well, we observe the locking of the *platicon* to the underlying modulation, although with a significant effect on its spectrum P_{μ} (see inset). This *platicon*'s spectrum lower robustness against external perturbation is not captured by our model which assumes a shifted but otherwise unchanged spectrum. Therefore, eq. 3.29 does not generally apply, even though we expect our model to predict the locking range within a tolerance corresponding to the relative amplitude change of the corresponding comb line $a_{\mu'}$.

3.4.5 Effect of thermal resonance shifts

Across the sideband-injection locking range, the power in the comb state changes by small amounts due to the secondary laser, which may add or subtract energy from the resonator (see Section 3.4.3). In consequence, the temperature of the resonator changes by small amounts, impacting via the thermo-refractive effect (and to a lesser extent by thermal expansion) the effective cavity length and hence f_{rep} . This effect occurs on top of the sideband injection locking dynamics. In a typical microresonator, the full thermal shift of the driven resonance that can be observed prior to soliton formation is within 1 to 10 GHz. In a DKS state, the coupled power is usually 1 to 10%,

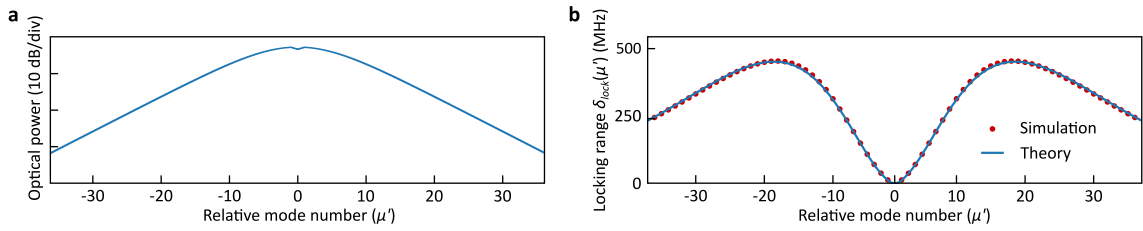


Figure 3.7 | Locking range simulations. **a**, Intracavity spectrum of the single DKS state used for the simulation of the sideband injection locking range. **b**, Simulated and theoretical (cf. eq. 3.29) locking range of the sideband-injection locking dynamic.

implying a maximal thermal shift of 1 GHz. Assuming the secondary laser will change the power in the resonator by not more than 5% (theoretical maximum for the highest pump power used in our manuscript), we expect a maximal thermal resonance shift of 50 MHz. Now, dividing by the absolute mode number of > 500 , we expect $\delta f_{\text{rep}} < 100 \text{ kHz}$, which is two orders of magnitude below the effect resulting from sideband injection locking.

Chapter 4

Phase-stabilised self-injection-locked microcomb

Thibault Wildi^{1, †}, Alexander E. Ulanov^{1, †}, Thibault Voumard¹, Bastian Ruhnke¹ and Tobias Herr^{1,2}

¹ *Deutsches Elektronen-Synchrotron DESY, Notkestr. 85, 22607 Hamburg, Germany*

² *Physics Department, Universität Hamburg UHH, Luruper Chaussee 149, 22761 Hamburg, Germany*

[†] *These authors contributed equally*

Published in *Nature Communications* Vol. 15, Article number 7030 on August 12, 2024

<https://doi.org/10.1038/s41467-024-50842-8>

Author contributions

T.W., A.U., and T.H. conceived the experiment. T.W. and A.U. designed the setup and the photonic chip, performed the experiments, and analyzed the data. T.V. developed and operated the reference comb. B.R. supported the design of the resonator and the experiments. T.H. supervised the work. T.W., A.U., and T.H. prepared the manuscript with input from all authors.

Abstract

Microresonator frequency combs (microcombs) hold great potential for precision metrology within a compact form factor, impacting a wide range of applications such as point-of-care diagnostics, environmental monitoring, time-keeping, navigation and astronomy. Through the principle of self-injection locking, electrically-driven chip-based microcombs with minimal complexity are now feasible. However, phase-stabilisation of such self-injection-locked microcombs — a prerequisite for metrological frequency combs — has not yet been attained. Here, we address this critical need by demonstrating full phase-stabilisation of a self-injection-locked microcomb. The microresonator is implemented in a silicon nitride photonic chip, and by controlling a pump laser diode and a microheater with low voltage signals (less than 1.5 V), we achieve independent control of the comb's offset and repetition rate frequencies. Both actuators reach a bandwidth of over 100 kHz, enabling phase-locking of the microcomb to external frequency references. These results establish photonic chip-based, self-injection-locked microcombs as low-complexity yet versatile sources for coherent precision metrology in emerging applications.

4.1 Introduction

Optical frequency combs provide large sets of laser lines that are equidistant in optical frequency and mutually phase-coherent [4, 181]. Owing to this property, they have enabled some of the most precise measurements in physics and are pivotal to a vast range of emerging applications, from molecular sensing to geonavigation. Frequency combs based on high-Q nonlinear optical microresonators (microcombs) [37, 44] that can be fabricated in complementary metal–oxide–semiconductor (CMOS) compatible, low-cost, scalable, wafer-scale processes [50, 54], promise to bring frequency comb technology into widespread application beyond the confines of optics laboratories [110, 139, 180].

In microcombs, nonlinear processes partially convert a continuous-wave (CW) driving laser with frequency ν_p into a series of comb lines that are mutually spaced in frequency by the comb's repetition rate f_{rep} , so that $\nu_\mu = \nu_p + \mu f_{\text{rep}}$, describes the frequencies ν_μ in the comb ($\mu = 0, \pm 1, \dots$ is a mode index relative to the pump; see Figure 4.1c). For many comb-based precision measurements, it is crucial to independently control the comb's defining parameters, here ν_p and f_{rep} , on a level that permits full phase control, i.e. *phase-locking*, of ν_p and f_{rep} to external frequency references. This is equiv-

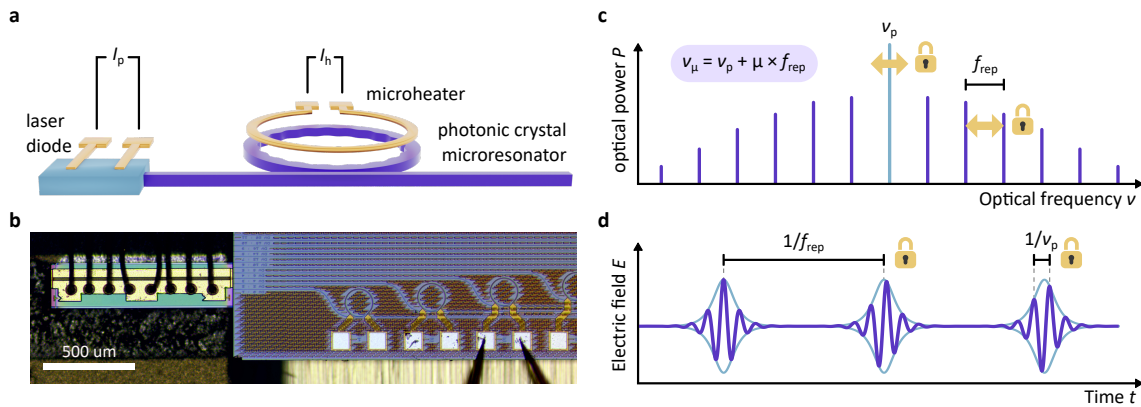


Figure 4.1 | Phase-stabilised self-injection-locked microcomb. **a**, Synthetic-reflection self-injection-locked microcomb. The combined actuation of the laser diode current I_p and the current I_h of a microheater controlling the microring temperature enables full phase-stabilisation of the microcomb via low voltage signals. **b**, Micrograph of the SIL microcomb source comprised of a DFB laser diode (left) butt-coupled to a photonic-chip hosting Si_3N_4 microresonators (right). A metallic microheater embedded in the SiO_2 cladding is routed above the microring. **c**, The optical spectrum of a continuous-wave driven microcomb is comprised of equidistant lines ν_μ spaced by the comb's repetition rate f_{rep} and centred on the pump frequency ν_p . Full phase-stabilisation of the microcomb entails locking both degrees of freedom to an external reference. **d**, In the time domain, this corresponds to a pulse train with a stabilised period $\tau_{\text{rep}} = 1/f_{\text{rep}}$ and optical carrier period $\tau_p = 1/\nu_p$.

alent to controlling carrier wave and envelope of the temporal optical waveform as indicated in Figure 4.1d. For instance, this is important for molecular spectroscopy, environmental monitoring, medical diagnostics, geonavigation, exoplanet search, and other emerging applications that rely on phase-coherent links between electromagnetic waves.

A major advancement in microcombs came through the principle of self-injection locking (SIL) [123, 124, 217], which enabled electrically-driven comb sources with drastically reduced operational complexity and chip-level integration [45, 119, 129–132, 134, 218]. Instead of a low-noise tabletop pump laser, SIL utilises a chip-scale semiconductor pump laser and a narrow linewidth injection feedback from a high-Q microresonator. The SIL mechanism leads to a low-noise pump laser and elegantly ensures that the laser is intrinsically tuned to the microresonator for comb generation. Although highly attractive, the simplicity and compactness of SIL-based combs entail a critical drawback with regard to controlling ν_p and f_{rep} . In contrast to previous non-SIL systems in which the frequency and the power of a tabletop pump laser have been used as independent actuators to simultaneously phase-stabilise ν_p and f_{rep} [219–221], in SIL

systems, these parameters are not independent (both depend on the laser pump current). Previous work has already accomplished stabilisation of one degree of freedom (f_{rep}) [76], however, phase-stabilisation of both degrees of freedom is an outstanding challenge. This lack of full phase-stabilisation in SIL microcombs represents a serious shortcoming for metrological applications.

Here, we present a chip-scale, electrically-driven, metrology-grade SIL microcomb operating at CMOS-compatible voltages. This source combines a semiconductor laser diode and a high-quality factor silicon nitride microresonator equipped with an integrated microheater [118, 171] in a compact millimetre-square footprint (see Figure 4.1a and b). The diode current and the integrated microheater provide two independent, low-voltage (<1.5 V) actuators reaching a remarkable >100 kHz effective actuation bandwidth. With these actuators, and in conjunction with synthetic reflection SIL [134], which supports a large range of laser detunings and lowers the actuation bandwidth requirement through laser linewidth narrowing, we demonstrate full phase stabilisation of the microcomb by phase-locking ν_p and f_{rep} to external frequency references, creating a small-footprint, low-complexity, low-cost and CMOS-compatible frequency comb for demanding metrological applications.

4.2 Setup

Our microcomb is based on CW laser-driven dissipative Kerr-solitons (DKS) [44, 110, 112] in a chip-integrated silicon nitride photonic crystal ring resonator (PhCR) [74, 80, 81, 134]. In this scheme, a semiconductor distributed feedback (DFB) laser diode is butt-coupled to the photonic chip hosting the PhCR (coupling losses of ~ 3.5 dB), delivering approximately 25 mW of on-chip optical pump power at 1557 nm; a cleaved ultra-high numerical aperture optical fibre (UHNA-7) is utilised for output coupling (coupling losses of ~ 1.7 dB). Both the laser chip and microresonator chip are temperature stabilised with a precision of ± 5 mK via standard electric heaters/coolers. The microresonator itself is characterised by a free-spectral range (FSR) of 300 GHz, anomalous group velocity dispersion, and a high quality factor $Q \approx 1.5 \times 10^6$ (see Methods). An integrated metallic microheater [118, 171] is embedded in the silica cladding above the resonator waveguide for fast thermal actuation of the microresonator. Complementary to piezo-electric or electro-optic actuators [222–225], which in an integrated setting can also reach high actuation bandwidth, microheaters are an attractive low-complexity alternative as they provide a robust, long-lifetime and low-voltage solution, that is readily compatible with silicon-based photonic chip technology.

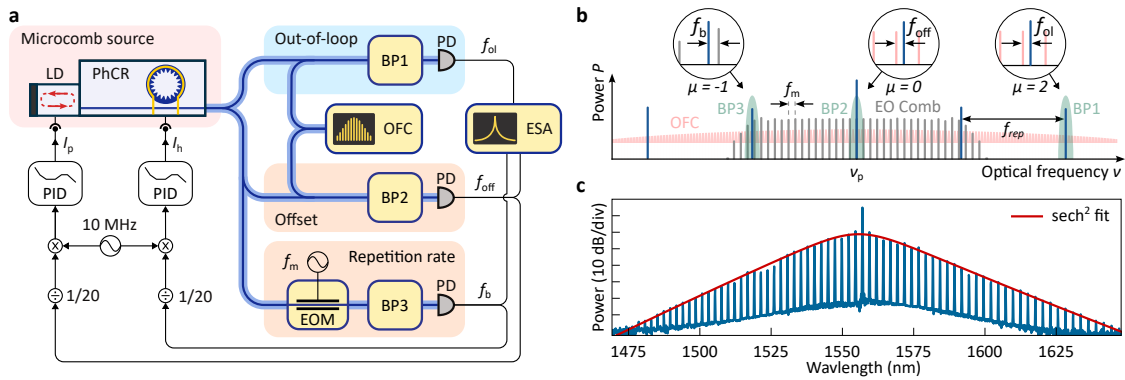


Figure 4.2 | Experimental setup. **a**, The microcomb source, a laser diode self-injection-locked to a photonic crystal ring resonator (PhCR) operating in the dissipative Kerr-soliton regime, is stabilised via two phase-lock loops feedback controlling the diode current I_p and heater current I_h respectively. OFC: reference optical frequency comb; ESA: electronic spectrum analyser; EOM: electro-optic modulator; BP: band-pass filter; PD: photodetector; LD: laser diode; PhCR: photonic crystal ring resonator; PID: proportional-integral-derivative controller. **b**, Frequency diagram, depicting the self-injection-locked microcomb (blue), the reference 1 GHz oscillator (red) and the electro-optic (EO) modulation comb (grey). The frequencies f_b , f_{off} , and f_{ol} , corresponding to the repetition rate, offset, and out-of-loop beat notes, respectively, are extracted by the optical band-pass filters BP1-3 (green) as shown in the insets. **c**, Optical spectrum of a self-injection-locked microcomb. The spectrum is well fitted by a sech^2 envelope with a FWHM of 1.44 THz.

By leveraging a recently demonstrated synthetic reflection technique [134], where the nano-patterned corrugation of the PhCR generates a tailored optical feedback, robust self-injection locking of the driving laser diode is achieved. This also has the desirable effect of forcing exclusive and deterministic single-soliton operation [74, 134]. Synthetic reflection also substantially extends the range of pump frequency-to-resonance detunings that are permissible during comb operation, providing extended actuation range and robust operation under phase-locking conditions. Moreover, the laser linewidth narrowing obtained via SIL relaxes the need for high bandwidth actuation.

In SIL DKS operation, the DFB laser's emission frequency ν_p (the central comb line of the microcomb) can be tuned by adjusting the current around the set point at a rate of 27 MHz mA^{-1} , which also affects the DKS repetition rate by 160 kHz mA^{-1} via the detuning-dependent Raman-induced soliton self-frequency shift (see [Supplementary information](#)). A second degree of freedom is provided by the microheater, which we operate at a current bias of 3 mA (105 mV). Via the microheater, the microcomb's repetition rate f_{rep} can be tuned with a sensitivity of $\sim 400 \text{ kHz mA}^{-1}$. As the laser diode and the microresonator are coupled through SIL, the microheater also induces a shift in

the microcomb's centre frequency ν_p (pump line) with a sensitivity of $\sim 160 \text{ MHz mA}^{-1}$. The actuator sensitivities are summarised in Table 4.1 and a theoretical derivation is provided in the [Supplementary information](#). As the corresponding control matrix is diagonalisable with non-zero diagonal elements, the two actuators enable independent control of both degrees of freedom of the SIL microcomb (ν_p and f_{rep}). As we show in the [Supplementary information](#), Section 4.6.3, the actuators are linear over a large actuation range (exceeding what is needed for phase-locking by orders of magnitude) and hence enable robust operation even under changing environmental conditions.

Depending on the application scenario, a frequency comb may be stabilised to different references, such as two lasers for frequency division and clock operation [226, 227], or a repetition rate and self-referencing signal [220, 228–232] to provide a phase-coherent radio-frequency-to-optical link. Figure 4.2a shows the experimental setup for proof-of-concept stabilisation and characterisation of the microcomb. Specifically, we validate the capability of our system to achieve full-phase stabilisation by comparing our microcomb against a conventional optical frequency comb (OFC). The 1 GHz repetition rate of the conventional OFC is phase-locked to a 10 MHz signal from a GPS disciplined Rb-clock [233]. As Figure 4.2b illustrates, an error signal for stabilisation of ν_p is generated by recording the offset beatnote f_{off} between the microcomb line ν_p and the closest line of the reference OFC [219, 228] (note that this offset is not to be confused with the carrier-envelope offset frequency). To obtain a repetition rate error signal, we utilise electro-optic phase-modulation (modulation frequency $f_m \approx 17.5 \text{ GHz}$) of the central comb line and detect the beating $f_b = f_{\text{rep}} - 17 \times f_m \approx 200 \text{ MHz}$ between 17th modulation sideband and the first sideband of the microcomb [216]. Both beat notes are then frequency-divided down to approximately 10 MHz, and the error signals are extracted through phase detection with respect to the 10 MHz Rb-clock signal (all microwave sources and recording devices are also referenced to the 10 MHz signal from the Rb-clock). The phase-locked loops (PLLs) are implemented using two con-

Sensitivity	f_{off}	f_{rep}
I_p	27 MHz/mA	160 kHz/mA
I_h	160 MHz/mA	400 kHz/mA

Table 4.1 | Actuator sensitivities. Sensitivity of the SIL microcomb's offset frequency f_{off} and repetition rate f_{rep} to the DFB current I_p and micro-heater current I_h . The values were measured around the experiment set point of $\sim 180 \text{ mA}$ and 3 mA , respectively. A theoretical derivation of the actuator tuning coefficients is presented in Section 4.6.1 and 4.6.2 of the [Supplementary information](#).

ventional off-the-shelf proportional-integral-derivative (PID) controllers, acting onto the laser diode's driving current I_p and the microheater current I_h for the offset f_{off} and repetition rate f_{rep} stabilisation, respectively. As follows from Table 4.1, alternative configurations of the PLLs are possible, e.g. swapping the actuators or simultaneously using both actuators for both degrees of freedom to diagonalise the control matrix, which would, however, involve specifically designed PID controllers (e.g., via a field-programmable gate array, FPGA).

Finally, an independent out-of-loop validation of the microcomb's phase-stability is performed by recording the beat note $f_{\text{ol}} = 2 \times f_{\text{rep}} + f_{\text{off}} - 601 \times 1 \text{ GHz}$ between the second sideband of the microcomb and the 601th sideband of the reference OFC. Impacted by both phase locks, the out-of-loop measurement is a key metric in evaluating the overall system performance.

4.3 Experiments

The successive initiation of both PLLs is shown in Figure 4.3a where the spectrogram of the out-of-loop beat note is presented. While activating the offset lock already substantially enhances the stability of the out-of-loop beat note (at $\sim 1.25 \text{ s}$ in Figure 4.3a), the remaining fluctuations are only suppressed with the additional activation of the repetition rate lock (at $\sim 2.8 \text{ s}$ in Figure 4.3a). Thus, the two high-bandwidth actuators and the extended detuning range, reliably obtained through synthetic reflection, enable phase stabilisation of the microcomb.

When the microcomb is phase stabilised, the phase excursion in the signals f_{rep} , and f_{off} are restricted to a limited interval by the PLLs. This restriction also implies that the phase excursion in the signal f_{ol} are bounded, as long as the reference OFC is phase-stabilised and differential variations of the in-loop and out-of-loop detection paths are negligible.

To get an insight into the nature of the phase excursions, we record the frequency evolution of the out-of-loop beat note f_{ol} with a gate time $\tau = 1 \text{ s}$ and without dead time between the non-overlapping samples (the frequency is extracted from the signal's quadratures, see Methods). The measured frequencies (shifted to zero-mean) are displayed in Figure 4.3b and the corresponding histogram is presented in Figure 4.3c (standard deviation of 4.25 Hz). The scatter of the frequency values (and hence the phase deviations) is well approximated by a Gaussian distribution, indicating random noise processes as their origin, as expected for a phase-locked state. Similar data can

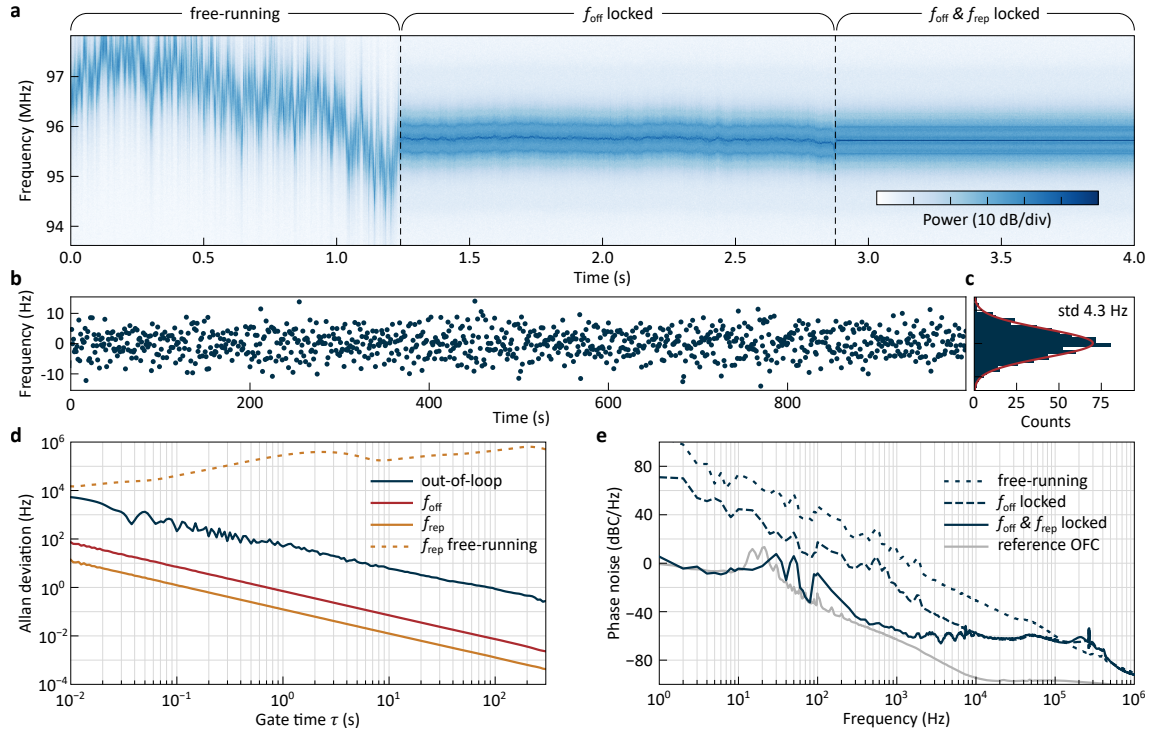


Figure 4.3 | Full phase-stabilisation of the self-injection-locked microcomb. **a**, Spectrogram of the out-of-loop beat note f_{ol} showing the transition from a free-running to a fully-locked state through the successive initiation of the offset f_{off} and repetition rate f_{rep} locks. **b**, Time series measurement of the out-of-loop frequency f_{ol} in the fully-locked state. The samples are acquired using a 1 s gate time at a rate of 1 Hz (zero dead time). **c**, Histogram of the values shown in **b**, with a Gaussian fit (in red) with 4.3 Hz standard deviation (std). **d**, Overlapping Allan deviations (OADs) under full-phase stabilisation of the out-of-loop signal (solid, blue), the in-loop offset frequency f_{off} (solid, red) and microcomb repetition rate f_{rep} (solid, orange) as a function of the gate time τ . The OADs average down with $\tau^{-0.996}$, $\tau^{-0.997}$ and $\tau^{-0.922}$ respectively. The OAD of the free-running f_{rep} is provided for comparison (dashed, orange). The frequency counter noise floor, 40 dB below the level of f_{rep} , is not shown. **e**, Single-sideband phase noise of the out-of-loop beat note f_{ol} in the free-running (orange), offset-locked (red) and fully-locked states (blue). The phase noise of the reference optical frequency comb is also shown (grey).

be obtained for f_{rep} and f_{off} but are not shown here.

Robust and tight phase-locking also manifests itself in the overlapping Allan deviations (OADs) of f_{rep} , f_{off} and f_{ol} , which we show in Figure 4.3d (see Methods). For sufficiently long averaging gate time τ , the OAD is expected to scale proportional to τ^{-1} as phase excursions are bounded by the PLLs. Indeed, the observed scalings of the OADs — $\tau^{-0.997}$, $\tau^{-0.996}$ and $\tau^{-0.922}$ for f_{rep} , f_{off} and f_{ol} respectively — follow the expectation for a phase lock. Importantly, the scalings of the OADs are clearly distinct from the $\tau^{-0.5}$ scaling characteristic of an unbounded random walk of the phase, which would result from random cycle slips in an imperfect phase lock. As such, the OADs of f_{rep} and f_{off} demonstrate the successful implementation of the phase locks, and the OAD of f_{ol} provides an independent out-of-loop validation. For comparison, we also show the OAD of the free-running f_{rep} signal, which, due to uncontrolled frequency drifts, results in an increasing OAD.

Complementing the Allan deviation measurement, we show in Figure 4.3e the phase noise of the out-of-loop beatnote f_{ol} to illustrate the impact of the phase lock. Consistent with Figure 4.3a, activating the f_{off} lock leads to a first reduction of the phase noise, and activation of both locks lowers the phase noise even more; the phase noise is limited at low frequencies by the phase noise of the reference OFC [233]. The crossing point of the free-running and fully-locked phase noise traces reveals a remarkably high locking bandwidth of larger than 100 kHz that is implemented via the diode current and the simple microheater.

To provide more insights into the locking actuators, we record the closed-loop frequency responses of the repetition rate and offset PLLs as shown in Figure 4.4a and **b** (with the respective other degree of freedom unlocked). Bandwidths of over 100 kHz and 300 kHz, respectively, are achieved for the microheater-based repetition rate actuator and the laser diode-based offset actuator. Both actuators allow for broadband noise suppression, as can be observed from the phase noise of the repetition rate f_{rep} and offset f_{off} signals (Figure 4.4c and **d**) and their corresponding beat notes (Figure 4.4e and **f**). We compute the residual phase modulation (PM) on f_{rep} and f_{off} in the fully-locked state (obtained by integrating the phase noise down to 1 Hz), yielding a root mean square (RMS) residual PM of 0.13 rad and 0.86 rad respectively. Considering the 20x prescaler in the PLLs, the residual PM values are at or below the milliradian level, confirming the tight phase lock. Despite the cross-talk between both actuators, no substantial degradation of the locking performance is observed when both degrees of freedom are locked simultaneously.

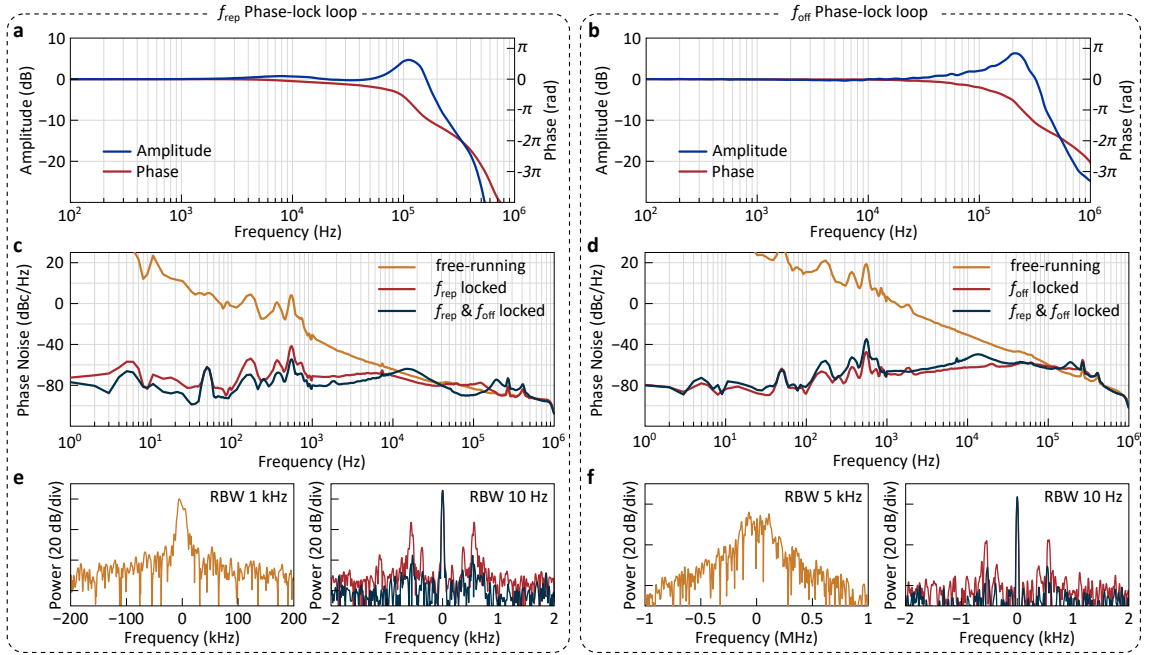


Figure 4.4 | Characterisation of the phase-locked loops. **a, b**, Closed-loop frequency response of the repetition rate f_{rep} (**a**) and offset beat note f_{off} (**b**) phase-locked loops. **c, d**, Single-sideband phase noise of f_{rep} (**a**) and f_{off} (**b**) in the free-running, partially locked and fully locked states. **e, f**, repetition rate beat notes (**e**) and offset beat notes (**f**) corresponding to the respective state shown in **c** and **d**. Note the difference in scale of the frequency axis between the free-running (left) and locked (right) states.

4.4 Conclusion

In conclusion, we demonstrate full phase-stabilisation of a self-injection-locked microresonator frequency comb, and validate its performance through comparison with a conventional mode-locked laser-based frequency comb. Based on a photonic-chip integrated microresonator, our system operates solely on CMOS-compatible driving and control voltages. The control actuators — comprising a laser diode and micro-heater — achieve a feedback bandwidth exceeding 100 kHz. In conjunction with synthetic reflection, our approach enables robust phase-locking of the microcomb to external frequency references in an unprecedentedly compact form factor.

Our microcomb source (Figure 4.1b) is implemented within a sub-1 mm² footprint and does not require the use of tabletop lasers, amplifiers, or high-voltage actuators. Future work could potentially leverage on-chip pulse amplification [234] and integrated f-2f interferometry [235–237] to achieve chip-scale self-referencing [220, 228–232], thereby implementing a phase-stable radio-frequency to optical link. Stabilising our system

to two atomic clock transitions would result in a compact optical clock, and the capability to achieve phase coherence between multiple sources can be instrumental for synchronisation of large scale facilities or communication networks.

As such, our demonstration establishes a novel, small-footprint, low-complexity, low-cost, and CMOS-compatible frequency comb source for demanding metrological applications, including those in portable, mobile, and integrated settings. The presented results may also inform the design of other chip-integrated light sources, such as rapidly tunable lasers or optical parametric oscillators.

4.5 Methods

4.5.1 Sample fabrication.

The samples were fabricated commercially by LIGENTEC SA using ultraviolet stepper optical lithography. The microresonator ring radius of $75\ \mu\text{m}$ corresponds to an FSR of 300 GHz, while a waveguide width of 1600 nm and a waveguide height of 800 nm provide anomalous group-velocity dispersion (difference between neighbouring FSRs at the pump frequency, $D_2/2\pi \approx 9\ \text{MHz}$). A coupling gap of 500 nm between the ring and bus waveguide ensures the resonator is critically coupled. Synthetic feedback to the driving DFB diode laser is provided by a nano-patterned corrugation, the amplitude and period of which were chosen to achieve a forward-backwards coupling rate $\gamma/2\pi \approx 145\ \text{MHz}$ at the pump wavelength of $\sim 1557\ \text{nm}$ [134]. All modes, including the pump mode, exhibit a high quality factor of $Q \approx 1.5 \times 10^6$.

4.5.2 Frequency stability measurements.

To measure the long-term stability of the microwave signals, we record the beat note's in-phase and quadrature (I/Q) components using the built-in I/Q-analyser of an electronic spectrum analyser (Rohde & Schwarz FSW26). The phase is then extracted from the I/Q data, from which the overlapping Allan deviation is computed using the *Allan-Tools* python module implementing the NIST standards [238]. Frequency counts are obtained by evaluating the finite differences of the extracted phase over the gate time. Spectrograms, spectra, and phase noises are calculated similarly from IQ data.

4.5.3 Frequency response measurement.

To record the closed-loop frequency response of each of the actuators (Figure 4.4a and b), a modulation tone is added to the error signal at the input of the PID controller while locked, effectively modulating the set-point. The amplitude and phase of the error signal are then recorded as a function of the modulation frequency using a vector network analyser.

4.6 Supplementary information

4.6.1 Tuning of the offset frequency f_{off}

Diode laser current

The tuning rate of the diode laser frequency used in our work is approximately 1 GHz mA^{-1} . As illustrated in Figure 4.5, self-injection locking (SIL) reduces this tuning rate by a factor $\sigma = \partial\xi/\partial\zeta$ due to the feedback from the microresonator. In our case, we estimate $\sigma \approx 40$ when operating in the SIL dissipative Kerr soliton (DKS) regime [132] (the exact value of σ depends on the detuning between diode laser and microresonator), and therefore

$$\frac{\partial f_{\text{off}}}{\partial I_p} \approx 25 \text{ MHz mA}^{-1}. \quad (4.1)$$

This estimate is in excellent agreement with the measured value of 27 MHz mA^{-1} (c.f. Table 1 in manuscript). Furthermore, we note that SIL reduces the diode laser's linewidth by a factor σ^2 , often known as the SIL stabilisation coefficient. This more than 1000-fold reduction in linewidth significantly reduced the bandwidth requirement for the actuators and is critical in enabling phase-locking via heater control.

Heater current

Similarly, varying the microheater current modifies the temperature of the microresonator and hence affects the diode laser's emission frequency through the SIL mechanism. In our system, we measure the heater tuning coefficient to be approximately 1 GHz mW^{-1} in our chips (thermally-induced frequency shift per unit of dissipated electrical power), which corresponds to

$$\frac{\partial f_{\text{off}}}{\partial I_h} \approx 210 \text{ MHz mA}^{-1} \quad (4.2)$$

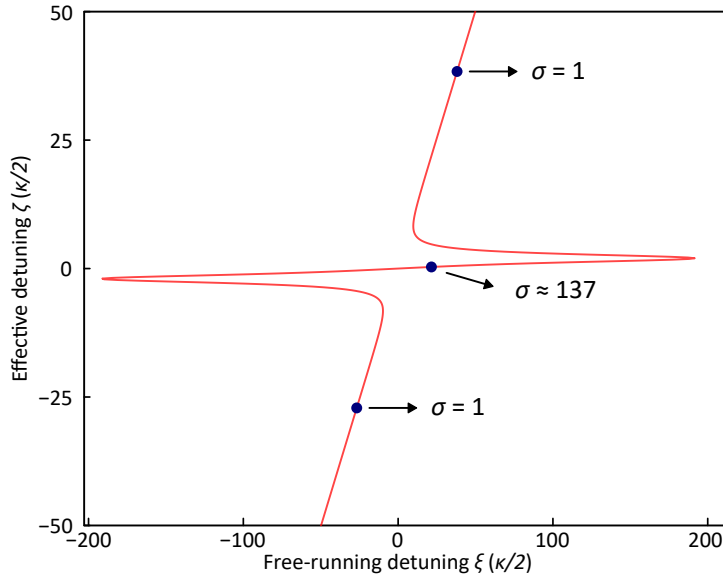


Figure 4.5 | Conceptual illustration of a SIL tuning curve. The effective detuning $\zeta = 2(\omega_0 - \omega_e)/\kappa$ is shown as a function of the laser-microresonator detuning $\xi = 2(\omega_0 - \omega_{LC})/\kappa$ (ω_0 is the resonance frequency of the microresonator, ω_e the laser emission frequency and ω_{LC} the free-running laser frequency, i.e. the laser's emission frequency in the absence of SIL). Outside of the SIL range, there is a one-to-one dependence between ζ and ξ , whereas, in SIL operation, the laser tuning speed $\partial\zeta/\partial\xi$ is reduced by a factor σ .

at our operation point (current bias of 3 mA). This is in good agreement with the measured value of 160 MHz mA^{-1} (c.f. Table 1 in manuscript).

4.6.2 Tuning of the repetition rate f_{rep}

To quantify the repetition rate tuning, we need to include the Raman-induced soliton self-frequency shift (SFS) in our considerations. The SFS is given by [208, 209]:

$$\Omega \approx -\frac{64\pi^2}{15} \frac{D_1^2}{2\pi D_2} \delta f_R \tau_R, \quad (4.3)$$

where D_1 and D_2 , describe the microresonator's mode frequencies $\omega_\mu = \omega_0 + D_1\mu + D_2/2\mu^2$ (μ is the relative mode index), $\delta = (\omega_0 - \omega_p)/(2\pi)$ the pump to resonance detuning, and f_R and τ_R the Raman fraction and shock terms respectively, taken to be 20% and 20 fs in silicon nitride [208]. The SRS translates directly to a change in the repetition rate via the cavity dispersion:

$$\Delta f_{\text{rep}} = \frac{\Omega}{2\pi} \frac{D_2}{D_1} \approx D_1 \delta f_R \tau_R. \quad (4.4)$$

Hence, the repetition rate is sensitive to the detuning δ via the Raman-induced SFS.

Diode laser current

As discussed in Section 4.6.1, the detuning δ can be tuned through the diode laser current at a rate of 25 MHz mA^{-1} . Using eq. 4.4, we find

$$\frac{\partial f_{\text{rep}}}{\partial I_p} \approx 190 \text{ kHz mA}^{-1}, \quad (4.5)$$

which is in good agreement with the measured value of 160 kHz mA^{-1} (c.f. Table 1 in manuscript).

Heater current

The detuning δ can also be adjusted via the heaters, although the tuning rate is reduced through the SIL mechanism by σ to approximately 5 MHz mA^{-1} . Again using eq. 4.4, we find

$$\frac{\partial f_{\text{rep}}}{\partial I_h} \approx 38 \text{ kHz mA}^{-1}. \quad (4.6)$$

On the other hand, thermal actuation directly affects the ring's FSR (via the thermorefractive effect and to a lesser extent, through thermal expansion) at a rate

$$\frac{1}{2\pi} \frac{\partial D_1}{\partial I_h} \approx 325 \text{ kHz mA}^{-1}. \quad (4.7)$$

These two different contributions add up to about $\partial f_{\text{rep}}/\partial I_h = 360 \text{ kHz mA}^{-1}$, which is again in good agreement with the measured value of 400 kHz mA^{-1} (c.f. Table 1 in the main manuscript).

4.6.3 Actuator linearity

The dependence of the microcomb repetition rate f_{rep} and offset frequency f_{off} where recorded as a function of the diode laser current I_p and heater current I_h (see Figure 4.6). All tuning curves are monotonic and, to good approximation, linear, which ensures stable locking conditions.

4.6.4 Microheater frequency response

We measure the open-loop microheater frequency response by using a slow side-of-fringe lock to stabilise a continuous wave laser on a resonance of the microresonator.

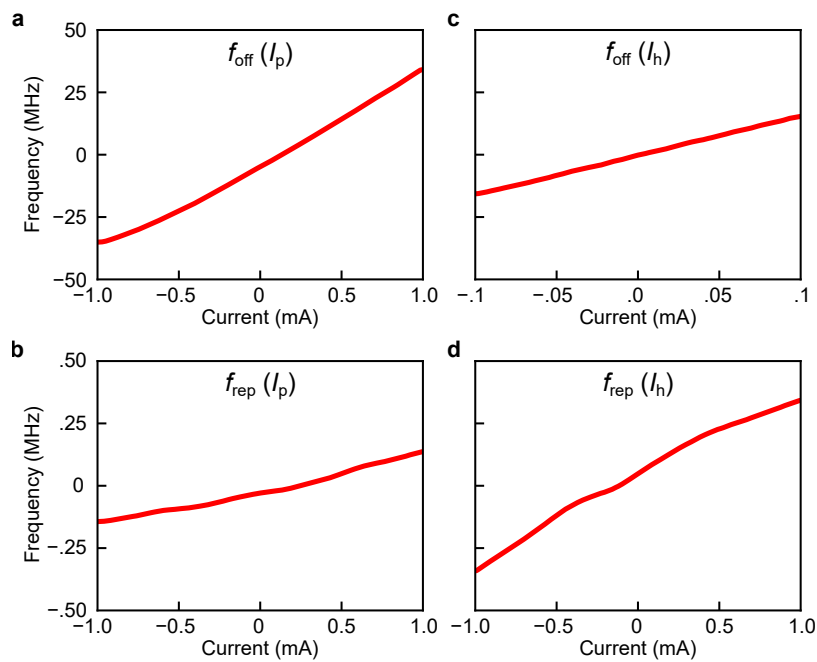


Figure 4.6 | Actuator tuning curves. Values are shown around the system’s operating point. **a**, Offset frequency f_{off} as a function of the diode laser current I_p . **b**, Repetition rate frequency f_{rep} as a function of the diode laser current I_p . **c**, Offset frequency f_{off} as a function of the microheater current I_h . **d**, Repetition rate frequency f_{rep} as a function of the microheater current I_h .

A sinusoidal tone is then applied to the microheater, which modulates the resonance frequency and, thereby, the transmission of the continuous wave laser. We can extract the microheater’s frequency response by recording the amplitude and phase relation between the input and output signal (see Figure 4.7).

As can be seen, the 3 dB of the microheater is approximately 5 kHz. Despite this, a phase delay of π is reached at ~ 100 kHz. This allows us, in a closed-loop configuration, to effectively extend the heaters’s bandwidth to more than 100 kHz. As the heater bandwidth dictates the overall system bandwidth, this step is critical in achieving both offset and repetition rate locks.

4.6.5 Comparison of fully phase-locked microcombs

A comparison of fully phase-locked microcombs to date (i.e. ν_p and f_{rep} are both phase-coherently stabilised to an external frequency reference) is provided in Table 4.2, where we list resonator platform, form factor, the employed actuators as well as important characteristics such as pump laser power, electrical power consumption, volume (excluding driving electronics) and approximate unit cost.

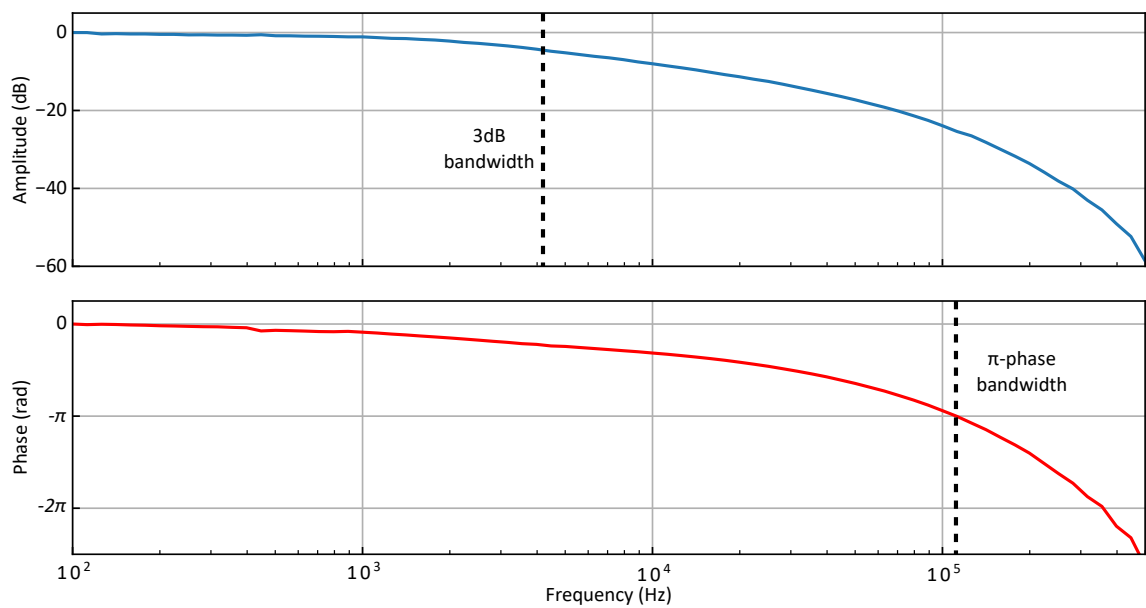


Figure 4.7 | Open-loop microheater frequency response. Amplitude (top) and phase (bottom) frequency response of the microheater. While the 3 dB bandwidth is approximately 5 kHz a phase delay of π is reached at ~ 100 kHz.

Ref.	Platform	Form factor w/ actuators	1 st actuator	2 nd actuator	Pump ^a (mW)	Elec. ^b (W)	Volume ^c (cm ³)	Cost ^d (USD)
[219]	SiO ₂ WGM	Table-top	ECDL detuning	EDEFA power	200	> 10	> 1000	> 10000
[229]	MgF ₂ WGM	Table-top	FL detuning	Aux. FL detuning	240	> 10	> 1000	> 10000
[220]	SiO ₂ WGM	Table-top	ECDL detuning	EDEFA power	100	> 10	> 1000	> 10000
[54]	Si ₃ N ₄ PIC	Table-top	ECDL detuning	AOM power	2000	> 10	> 1000	> 10000
[221]	Si ₃ N ₄ PIC	Table-top	SSB modulator	ECDL/EDEFA power	200	> 10	> 1000	> 10000
This work	Si ₃ N ₄ PIC	Chip-scale	SIL DFB current	Microheater	25	< 0.5	< 1	< 100

WGM, whispering-gallery-mode resonator; PIC, photonic integrated circuit microring resonator; ECDL, external cavity diode laser; EDEFA, erbium-doped fibre amplifier; FL, fibre laser; AOM, acousto-optic modulator; SSB single sideband; SIL, self-injection locking; DFB, distributed feedback laser diode. ^aCoupled optical pump power. ^bEstimated electrical power consumption of the optical frequency comb source. ^cEstimated volume excluding driving electronics. ^dEstimated unit cost, when fabricated at scale.

Table 4.2 | Comparison of fully phase-locked microresonator frequency combs.

Chapter 5

Summary and Outlook

Microresonator-based optical frequency combs have emerged as a promising complement to conventional optical frequency combs based on ultrafast lasers. With their small footprint, low power consumption, and high repetition rates, microcombs hold potential for a wide range of applications ranging from precision metrology and spectroscopy to telecommunications and optical clockwork. In this thesis, we have explored several approaches to addressing some of the critical challenges that still hinder the widespread adoption of microcombs by focusing on issues such as dispersion management, noise reduction, precise control, and phase-coherent metrological performance:

In Chapter 2, we presented the first demonstration of dissipative Kerr solitons inside an integrated Fabry-Pérot microresonator. Consisting of a pair of uniaxial photonic crystal reflectors (PCRs) embedded within a waveguide, the resonator's total dispersion is the sum of the mirrors and the waveguide contributions. Complementing methods developed for ring-type devices, Fabry-Pérot microresonators with dispersive mirrors provide a versatile approach to broadband dispersion engineering that may lead to DKSs at visible wavelengths and allow the use of new materials that are currently inaccessible due to unsuitable effective waveguide dispersion. This potential was highlighted in follow-up work by Nardi *et al.* [239], where chirped photonic crystal reflectors were used to achieve overall anomalous dispersion in an integrated Fabry-Pérot microresonator made from gallium phosphide — a promising material with a Kerr nonlinearity 200 times greater than that of the silicon nitride. The high refractive index of GaP enables a strong index modulation within the PCRs, resulting in a broadband cavity that supports ultra-short soliton pulses.

Since our publication, interest in Fabry-Pérot microresonators has continued to rise, as evidenced by numerous works on standing-wave Kerr cavities. These include investigations of dark solitons [240, 241] and pulsed-pumping [242] in the normal dispersion regime, modulation instability [243], symmetry breaking [244], the experimental demonstrations of broadband solitons in fiber cavities [245] and extensions to new material platforms [246, 247]. A recent review on microcombs in fiber Fabry-Pérot cavities [248] further underscores this growing interest. Furthermore, Fabry-Pérot microresonators have proven to be particularly well-suited to inverse design approaches [163, 249, 250], which utilize machine learning and large-scale electromagnetic simulations to optimize the topology of integrated photonic devices. When applied to photonic crystal reflectors, this approach yields intricate yet compact structures that cannot be designed through conventional means. Beyond standing-wave cavities, photonic crystal structures are increasingly employed for narrow and broadband dispersion engineering in nonlinear integrated photonics [80, 81, 251] and are now routinely included in the design of microresonators for soliton generation [122, 134, 137].

In Chapter 3, we presented a study of *sideband injection locking* in microresonator frequency combs, an all-optical approach to controlling a Kerr comb's offset and repetition rate frequencies relying on the injection of a second laser which forms part of the comb. Using this technique, an optical frequency division scheme was demonstrated, resulting in >30 dB noise suppression with respect to a free-running comb and highlighting its potential for applications such as low-noise microwave generation, compact optical clocks, and more generally, metrological-grade microcombs.

Despite sideband injection locking indirectly underpinning many aspects of Kerr frequency combs — including parametric seeding, dichromatic pumping, optical trapping, and soliton synchronization — it has been the subject of surprisingly little research to date [186, 190, 197, 205]. However, this is poised to change thanks to the increased visibility following the influential study by Moille *et al.* [232], published shortly after our work, which utilized this technique in the context of optical clockworks. Recent studies have already shown the use of *sideband injection locking* in low-noise Kerr combs [252], optical frequency division [253–255], Kerr comb-based voltage-controlled oscillators [256], and sub-comb mode locking [257].

In Chapter 4, following our investigation of a comb actuation method, we complement this by demonstrating chip-scale phase stabilization of a self-injection-locked microcomb. SIL relies on optical feedback from the microresonator to precisely control the emission frequency of the driving pump diode, thus eliminating the need for narrow-linewidth, rapidly tunable tabletop lasers. The significant reduction in ma-

terial and operational complexity of SIL-based microcombs holds great promise for bringing microresonator-based frequency combs from one-of-a-kind laboratory experiments to widespread applications. By demonstrating that SIL-based combs can be fully phase-stabilized to external frequency references, we further establish that such sources are compatible with metrological applications.

Looking ahead, the integration with additional chip-based technologies, such as on-chip amplification [234] and integrated f - $2f$ interferometry [235–237], could enable chip-scale self-referencing [220, 228–232]. Integrating a direct radio-frequency to optical link within such a small form factor might enable compact optical clocks and find application in communication, synchronization of large-scale facilities, or photonics analog-to-digital converters.

Appendix A

Frequency comb assisted diode laser spectroscopy

Diode lasers, relying on broadband semiconductor gain media, can be made into narrow-linewidth, tunable sources when paired with external cavity feedback mechanisms, such as those provided by diffraction gratings or etalons. Such external cavity diode lasers (ECDLs) — through the use of motor- and/or piezo-control and clever mechanical design — can achieve continuous, mode-hop-free tuning over broad bandwidth (>100 nm). They are sources of choice for spectroscopy with applications ranging from environmental monitoring [258] and medical diagnostics [259] to industrial process control [260] and fundamental research [261].

Frequency comb assisted diode laser spectroscopy (FCADLS) [211] relies on an auxiliary optical frequency comb to calibrate a frequency scan of a continuously tunable laser (CTL). It is a powerful technique that can provide broadband, high-resolution, and highly accurate spectroscopic data when a high acquisition rate is not required. In the current work, FCADLS has been extensively employed to characterize microresonators, facilitating measurements of dispersion, loss, and coupling that were crucial for the development of silicon nitride photonic integrated circuits. Additionally, FCADLS was used to calibrate the frequency of the injected laser and obtain broadband data in the microcomb side-band injection-locking experiments. A custom FCADLS setup was developed with a focus on spectral accuracy, robustness, and reliability, which enabled streamlined data acquisition and processing. The subsequent chapter explains the working principles of FCADLS and provides a comprehensive technical description of the experimental setup and methodologies.

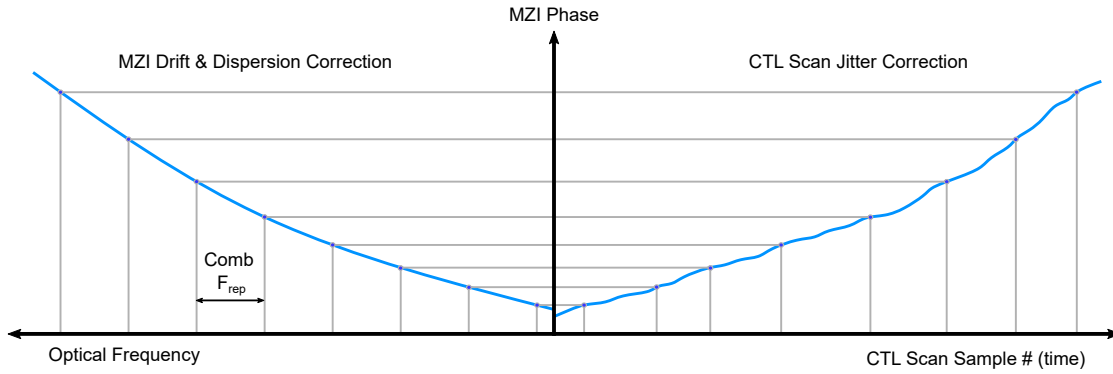


Figure A.1 | Working principle of MZI-assisted FCADLS. Calibration of the CTL frequency $\omega(t)$ is achieved by first mapping the scan time t onto the MZI phase φ , correcting fluctuation in the laser scan rate (see Section A.1). Evenly-spaced comb markers provided by the reference optical frequency comb enable conversion to optical frequency by providing a regular grid of known frequencies.

A.1 Working principles

In frequency comb assisted diode laser spectroscopy, the instantaneous frequency $\omega(t)$ of the scanning laser is reconstructed post-measurement by utilizing a calibration signal derived from a reference optical frequency comb (OFC). The calibration signal contains markers corresponding to the crossing events t_n between the scanning laser and the individual lines of the reference OFC. These markers establish an equidistant grid of known frequencies $\omega(t_n) = \omega_o + n \cdot \omega_{\text{rep}} = \omega_n$, where $\omega_o/(2\pi)$ and $\omega_{\text{rep}}/(2\pi)$ are the offset and repetition rate frequencies of the reference OFC¹. Assuming the scanning rate is approximately constant between two successive comb lines, that is, $\omega(t)$ is linear over the interval $t \in [t_n, t_{n+1}]$, the full frequency axis can be reconstructed via interpolation. In practice, this requirement is rarely met, and an additional calibration signal is required to bridge the gap between markers.

Expanding upon the original scheme proposed by Del’Haye *et al.* [211], our implementation incorporates two additional calibration channels. Firstly, a hydrogen cyanide (HCN) gas cell delivers absolute frequency calibration through a set of well-known spectral absorption features situated between 1525 nm and 1565 nm [262–264]. Secondly, an unbalanced all-fiber Mach–Zehnder interferometer (MZI) is employed to generate a frequency-dependent modulation signal, which enables precise interpolation between comb markers. The MZI transmission is proportional to $\sin \varphi(\omega)$, where the MZI phase $\varphi(\omega) = \Delta L \cdot \beta(\omega)$ depends on the length difference between the MZI

¹In practice, the absolute line number n is rarely known, and therefore, an additional mean of absolute frequency calibration is required.

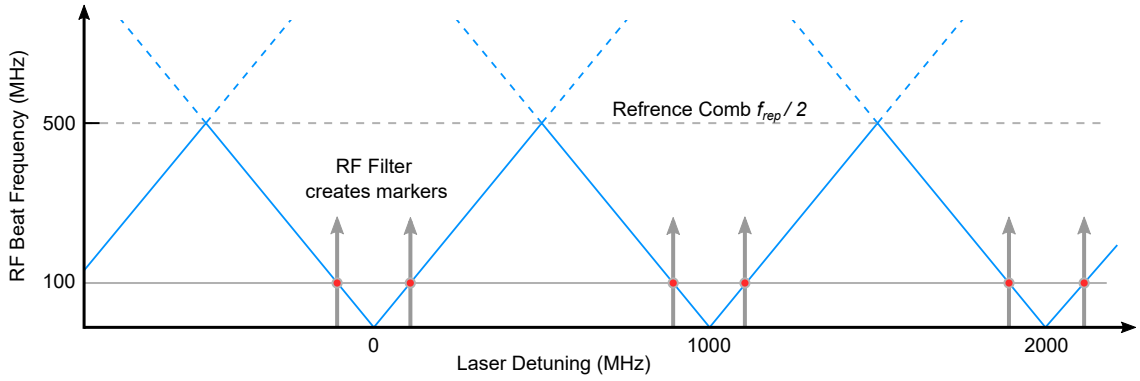


Figure A.2 | FCADLS calibration marker. The heterodyne beat frequency between the CTL and the nearest comb lines (blue) ramps back and forth between 0 Hz and $f_{\text{rep}}/2$. By introducing an RF band-pass filter, a pair of markers can be generated around each comb line when the beat note frequency is within the filter bandwidth.

arms ΔL and the dispersion of the fiber $\beta(\omega)$. Importantly, $\beta(\omega)$ is a *smooth* function of ω and, unlike the laser frequency $\omega(t)$, $\varphi(\omega)$ can be assumed to vary linearly between comb markers (in the interval $\omega \in [\omega_n, \omega_{n+1}]$).

This is illustrated in Figure A.1. In practice, the scan time t is first mapped onto the MZI phase φ by extracting the phase from the MZI signal². The MZI phase is then mapped onto frequency using the evenly spaced markers provided by the optical frequency comb. In the final step (not shown in Figure A.1), absolute frequency calibration is achieved using the HCN gas cell, effectively shifting the reconstructed frequency axis to the correct position.

A.1.1 Generation of comb markers

The calibration markers are generated by combining a portion of the light from CTL with that from the reference OFC. As illustrated in Figure A.2, this combination results in a series of heterodyne beat notes between the line of the CTL and the respective lines of the OFC. In practice, only the beat note between the CTL and the nearest comb line is considered (solid blue line in Figure A.2). By introducing a low-pass RF filter (or relying on the finite bandwidth of the photodiode used for detection), markers can be produced each time the CTL intersects a comb line, as a heterodyne signal is only present when the frequency difference between the CTL and the comb line is within the filter bandwidth. Alternatively, as shown in Figure A.2, a band-pass filter can be

²This is done by zeroing out negative frequency components of the MZI signal (i.e., taking $\varphi(t) + iH(\varphi(t))$ where $H(\cdot)$ is the Hilbert transform), turning the real-valued signal into a complex rotating phasor, the phase of which can be extracted.

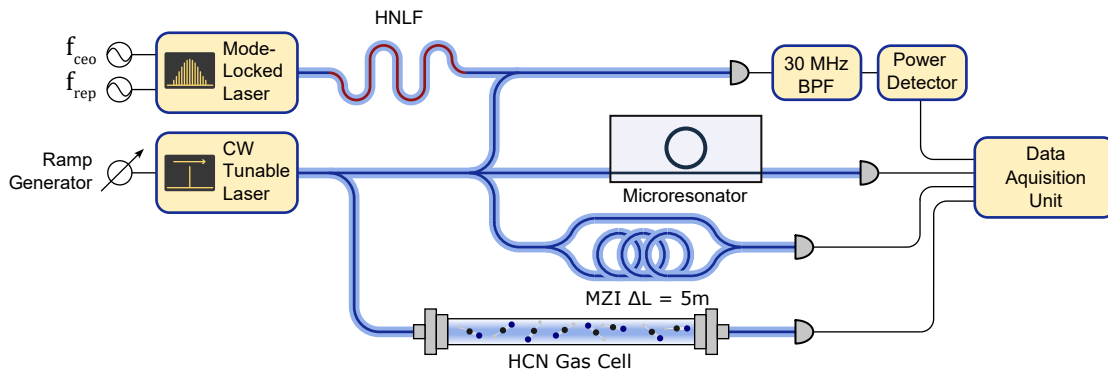


Figure A.3 | Frequency-assisted diode laser spectroscopy setup. CW: continuous wave; HNLf: Highly nonlinear fiber; BPF: bandpass filter; MZI: Mach-Zehnder interferometer.

used, resulting in two markers evenly spaced on either side of each comb line. This scheme is preferred as the heterodyne frequency does not pass through zero, simplifying signal processing. Optionally, an RF power detector can be added after the filter to extract the signal's envelope, reducing the required sampling rate as the heterodyne frequency does not need to be Nyquist-sampled.

A.2 Setup

Figure A.3 details the FCADLS setup used in the present work. Depending on the wavelength range of interest, a reference OFC with a repetition rate f_{rep} of either 1 GHz or 100 MHz is used. The 1 GHz OFC is generally preferred due to its higher power per line, resulting in a better signal-to-noise ratio of the calibration markers. However, when spectral extension through cascaded four-wave mixing is necessary to cover the desired wavelength range³, the 100 MHz OFC is favored due to its higher pulse peak power. Both combs can be self-referenced and fully stabilized for optimal performance [233]. The Mach-Zehnder interferometer is implemented in standard SMF28 optical fiber, using two 50/50 directional couplers and a length unbalanced $\Delta L = 5$ m, resulting in a free-spectral range of approximately 40 MHz. This allows for precise tracking of the MZI modulation signal and phase extraction with <1 MHz equivalent resolution. A 27 – 33 MHz bandpass filter and logarithmic RF power detector are used to generate the calibration markers from the heterodyne signal. The logarithmic power detector supports an input RF power from -60 dBm to 5 dBm, greatly extending the allowable dynamic range between the individual combs lines and effectively extending

³This is typically achieved using a length of polarization maintaining normal dispersion highly-nonlinear optical fiber.

Qty	Component	Description
1	HCN-13-H(5.5)-25-FCAPC	H ¹³ C ¹⁴ N fiber-coupled gas cell
2	Koheron PD100-DC	100 MHz low noise photodetector
1	Koheron PD100B-AC	100 MHz balanced photodetector
1	Koheron PD100B-DC	100 MHz balanced photodetector
1	ZX47-60LN-S+	Logarithmic RF power detector
1	SBP-30+	RF Bandpass filter
1	PMPLC-C+L-204-B-001-10-0.8-1	2x4 PM PLC splitters
2	50/50 SM Coupler	Direction coupler
1	50/50 PM Coupler	Direction coupler
1	5m SFM28	Single mode fiber

Table A.1 | Bill of material.

the scan range for a given reference comb spectrum.

A complete list of components, excluding laser sources and data acquisition devices, can be found in Table A.1.

A.3 Signal processing

Figure A.4 presents a typical set of traces acquired during an FCADLS scan. Panels a, b, and c show the full traces, comprising nearly 10^7 samples spanning from 1520 nm to 1605 nm (or approximately 10 THz of bandwidth), while panels d, e, and f show a magnified view of the signals spanning approximately 3.5 GHz. Panel e shows the magnified MZI calibration signal, with the modulation clearly resolved (~ 40 MHz FSR), while Panel f shows a magnified view of the comb (blue) and HCN gas cell (red) calibration signals. In the latter, the markers generated from the reference OFC appear in pairs, centered on each comb line, repeating every $f_{\text{rep}} = 1$ GHz, and separated by twice the RF band-pass filter frequency 2×30 MHz.

The calibration procedure is as follows:

1. The *analytical representation* of the MZI calibration signal is computed (negative frequency components are disregarded, resulting in a complex signal), from which the instantaneous phase $\varphi(t)$ is extracted.
2. The derivative of the phase signal $d\varphi(t)/dt$ is evaluated to get an estimation of the instantaneous laser scanning rate $d\omega(t)/dt \approx c/(n\Delta L) \cdot d\varphi(t)/dt$. This estimation is then used to identify the (central) portion of the scan where the laser speed remains approximately constant. All the traces are then re-cut, disregard-

Appendix A. Frequency comb assisted diode laser spectroscopy

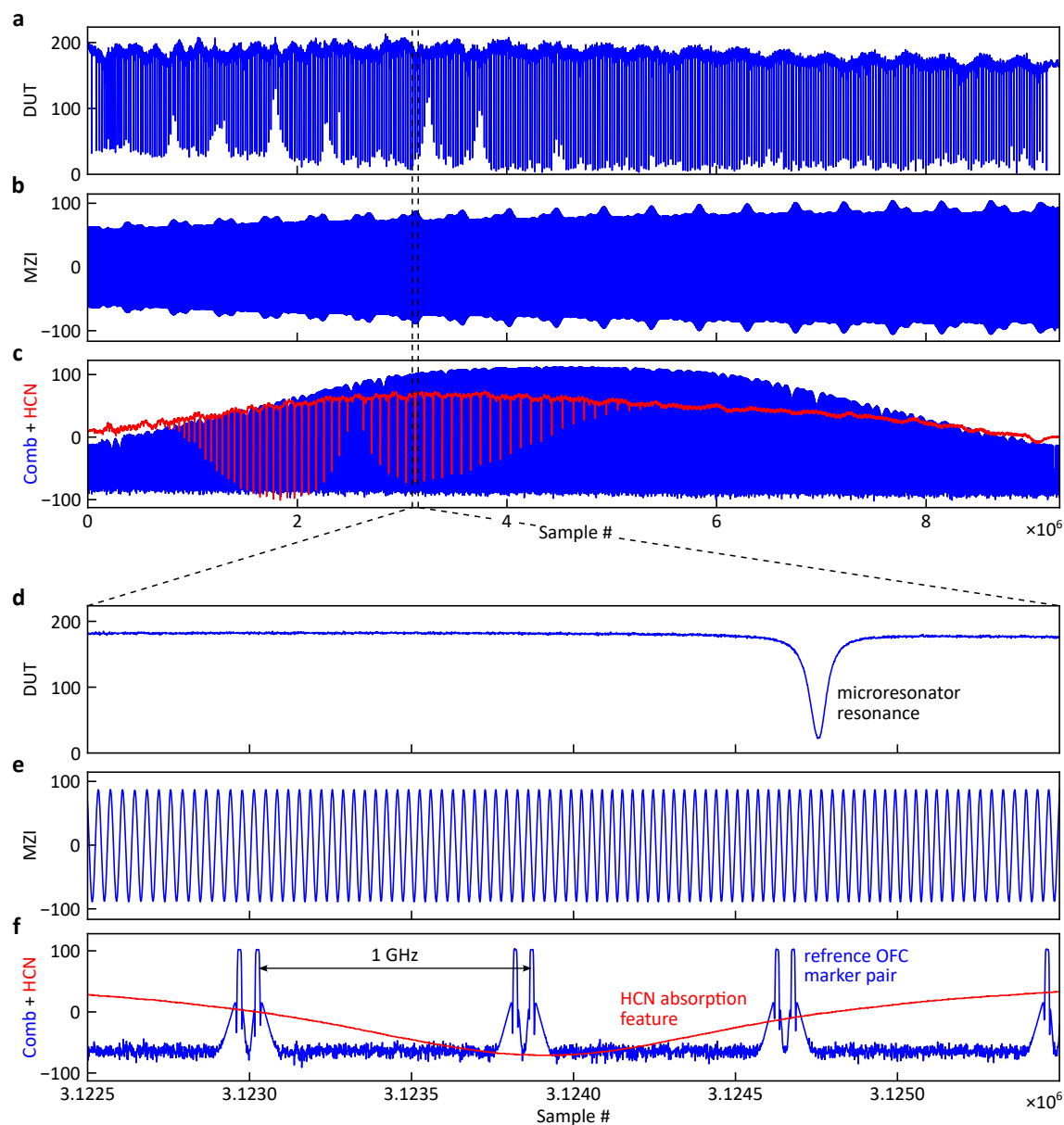


Figure A.4 | FCADLS signals. Example of FCADLS traces covering the range from 1520 nm to 1605 nm (~ 10 THz spectral span). **a**, Device under test (DUT). In this case, the TE transmission signal of a 25 GHz FSR microresonator. **b**, Calibration signal recorded from the Mach-Zehnder interferometer with FSR ~ 40 MHz. **c**, HCN gas cell (red) calibration signal, containing the R- and P-branch absorption features, and comb calibration signal (blue) containing the comb line markers. **d**, **e**, and **f** show the magnified view (approx. $\times 3000$) of the previous panels, spanning approximately 3.5 GHz of optical frequency.

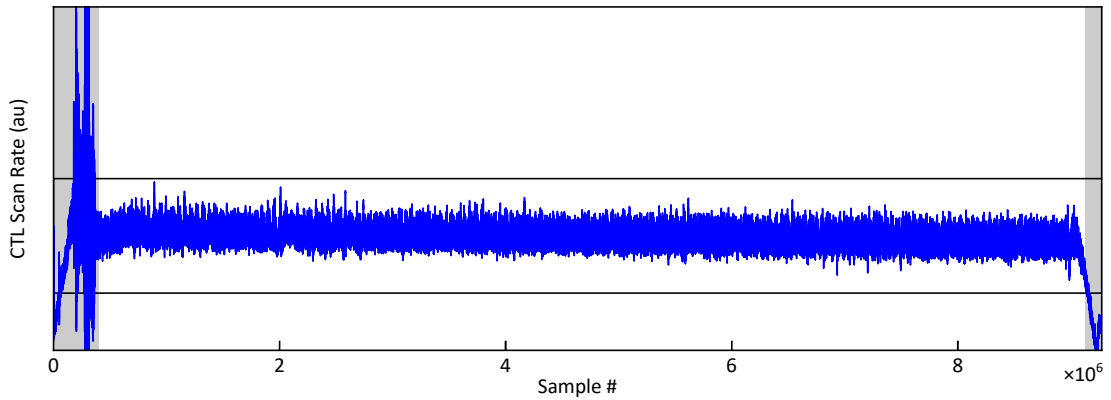


Figure A.5 | EDCL scan rate. Approximate laser scan rate (in arbitrary units) obtained by taking the time derivative of the instantaneous phase of the MZI signal. The acceleration and deceleration of the CTL are visible at the start and the end of the trace, respectively. Before settling on a steady scan rate, the laser transitions briefly through a noisy regime, likely due to stick-slip and/or resonant dynamics of the motor-actuated external feedback mechanism. As clean data is required for calibration, data outside of the 50 % to 150 % range of the median scan rate is disregarded (boundaries are shown as black horizontal lines and disregarded data is highlighted in grey).

ing poor-quality data outside this range, where the scanning laser is either accelerating, decelerating, or behaving erratically. This process is detailed in Figure A.5.

3. The maxima in the comb calibration signal (see Figure A.4f, blue trace) are identified, corresponding to the crossing events t_n between the reference OFC and scanning laser. As shown in Figure A.6, the power detector output is constant within the bandwidth of the band-pass filter. In order to obtain well-defined maxima, the signal is first convolved with a flat-top windowing function before peak detection. Every second marker is then disregarded, keeping only the set of left-side (or right-side) markers with respect to the comb lines. This step establishes a set of points (φ_n, ω_n) , where $\omega_n = \omega_o + n \cdot \omega_{\text{rep}}$ is an equidistant grid of known optical frequencies.
4. Using this grid, an interpolation function is established to map the instantaneous MZI phase φ to optical frequencies ω . This is possible because, unlike the laser frequency $\omega(t)$, the MZI phase signal $\varphi(\omega) = \Delta L \cdot \beta(\omega)$ can be considered to vary linearly between any two calibration markers.
5. Finally, the transmission signal from the HCN gas cell is used to achieve absolute frequency calibration. The R- and P-branch lines, located between 1525 nm

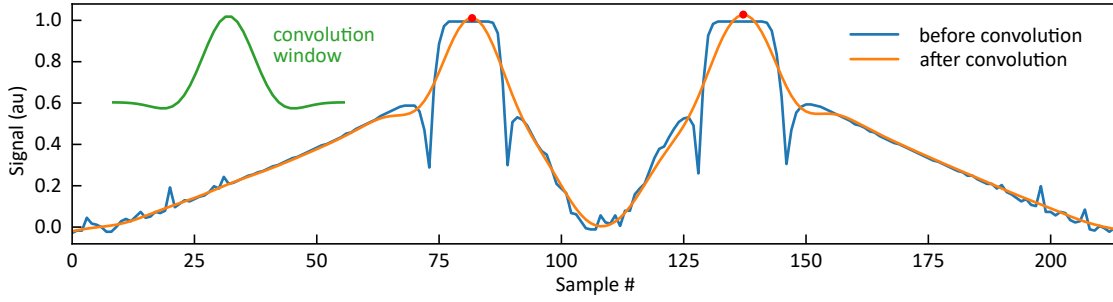


Figure A.6 | Reference OFC marker extraction. The signal from the RF power detector (blue) is flat within the 27 – 33 MHz passband of the RF filter. In order to improve the accuracy of the peak detection algorithm, the signal is first convolved with a windowing function (green). The output signal (orange) has clearly defined maxima from which the calibration markers (red) can be located.

and 1565 nm (see Figure A.4c, red trace) are fitted and collectively used to offset the reconstructed frequency axis to the correct position [262–264]. The line-dependent pressure-shift coefficients have to be accounted for when computing the line frequencies⁴.

A.4 Validation and performance

Several independent methods can be used to validate the calibration and estimate the resulting spectral accuracy.

A.4.1 MZI dispersion

First, the instantaneous phase of the MZI signal can be used to measure the dispersion of the optical fiber composing the interferometer arms. To do so, the phase signal is Taylor-expanded around a central frequency ω_0 as

$$\varphi(\omega) = \Delta L \left(\beta_0 + \beta_1(\omega - \omega_0) + \frac{\beta_2}{2!}(\omega - \omega_0)^2 + \dots \right), \quad (\text{A.1})$$

$$\text{where } \beta_n = \left. \frac{\partial^n \beta(\omega)}{\partial \omega^n} \right|_{\omega=\omega_0} \quad (\text{A.2})$$

are the dispersion coefficients, and ΔL is the length difference between the two arms of the MZI. Subtracting the constant and linear terms from eq. A.1 reveals the effects of higher-order dispersion ($\beta_n, \forall n \geq 2$) as shown in Figure A.7. Specifically, $\beta_2 = \partial^2 \beta / \partial \omega^2$

⁴The HCN gas cell pressure is obtained by minimizing the residuals between the measured and computed line frequencies.

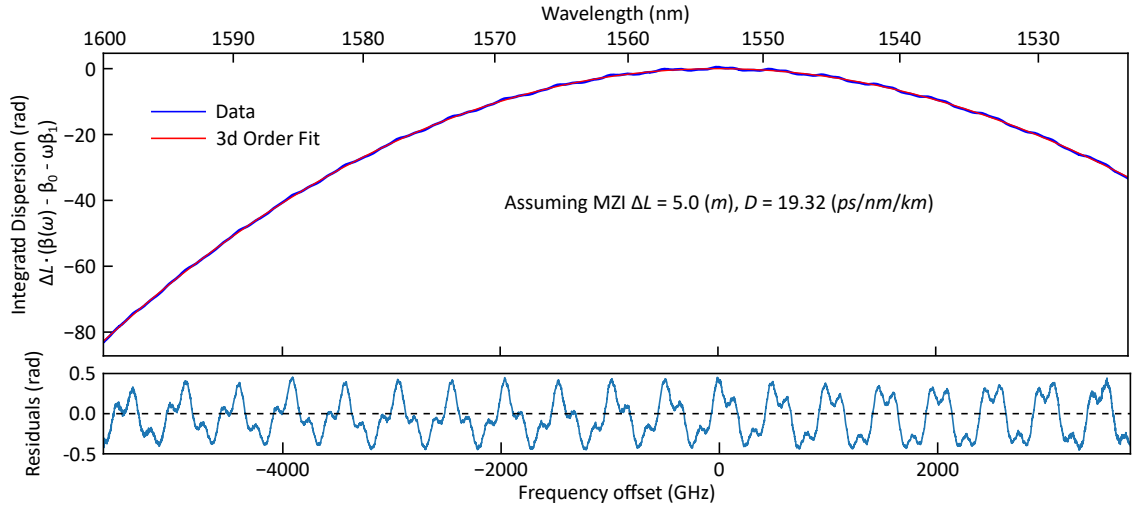


Figure A.7 | Mach-Zehnder interferometer dispersion. Top: Instantaneous phase of the MZI signal with the constant and linear components subtracted (see main text): $\varphi(\omega) - \Delta L(\beta_0 + \beta_1(\omega - \omega_0))$. Deviation from a straight line is due to the presence of the presence of high order dispersion (≥ 2). A 3rd-order fit reveals that the dispersion parameter is $19.32 \text{ ps nm}^{-1} \text{ km}^{-1}$, in excellent agreement with the specification for SMF28 optical fiber. Bottom: Residuals from the 3rd-order fit. Periodic oscillations can be observed, introduced by the 50/50 directional couplers splitting/combing the arms of the MZI. Note that these oscillations are resolved by the reference OFC (spectral oscillation period $\gg \omega_{\text{rep}}/(2\pi)$) and, therefore, corrected by the calibration procedure.

is the group velocity dispersion (GVD), which is directly related to the *dispersion parameter* $D = -\frac{\omega_0^2}{2\pi c} \beta_2$ often used to characterize optical fibers. Typically, a value of $D = 19.3(1) \text{ ps nm}^{-1} \text{ km}^{-1}$ is measured, in excellent agreement with the $D \approx 19 \text{ ps nm}^{-1} \text{ km}^{-1}$ specification of SMF28 fiber.

In practice, this check is performed after step 3 of the calibration procedure to verify that both the instantaneous phase and the calibration markers are correctly extracted. If a comb line were missed, a vertical discontinuity would be observed in the dispersion relation at the frequency of the missing marker, with a step $\Delta L \beta_1 \omega_{\text{rep}}$ corresponding to a frequency error of ω_{rep} after calibration.

A.4.2 Hydrogen cyanide

While the HCN calibration signal is used to set the absolute frequency offset, the residuals between the measured and published line frequencies can be used to estimate the spectral accuracy of the reconstructed frequency axis. Figure A.8 shows an example of these residuals for the R- and P-branch lines as a function of frequency. The RMS devi-

Appendix A. Frequency comb assisted diode laser spectroscopy

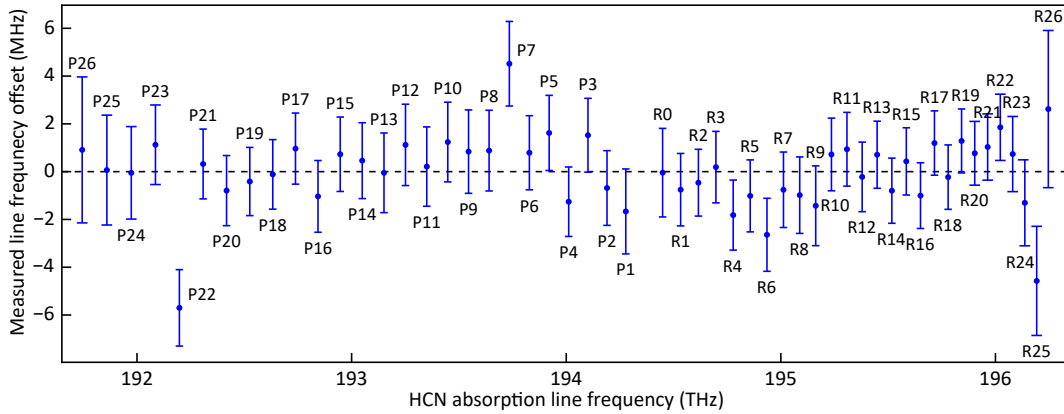


Figure A.8 | HCN spectroscopy. Frequency offset between the measured and published line frequencies. The $\pm 2\sigma$ error bars include the combination of the fit uncertainty and the uncertainty of the published line data used for this work. The residual RMS value is 1.6 MHz.

ation is approximate 1.6 MHz and is limited by the fit uncertainty and the uncertainty of the published data, as shown by the error bars.

From this, we conclude that our FCADLS setup achieves MHz-level spectral accuracy despite the relative broad linewidth of the HCN absorption features (FWHM > 1 GHz). This is largely sufficient for the applications within this work, such as microresonator dispersion measurement, sideband injection locking characterization, and comb reconstruction spectroscopy. Utilizing a calibration source with narrower spectral lines could further improve spectral accuracy.

It is also important to note that the relative spectral accuracy is expected to be significantly better and is primarily limited by the spectrally dependent signal-to-noise ratio of the Mach-Zehnder interferometer and comb calibration signals.

Appendix B

Derivation of coupled mode equations

The *coupled mode equations* approach to modeling Kerr resonator dynamics is a frequency-domain method that describes the temporal evolution of the complex amplitudes of the cavity's (longitudinal) eigenmodes [44, 96]. While strictly equivalent to the wider known *Lugiato–Lefever equation* [83, 88], describing the temporal evolution of the complex intracavity field, CME enable straightforward integration of mode-dependent parameters within numerical simulations, such as dispersion and linewidth data obtained through frequency-assisted diode laser spectroscopy. In this appendix, the coupled mode equations used as the basis for the numerical simulation of Kerr frequency combs in the body of this thesis are derived from the nonlinear wave equation.

B.1 Definitions

Let the nonlinear wave equation be [82, 265]

$$\nabla^2 \tilde{\mathbf{E}} - \frac{n_0^2}{c^2} \frac{\partial^2 \tilde{\mathbf{E}}}{\partial t^2} = \frac{1}{\epsilon_0 c^2} \frac{\partial^2 \tilde{\mathbf{P}}^{\text{NL}}}{\partial t^2}, \quad (\text{B.1})$$

where $\tilde{\mathbf{P}}^{\text{NL}}$ is the nonlinear polarization of a $\chi^{(3)}$ material

$$\tilde{\mathbf{P}}^{\text{NL}} = \epsilon_0 \chi^{(3)} \tilde{\mathbf{E}}^3. \quad (\text{B.2})$$

The electric field inside a high-Q resonator can be expressed as a linear combination of the cavity's eigenmodes

$$\tilde{\mathbf{E}}(t, \mathbf{r}) = \sum_{\mu} E_{\mu} \mathbf{F}_{\mu}(\mathbf{r}) e^{-j\omega_{\mu} t} + \text{c.c.}, \quad (\text{B.3})$$

Appendix B. Derivation of coupled mode equations

where E_μ are the slow-varying mode amplitudes¹, $\mathbf{F}_\mu(\mathbf{r})$ the cavity eigenmodes and c.c. the complex conjugate. The cavity eigenmodes are orthogonal and normalized such that

$$\langle \mathbf{F}_\mu, \mathbf{F}_\eta \rangle = \int_V \mathbf{F}_\mu(\mathbf{r}) \cdot \mathbf{F}_\eta^*(\mathbf{r}) dV = \begin{cases} 1, & \text{if } \mu = \eta \\ 0, & \text{if } \mu \neq \eta \end{cases}. \quad (\text{B.4})$$

We make the assumption that the waveguide is uniform in cross-section such that the cavity eigenmodes can be expressed as the product of a plane wave and a transverse field profile $\bar{\mathbf{F}}_\mu(x, y)$

$$\mathbf{F}_\mu(\mathbf{r}) = \bar{\mathbf{F}}_\mu(x, y) e^{j\beta_\mu z}, \quad (\text{B.5})$$

$$\text{where } \beta_\mu = \mu \frac{2\pi}{L}. \quad (\text{B.6})$$

Here β_μ is the propagation constant of the μ^{th} mode and L is the round-trip length of the cavity. Note that due to the choice of normalization for $\mathbf{F}_\mu(\mathbf{r})$

$$\langle \bar{\mathbf{F}}_\mu, \bar{\mathbf{F}}_\mu \rangle = \iint_S \bar{\mathbf{F}}_\mu(x, y) \cdot \bar{\mathbf{F}}_\mu^*(x, y) dx dy = \frac{1}{L}, \quad (\text{B.7})$$

where the integral is carried over the waveguide's transverse plane S . Finally, we define the effective mode area A_{eff} as

$$A_{\text{eff}} := \frac{\left(\iint |\bar{\mathbf{F}}_\mu(x, y)|^2 dx dy \right)^2}{\iint |\bar{\mathbf{F}}_\mu(x, y)|^4 dx dy} = \frac{1}{L^2 \iint |\bar{\mathbf{F}}_\mu(x, y)|^4 dx dy}, \quad (\text{B.8})$$

and the effective mode volume as $V_{\text{eff}} := LA_{\text{eff}}$. Note that A_{eff} and V_{eff} are independent of our choice of normalization for $\mathbf{F}_\mu(\mathbf{r})$.

B.2 Derivation

B.2.1 Removal of spatial dependencies

We start by substituting eq. B.3 into the wave eq. B.1. To simplify the redaction, we will process the left-hand side (LHS) and right-hand side (RHS) separately.

¹We drop the time dependence of the slow-varying amplitudes to simplify notation.

For the LHS of eq. B.1, we find, for Laplacian of the electric field

$$\nabla^2 \tilde{\mathbf{E}} = \sum_{\mu} \mathbf{E}_{\mu} e^{-j\omega_{\mu} t} \nabla^2 \mathbf{F}_{\mu}(\mathbf{r}) + \text{c.c.}, \quad (\text{B.9})$$

and for the second term

$$\begin{aligned} -\frac{n_0^2}{c^2} \frac{\partial^2 \tilde{\mathbf{E}}}{\partial t^2} &= -\frac{n_0^2}{c^2} \sum_{\mu} \mathbf{F}_{\mu}(\mathbf{r}) \frac{\partial^2}{\partial t^2} \left(\mathbf{E}_{\mu} e^{-j\omega_{\mu} t} \right) + \text{c.c.} \\ &= -\frac{n_0^2}{c^2} \sum_{\mu} \mathbf{F}_{\mu}(\mathbf{r}) \left(\ddot{\mathbf{E}}_{\mu} - 2j\omega_{\mu} \dot{\mathbf{E}}_{\mu} - \omega_{\mu}^2 \mathbf{E}_{\mu} \right) e^{-j\omega_{\mu} t} + \text{c.c.} \end{aligned} \quad (\text{B.10})$$

Combining both terms, the LHS can be rewritten as

$$\begin{aligned} \nabla^2 \tilde{\mathbf{E}} - \frac{n_0^2}{c^2} \frac{\partial^2 \tilde{\mathbf{E}}}{\partial t^2} &= \\ \sum_{\mu} \mathbf{E}_{\mu} e^{-j\omega_{\mu} t} \left(\nabla^2 + \frac{n_0^2 \omega_{\mu}^2}{c^2} \right) \mathbf{F}_{\mu}(\mathbf{r}) - \frac{n_0^2}{c^2} \sum_{\mu} \mathbf{F}_{\mu}(\mathbf{r}) \left(\ddot{\mathbf{E}}_{\mu} - 2j\omega_{\mu} \dot{\mathbf{E}}_{\mu} \right) e^{-j\omega_{\mu} t} &+ \text{c.c.}, \end{aligned} \quad (\text{B.11})$$

where the first term vanishes as the cavity eigenmodes $\mathbf{F}_{\mu}(\mathbf{r})$ are by definition solutions to the Helmholtz equation $(\nabla^2 + n_0^2 \omega_{\mu}^2 / c^2) \mathbf{F}_{\mu}(\mathbf{r}) = 0$. Additionally we make the slow varying envelope assumption $|\ddot{\mathbf{E}}_{\mu}| \ll |2\omega_{\mu} \dot{\mathbf{E}}_{\mu}|$, such that we are left with

$$\nabla^2 \tilde{\mathbf{E}} - \frac{n_0^2}{c^2} \frac{\partial^2 \tilde{\mathbf{E}}}{\partial t^2} \approx 2j \frac{n_0^2}{c^2} \sum_{\mu} \mathbf{F}_{\mu}(\mathbf{r}) \omega_{\mu} \dot{\mathbf{E}}_{\mu} e^{-j\omega_{\mu} t} + \text{c.c.} \quad (\text{B.12})$$

For the RHS of eq. B.1 we find

$$\begin{aligned} \frac{1}{\epsilon_0 c^2} \frac{\partial^2 \tilde{\mathbf{P}}^{\text{NL}}}{\partial t^2} &= \frac{\chi^{(3)}}{c^2} \frac{\partial^2 \tilde{\mathbf{E}}^3}{\partial t^2} \\ &= \frac{\chi^{(3)}}{c^2} \frac{\partial^2}{\partial t^2} \left(\sum_{\mu} \mathbf{E}_{\mu} \mathbf{F}_{\mu}(\mathbf{r}) e^{-j\omega_{\mu} t} + \text{c.c.} \right)^3 \\ &\approx 3 \frac{\chi^{(3)}}{c^2} \sum_{\mu, \mu', \mu''} \frac{\partial^2}{\partial t^2} \left(\mathbf{E}_{\mu} \mathbf{E}_{\mu'} \mathbf{E}_{\mu''}^* \mathbf{F}_{\mu}(\mathbf{r}) \mathbf{F}_{\mu'}(\mathbf{r}) \mathbf{F}_{\mu''}^*(\mathbf{r}) e^{-j(\omega_{\mu} + \omega_{\mu'} - \omega_{\mu''}) t} + \text{c.c.} \right) \end{aligned} \quad (\text{B.13})$$

where we have omitted the terms corresponding to triple-sum and third-harmonic generation. We once again use the slow varying envelope assumption $|\ddot{\mathbf{E}}_{\mu}| \ll |2\omega_{\mu} \dot{\mathbf{E}}_{\mu}| \ll$

Appendix B. Derivation of coupled mode equations

$|\omega_\mu^2|$ and derive

$$\frac{1}{\epsilon_0 c^2} \frac{\partial^2 \tilde{\mathbf{P}}^{\text{NL}}}{\partial t^2} = 3 \frac{\chi^{(3)}}{c^2} \sum_{\mu, \mu', \mu''} -(\omega_\mu + \omega_{\mu'} - \omega_{\mu''})^2 E_\mu E_{\mu'} E_{\mu''}^* \cdot \mathbf{F}_\mu(\mathbf{r}) \mathbf{F}_{\mu'}(\mathbf{r}) \mathbf{F}_{\mu''}^*(\mathbf{r}) e^{-j(\omega_\mu + \omega_{\mu'} - \omega_{\mu''})t} + \text{c.c.} \quad (\text{B.13})$$

We then assume we are working around a central frequency ω_0 such that $(\omega_\mu + \omega_{\mu'} - \omega_{\mu''})^2 \approx \omega_0^2$

$$\frac{1}{\epsilon_0 c^2} \frac{\partial^2 \tilde{\mathbf{P}}^{\text{NL}}}{\partial t^2} = -\frac{3\omega_0^2 \chi^{(3)}}{c^2} \sum_{\mu, \mu', \mu''} E_\mu E_{\mu'} E_{\mu''}^* \mathbf{F}_\mu(\mathbf{r}) \mathbf{F}_{\mu'}(\mathbf{r}) \mathbf{F}_{\mu''}^*(\mathbf{r}) e^{-j(\omega_\mu + \omega_{\mu'} - \omega_{\mu''})t} + \text{c.c.} \quad (\text{B.13})$$

B.3 Projection

We now project the equation on a given mode η by multiplying by $\mathbf{F}_\eta^*(\mathbf{r})$ and integrating over volume.

For the **LHS** we have

$$\int_V \mathbf{F}_\eta^*(\mathbf{r}) \cdot \left(\nabla^2 \tilde{\mathbf{E}} - \frac{n_0^2}{c^2} \frac{\partial^2 \tilde{\mathbf{E}}}{\partial t^2} \right) dV = 2j \frac{n_0^2}{c^2} \sum_\mu \int_V \mathbf{F}_\eta^*(\mathbf{r}) \cdot \left(\mathbf{F}_\mu(\mathbf{r}) \omega_\mu \dot{E}_\mu e^{-j\omega_\mu t} + \text{c.c.} \right) dV \quad (\text{B.14})$$

$$= 2j \frac{n_0^2}{c^2} \sum_\mu \omega_\mu \dot{E}_\mu e^{-j\omega_\mu t} \langle \mathbf{F}_\mu, \mathbf{F}_\eta \rangle + \text{c.c.} \quad (\text{B.15})$$

$$= 2j \frac{n_0^2}{c^2} \omega_\eta \dot{E}_\eta e^{-j\omega_\eta t}, \quad (\text{B.16})$$

where we have used eq. B.4. Note that the c.c. components disappears as $\langle \mathbf{F}_\mu^*, \mathbf{F}_\eta \rangle = 0, \forall \mu$.

For the **RHS** we have

$$\int_V \mathbf{F}_\eta^*(\mathbf{r}) \cdot \left(\frac{1}{\epsilon_0 c^2} \frac{\partial^2 \tilde{\mathbf{P}}^{\text{NL}}}{\partial t^2} \right) dV = -\frac{3\omega_0^2 \chi^{(3)}}{c^2} \sum_{\mu, \mu', \mu''} E_\mu E_{\mu'} E_{\mu''}^* e^{-j(\omega_\mu + \omega_{\mu'} - \omega_{\mu''})t} \cdot \int_V \mathbf{F}_\mu(\mathbf{r}) \mathbf{F}_{\mu'}(\mathbf{r}) \mathbf{F}_{\mu''}^*(\mathbf{r}) \mathbf{F}_\eta^*(\mathbf{r}) dV \quad (\text{B.17})$$

We then use eq. B.5 and make the assumption that all eigenmodes share a common

transverse field profile $\tilde{\mathbf{F}}_\mu(x, y) = \tilde{\mathbf{F}}(x, y)$

$$\int_V \mathbf{F}_\mu(\mathbf{r}) \mathbf{F}_{\mu'}(\mathbf{r}) \mathbf{F}_{\mu''}^*(\mathbf{r}) \mathbf{F}_\eta^*(\mathbf{r}) dV = \int_V |\tilde{\mathbf{F}}(x, y)|^4 e^{j\frac{2\pi}{L}(\mu + \mu' - \mu'' - \eta)z} dV \quad (\text{B.18})$$

$$= \begin{cases} V_{\text{eff}}^{-1}, & \text{if } \mu + \mu' - \mu'' - \eta = 0 \\ 0, & \text{otherwise} \end{cases}, \quad (\text{B.19})$$

where we have used eq. B.8. Note that again, the c.c. components disappear as no combination can yield $\mu'' - \mu - \mu' - \eta = 0$.

We now **combine** both sides of the equation to get

$$\dot{E}_\eta = j \frac{3\omega_0 \chi^{(3)}}{2n^2 V_{\text{eff}}} \sum_{\mu, \mu', \mu''} E_\mu E_{\mu'} E_{\mu''}^* e^{-j(\omega_\mu + \omega_{\mu'} - \omega_{\mu''} - \omega_\eta)t}, \quad (\text{B.20})$$

summing over $\forall \mu, \mu', \mu''$ respecting $\mu + \mu' - \mu'' = \eta$.

B.4 Normalization

Let the time-averaged Poynting vector for mode μ be

$$\langle \tilde{\mathbf{P}}_\mu \rangle = \langle \tilde{\mathbf{E}}_\mu \times \tilde{\mathbf{H}}_\mu \rangle = \frac{1}{2} \mathbf{E}_\mu \times \mathbf{H}_\mu \quad (\text{B.21})$$

where $\tilde{\mathbf{E}}_\mu = \Re \mathbf{E}_\mu \cdot e^{-j\omega t}$ and $\tilde{\mathbf{H}}_\mu = \Re \mathbf{H}_\mu \cdot e^{-j\omega t}$. In the scalar case, we make the approximation that $|\mathbf{H}_\mu| = n\epsilon_0 c \cdot |\mathbf{E}_\mu|$ and that $\tilde{\mathbf{P}}_\mu$ is co-axial with the waveguide and has magnitude

$$|\langle \tilde{\mathbf{P}}_\mu \rangle| = \frac{n\epsilon_0 c}{2} |\mathbf{E}_\mu|^2 \quad (\text{B.22})$$

Therefore, the circulating power for mode μ is obtained by integrating the time-averaged Poynting vector over the waveguide cross-section

$$\begin{aligned} P_\mu &= \frac{n\epsilon_0 c}{2} \iint |\mathbf{E}_\mu|^2 dx dy \\ &= 2n\epsilon_0 c \iint |E_\mu \mathbf{F}_\mu(\mathbf{r})|^2 dx dy \\ &= 2n\epsilon_0 c |E_\mu|^2 \iint |\tilde{\mathbf{F}}(x, y)|^2 dx dy \\ &= \frac{2n\epsilon_0 c}{L} |E_\mu|^2 \end{aligned} \quad (\text{B.23})$$

Appendix B. Derivation of coupled mode equations

where we have used eq. B.3 and B.7. We then introduce the normalized mode amplitude A_μ such that $|A_\mu|^2$ is the number of quanta in the cavity in mode μ , by dividing by the photon energy $\hbar\omega_\mu$ and multiplying by the cavity round-trip time $\frac{nL}{c}$

$$|A_\mu|^2 = P_\mu \frac{nL}{c\hbar\omega_\mu} = \frac{2\epsilon_0 n^2}{\hbar\omega_\mu} |E_\mu|^2 \quad (\text{B.24})$$

yielding

$$E_\mu = A_\mu \sqrt{\frac{\hbar\omega_\mu}{2\epsilon_0 n^2}} \quad (\text{B.25})$$

that we then substitute in eq. B.20

$$\dot{A}_\eta = j \frac{3\omega_0 \chi^{(3)}}{2n^2 V_{\text{eff}}} \frac{\hbar\omega_\eta}{2\epsilon_0 n^2} \sum_{\mu, \mu', \mu''} A_\mu A_{\mu'} A_{\mu''}^* e^{-j(\omega_\mu + \omega_{\mu'} - \omega_{\mu''} - \omega_\eta)t} \quad (\text{B.26})$$

We introduce this as well as the nonlinear index $n_2 = \frac{3}{4n_0^2 \epsilon_0 c} \chi^{(3)}$ into eq. B.26 and get

$$\dot{A}_\eta = j \frac{\hbar\omega_0^2 c n_2}{n^2 V_{\text{eff}}} \sum_{\mu, \mu', \mu''} A_\mu A_{\mu'} A_{\mu''}^* e^{-j(\omega_\mu + \omega_{\mu'} - \omega_{\mu''} - \omega_\eta)t} \quad (\text{B.27})$$

$$= jg \sum_{\mu, \mu', \mu''} A_\mu A_{\mu'} A_{\mu''}^* e^{-j(\omega_\mu + \omega_{\mu'} - \omega_{\mu''} - \omega_\eta)t} \quad (\text{B.28})$$

where g is the nonlinear coupling coefficient

$$g = \frac{\hbar\omega_0^2 c n_2}{n^2 V_{\text{eff}}} \quad (\text{B.29})$$

B.5 Decay and pump

Including the cavity decay rate κ , we get

$$\dot{A}_\eta = -\frac{\kappa}{2} A_\eta + jg \sum_{\mu, \mu', \mu''} A_\mu A_{\mu'} A_{\mu''}^* e^{-j(\omega_\mu + \omega_{\mu'} - \omega_{\mu''} - \omega_\eta)t}. \quad (\text{B.30})$$

We then consider a pump s (such that $|s|^2$ is the pump's photon flux) with frequency ω_p and $|\omega_p - \omega_0|$ much smaller than the cavity FSR such that it only contributes to mode $\eta = 0$

$$\dot{A}_\eta = -\frac{\kappa}{2} A_\eta \delta_\eta \sqrt{\kappa} e s e^{-j(\omega_p - \omega_0)t} + jg \sum_{\mu, \mu', \mu''} A_\mu A_{\mu'} A_{\mu''}^* e^{-j(\omega_\mu + \omega_{\mu'} - \omega_{\mu''} - \omega_\eta)t} \quad (\text{B.31})$$

B.5. Decay and pump

where δ_η is the Kronecker delta such that $\delta_\eta = 0$ except for $\delta_0 = 1$.

Introducing the following normalization:

$$\tau = \frac{\kappa}{2} t, \quad \zeta_\mu = \frac{2(\omega_\mu - \omega_p - \mu D_1)}{\kappa}, \quad f = \sqrt{\frac{8\eta g_0}{\kappa^2}} \sin, \quad a_\mu = \sqrt{\frac{2g_0}{\kappa}} A_\mu e^{-i(\omega_\mu - \omega_p - \mu D_1)t} \quad (\text{B.32})$$

enables the system to be rewritten in its dimensionless form:

$$\frac{\partial a_\mu}{\partial \tau} = -(1 + i\zeta_\mu) a_\mu + i \sum_{\mu', \mu''} a_{\mu'} a_{\mu''} a_{\mu' + \mu'' - \mu}^* + \delta_\mu f. \quad (\text{B.33})$$

Bibliography

1. Hall, J. L. Nobel Lecture: Defining and measuring optical frequencies. *Reviews of Modern Physics* **78**, 1279–1295 (Nov. 17, 2006).
2. Hänsch, T. W. Nobel Lecture: Passion for precision. *Reviews of Modern Physics* **78**, 1297–1309. ISSN: 0034-6861, 1539-0756 (Nov. 17, 2006).
3. Udem, T., Holzwarth, R. & Hänsch, T. W. Optical frequency metrology. *Nature* **416**, 233–237. ISSN: 00280836 (2002).
4. Fortier, T. & Baumann, E. 20 years of developments in optical frequency comb technology and applications. *Communications Physics* **2**, 1–16. ISSN: 2399-3650 (Dec. 6, 2019).
5. Cundiff, S. T. & Ye, J. Colloquium: Femtosecond optical frequency combs. *Reviews of Modern Physics* **75**, 325–342 (Mar. 10, 2003).
6. Udem, T., Reichert, J., Holzwarth, R. & Hänsch, T. W. Accurate measurement of large optical frequency differences with a mode-locked laser. *Optics Letters* **24**, 881–883. ISSN: 1539-4794 (July 1, 1999).
7. Udem, T., Reichert, J., Holzwarth, R. & Hänsch, T. W. Absolute Optical Frequency Measurement of the Cesium D1 Line with a Mode-Locked Laser. *Physical Review Letters* **82**, 3568–3571 (May 3, 1999).
8. Reichert, J., Niering, M., Holzwarth, R., Weitz, M., Udem, T. & Hänsch, T. W. Phase Coherent Vacuum-Ultraviolet to Radio Frequency Comparison with a Mode-Locked Laser. *Physical Review Letters* **84**, 3232–3235 (Apr. 10, 2000).
9. Diddams, S. A., Jones, D. J., Ye, J., Cundiff, S. T., Hall, J. L., Ranka, J. K., Windeler, R. S., Holzwarth, R., Udem, T. & Hänsch, T. W. Direct Link between Microwave and Optical Frequencies with a 300 THz Femtosecond Laser Comb. *Physical Review Letters* **84**, 5102–5105 (May 2000).
10. Telle, H., Steinmeyer, G., Dunlop, A., Stenger, J., Sutter, D. & Keller, U. Carrier-envelope offset phase control: A novel concept for absolute optical frequency measurement and ultrashort pulse generation. *Applied physics. B, Lasers and optics* **69**, 327–332. ISSN: 0946-2171, 1432-0649 (Oct. 1999).

Bibliography

11. Holzwarth, R., Udem, T., Hänsch, T. W., Knight, J. C., Wadsworth, W. J. & Russell, P. S. J. Optical Frequency Synthesizer for Precision Spectroscopy. *Physical Review Letters* **85**, 2264–2267 (Sept. 2000).
12. Jones, D. J., Diddams, S. A., Ranka, J. K., Stentz, A., Windeler, R. S., Hall, J. L. & Cundiff, S. T. Carrier-Envelope Phase Control of Femtosecond Mode-Locked Lasers and Direct Optical Frequency Synthesis. *Science* **288**, 635–639 (Apr. 2000).
13. *Femtosecond optical frequency comb: principle, operation, and applications* (eds Ye, J. & Cundiff, S. T.) (Springer, New York, NY, 2005). 361 pp. ISBN: 978-0-387-23790-9.
14. Picqué, N. & Hänsch, T. W. Frequency comb spectroscopy. *Nature Photonics* **13**, 146–157. ISSN: 17494893 (2019).
15. Coddington, I., Swann, W. C., Nenadovic, L. & Newbury, N. R. Rapid and precise absolute distance measurements at long range. *Nature Photonics* **3**, 351–356. ISSN: 1749-4893 (June 2009).
16. Van Rooij, R., Borbely, J. S., Simonet, J., Hoogerland, M. D., Eikema, K. S. E., Rozendaal, R. A. & Vassen, W. Frequency Metrology in Quantum Degenerate Helium: Direct Measurement of the $2\ 3S1 \rightarrow 2\ 1S0$ Transition. *Science* **333**, 196–198 (July 8, 2011).
17. Keilmann, F., Gohle, C. & Holzwarth, R. Time-domain mid-infrared frequency-comb spectrometer. *Optics Letters* **29**, 1542–1544. ISSN: 1539-4794 (July 1, 2004).
18. Gohle, C., Udem, T., Herrmann, M., Rauschenberger, J., Holzwarth, R., Schuessler, H. A., Krausz, F. & Hänsch, T. W. A frequency comb in the extreme ultraviolet. *Nature* **436**, 234–237. ISSN: 1476-4687 (July 2005).
19. Jones, R. J., Moll, K. D., Thorpe, M. J. & Ye, J. Phase-Coherent Frequency Combs in the Vacuum Ultraviolet via High-Harmonic Generation inside a Femtosecond Enhancement Cavity. *Physical Review Letters* **94**, 193201 (May 20, 2005).
20. Witte, S., Zinkstok, R. T., Ubachs, W., Hogervorst, W. & Eikema, K. S. E. Deep-Ultraviolet Quantum Interference Metrology with Ultrashort Laser Pulses. *Science* **307**, 400–403 (Jan. 21, 2005).
21. Diddams, S. A., Hollberg, L. & Mbele, V. Molecular fingerprinting with the resolved modes of a femtosecond laser frequency comb. *Nature* **445**, 627–630. ISSN: 1476-4687 (Feb. 2007).
22. Mandon, J., Guelachvili, G. & Picqué, N. Fourier transform spectroscopy with a laser frequency comb. *Nature Photonics* **3**, 99–102. ISSN: 1749-4893 (Feb. 2009).
23. Bernhardt, B., Ozawa, A., Jacquet, P., Jacquy, M., Kobayashi, Y., Udem, T., Holzwarth, R., Guelachvili, G., Hänsch, T. W. & Picqué, N. Cavity-enhanced dual-comb spectroscopy. *Nature Photonics* **4**, 55–57. ISSN: 1749-4893 (Jan. 2010).

24. Cingöz, A., Yost, D. C., Allison, T. K., Ruehl, A., Fermann, M. E., Hartl, I. & Ye, J. Direct frequency comb spectroscopy in the extreme ultraviolet. *Nature* **482**, 68–71. ISSN: 1476-4687 (Feb. 2012).
25. Diddams, S. A., Udem, T., Bergquist, J. C., Curtis, E. A., Drullinger, R. E., Hollberg, L., Itano, W. M., Lee, W. D., Oates, C. W., Vogel, K. R. & Wineland, D. J. An Optical Clock Based on a Single Trapped $^{199}\text{Hg}^+$ Ion. *Science* **293**, 825–828. ISSN: 0036-8075, 1095-9203 (Aug. 2001).
26. Holzwarth, R., Zimmermann, M., Udem, T. & Hansch, T. Optical clockworks and the measurement of laser frequencies with a mode-locked frequency comb. *IEEE Journal of Quantum Electronics* **37**, 1493–1501. ISSN: 1558-1713 (Dec. 2001).
27. Campbell, C. J., Radnaev, A. G., Kuzmich, A., Dzuba, V. A., Flambaum, V. V. & Derevianko, A. Single-Ion Nuclear Clock for Metrology at the 19th Decimal Place. *Physical Review Letters* **108**, 120802 (Mar. 22, 2012).
28. McFerran, J., Ivanov, E., Bartels, A., Wilpers, G., Oates, C., Diddams, S. & Hollberg, L. Low-noise synthesis of microwave signals from an optical source. *Electronics Letters* **41**, 650. ISSN: 00135194 (2005).
29. Murphy, M. T., Udem, T., Holzwarth, R., Sizmann, A., Pasquini, L., Araujo-Hauck, C., Dekker, H., D’Odorico, S., Fischer, M., Hänsch, T. W. & Manescau, A. High-precision wavelength calibration of astronomical spectrographs with laser frequency combs. *Monthly Notices of the Royal Astronomical Society* **380**, 839–847. ISSN: 0035-8711 (Aug. 2007).
30. Steinmetz, T., Wilken, T., Araujo-Hauck, C., Holzwarth, R., Hänsch, T. W., Pasquini, L., Manescau, A., D’Odorico, S., Murphy, M. T., Kentischer, T., Schmidt, W. & Udem, T. Laser Frequency Combs for Astronomical Observations. *Science* **321**, 1335–1337. ISSN: 0036-8075, 1095-9203 (Sept. 2008).
31. Li, C.-H., Benedick, A. J., Fendel, P., Glenday, A. G., Kärtner, F. X., Phillips, D. F., Sasselov, D., Szentgyorgyi, A. & Walsworth, R. L. A laser frequency comb that enables radial velocity measurements with a precision of 1 cm s⁻¹. *Nature* **452**, 610–612. ISSN: 1476-4687 (Apr. 2008).
32. Braje, D. A., Kirchner, M. S., Osterman, S., Fortier, T. & Diddams, S. A. Astronomical spectrograph calibration with broad-spectrum frequency combs. *The European Physical Journal D* **48**, 57–66. ISSN: 1434-6079 (June 1, 2008).
33. Mocker, H. W. & Collins, R. J. MODE COMPETITION AND SELF-LOCKING EFFECTS IN A Q -SWITCHED RUBY LASER. *Applied Physics Letters* **7**, 270–273. ISSN: 0003-6951, 1077-3118 (Nov. 15, 1965).
34. Cundiff, S. T. Phase stabilization of ultrashort optical pulses. *Journal of Physics D: Applied Physics* **35**, R43. ISSN: 0022-3727 (Apr. 2002).

Bibliography

35. Keller, U. Recent developments in compact ultrafast lasers. *Nature* **424**. ISSN: 1476-4687 (Aug. 14, 2003).
36. Vahala, K. J. Optical microcavities. *Nature* **424**, 839–846. ISSN: 1476-4687 (Aug. 2003).
37. Del’Haye, P., Schliesser, A., Arcizet, O., Wilken, T., Holzwarth, R. & Kippenberg, T. J. Optical frequency comb generation from a monolithic microresonator. *Nature* **450**, 1214–1217. ISSN: 1476-4687 (Dec. 2007).
38. Razzari, L., Duchesne, D., Ferrera, M., Morandotti, R., Chu, S., Little, B. E. & Moss, D. J. CMOS-compatible integrated optical hyper-parametric oscillator. *Nature Photonics* **4**, 41–45. ISSN: 1749-4885, 1749-4893 (Jan. 2010).
39. Webb, K. E., Erkintalo, M., Coen, S. & Murdoch, S. G. Experimental observation of coherent cavity soliton frequency combs in silica microspheres. *Optics Letters* **41**, 4613–4616. ISSN: 1539-4794 (Oct. 15, 2016).
40. Savchenkov, A. A., Matsko, A. B., Ilchenko, V. S., Solomatine, I., Seidel, D. & Maleki, L. Tunable Optical Frequency Comb with a Crystalline Whispering Gallery Mode Resonator. *Physical Review Letters* **101**, 093902. ISSN: 0031-9007, 1079-7114 (Aug. 2008).
41. Grudinin, I. S., Yu, N. & Maleki, L. Generation of optical frequency combs with a CaF₂ resonator. *Optics Letters* **34**, 878–880. ISSN: 1539-4794 (Apr. 1, 2009).
42. Liang, W., Savchenkov, A. A., Matsko, A. B., Ilchenko, V. S., Seidel, D. & Maleki, L. Generation of near-infrared frequency combs from a MgF₂ whispering gallery mode resonator. *Optics Letters* **36**, 2290–2292. ISSN: 1539-4794 (June 15, 2011).
43. Wang, C. Y., Herr, T., Del’Haye, P., Schliesser, A., Hofer, J., Holzwarth, R., Hänsch, T. W., Picqué, N. & Kippenberg, T. J. Mid-infrared optical frequency combs at 2.5 μm based on crystalline microresonators. *Nature Communications* **4**, 1345. ISSN: 2041-1723 (Jan. 8, 2013).
44. Herr, T., Brasch, V., Jost, J. D., Wang, C. Y., Kondratiev, N. M., Gorodetsky, M. L. & Kippenberg, T. J. Temporal solitons in optical microresonators. *Nature Photonics* **8**, 145–152. ISSN: 1749-4893 (Feb. 2014).
45. Liang, W., Eliyahu, D., Ilchenko, V. S., Savchenkov, A. A., Matsko, A. B., Seidel, D. & Maleki, L. High spectral purity Kerr frequency comb radio frequency photonic oscillator. *Nature Communications* **6**, 7957. ISSN: 2041-1723 (Aug. 11, 2015).
46. Jung, H., Xiong, C., Fong, K. Y., Zhang, X. & Tang, H. X. Optical frequency comb generation from aluminum nitride microring resonator. *Optics Letters* **38**, 2810. ISSN: 0146-9592, 1539-4794 (Aug. 2013).
47. Gong, Z., Bruch, A., Shen, M., Guo, X., Jung, H., Fan, L., Liu, X., Zhang, L., Wang, J., Li, J., Yan, J. & Tang, H. X. High-fidelity cavity soliton generation in crystalline

- ALN micro-ring resonators. *Optics Letters* **43**, 4366–4369. ISSN: 1539-4794 (Sept. 15, 2018).
48. Hausmann, B. J. M., Bulu, I., Venkataraman, V., Deotare, P. & Lončar, M. Diamond nonlinear photonics. *Nature Photonics* **8**, 369–374. ISSN: 1749-4893 (May 2014).
 49. Wilson, D. J., Schneider, K., Hönl, S., Anderson, M., Baumgartner, Y., Czornomaz, L., Kippenberg, T. J. & Seidler, P. Integrated gallium phosphide nonlinear photonics. *Nature Photonics* **14**, 57–62 (2020).
 50. Levy, J. S., Gondarenko, A., Foster, M. A., Turner-Foster, A. C., Gaeta, A. L. & Lipson, M. CMOS-compatible multiple-wavelength oscillator for on-chip optical interconnects. *Nature Photonics* **4**, 37–40. ISSN: 1749-4893 (Jan. 2010).
 51. Okawachi, Y., Saha, K., Levy, J. S., Wen, Y. H., Lipson, M. & Gaeta, A. L. Octave-spanning frequency comb generation in a silicon nitride chip. *Optics Letters* **36**, 3398. ISSN: 0146-9592, 1539-4794 (Sept. 2011).
 52. Foster, M. A., Levy, J. S., Kuzucu, O., Saha, K., Lipson, M. & Gaeta, A. L. Silicon-based monolithic optical frequency comb source. *Opt. Express, OE* **19**, 14233–14239. ISSN: 1094-4087 (July 2011).
 53. Herr, T., Hartinger, K., Riemensberger, J., Wang, C. Y., Gavartin, E., Holzwarth, R., Gorodetsky, M. L. & Kippenberg, T. J. Universal formation dynamics and noise of Kerr-frequency combs in microresonators. *Nature Photonics* **6**, 480–487. ISSN: 1749-4893 (July 2012).
 54. Brasch, V., Geiselmann, M., Herr, T., Lihachev, G., Pfeiffer, M. H. P., Gorodetsky, M. L. & Kippenberg, T. J. Photonic chip-based optical frequency comb using soliton Cherenkov radiation. *Science* **351**, 357–360. ISSN: 0036-8075, 1095-9203 (Jan. 22, 2016).
 55. Rowland, D. R. & Love, J. D. Evanescent wave coupling of whispering gallery modes of a dielectric cylinder. *IEE Proceedings J (Optoelectronics)* **140**, 177–188. ISSN: 2053-9088 (June 1, 1993).
 56. Gorodetsky, M. L. & Ilchenko, V. S. High-Q optical whispering-gallery microresonators: precession approach for spherical mode analysis and emission patterns with prism couplers. *Optics Communications* **113**, 133–143. ISSN: 0030-4018 (Dec. 15, 1994).
 57. Gorodetsky, M. L. & Ilchenko, V. S. Optical microsphere resonators: optimal coupling to high-Q whispering-gallery modes. *JOSA B* **16**, 147–154. ISSN: 1520-8540 (Jan. 1, 1999).
 58. Knight, J. C., Cheung, G., Jacques, F. & Birks, T. A. Phase-matched excitation of whispering-gallery-mode resonances by a fiber taper. *Optics Letters* **22**, 1129–1131. ISSN: 1539-4794 (Aug. 1, 1997).

Bibliography

59. Pfeiffer, M. H. P., Liu, J., Geiselmann, M. & Kippenberg, T. J. Coupling Ideality of Integrated Planar High- Q Microresonators. *Physical Review Applied* **7**. ISSN: 2331-7019 (Feb. 24, 2017).
60. Zhu, J., Özdemir, Ş. K., He, L. & Yang, L. Controlled manipulation of mode splitting in an optical microcavity by two Rayleigh scatterers. *Optics Express* **18**, 23535. ISSN: 1094-4087 (Nov. 8, 2010).
61. Shang, Y.-L., Ye, M.-Y. & Lin, X.-M. Experimental observation of Fano-like resonance in a whispering-gallery-mode microresonator in aqueous environment. *Photonics Research* **5**, 119–123. ISSN: 2327-9125 (Apr. 1, 2017).
62. Yang, K. Y., Beha, K., Cole, D. C., Yi, X., Del’Haye, P., Lee, H., Li, J., Oh, D. Y., Diddams, S. A., Papp, S. B. & Vahala, K. J. Broadband dispersion-engineered microresonator on a chip. *Nature Photonics* **10**, 316–320. ISSN: 1749-4893 (May 2016).
63. Turner, A. C., Manolatou, C., Schmidt, B. S., Lipson, M., Foster, M. A., Sharping, J. E. & Gaeta, A. L. Tailored anomalous group-velocity dispersion in silicon channel waveguides. *Optics Express* **14**, 4357–4362. ISSN: 1094-4087 (May 15, 2006).
64. Okamoto, K. *Fundamentals of optical waveguides* 2nd ed. 561 pp. ISBN: 978-0-12-525096-2 (Elsevier, Amsterdam ; Boston, 2006).
65. Tan, D. T. H., Ikeda, K., Sun, P. C. & Fainman, Y. Group velocity dispersion and self phase modulation in silicon nitride waveguides. *Applied Physics Letters* **96**, 061101. ISSN: 0003-6951 (Feb. 8, 2010).
66. Boggio, J. M. C., Bodenmüller, D., Fremberg, T., Haynes, R., Roth, M. M., Eisermann, R., Lisker, M., Zimmermann, L. & Böhm, M. Dispersion engineered silicon nitride waveguides by geometrical and refractive-index optimization. *JOSA B* **31**, 2846–2857. ISSN: 1520-8540 (Nov. 1, 2014).
67. Pfeiffer, M. H. P., Kordts, A., Brasch, V., Zervas, M., Geiselmann, M., Jost, J. D. & Kippenberg, T. J. Photonic Damascene process for integrated high-Q microresonator based nonlinear photonics. *Optica* **3**, 20. ISSN: 2334-2536 (Jan. 2016).
68. Fujii, S. & Tanabe, T. Dispersion engineering and measurement of whispering gallery mode microresonator for Kerr frequency comb generation. *Nanophotonics* **9**, 1087–1104. ISSN: 2192-8614 (May 2020).
69. Zhang, L., Yue, Y., Beausoleil, R. G. & Willner, A. E. Analysis and engineering of chromatic dispersion in silicon waveguide bends and ring resonators. *Optics Express* **19**, 8102. ISSN: 1094-4087 (Apr. 2011).
70. Anderson, M. H., Weng, W., Lihachev, G., Tikan, A., Liu, J. & Kippenberg, T. J. Zero dispersion Kerr solitons in optical microresonators. *Nature Communications* **13**, 4764. ISSN: 2041-1723 (Aug. 2022).

71. Ramelow, S., Farsi, A., Clemmen, S., Levy, J. S., Johnson, A. R., Okawachi, Y., Lamont, M. R. E., Lipson, M. & Gaeta, A. L. Strong polarization mode coupling in microresonators. *Optics Letters* **39**, 5134–5137. ISSN: 1539-4794 (Sept. 1, 2014).
72. Li, Y., Li, J., Huo, Y., Chen, M., Yang, S. & Chen, H. Spatial-mode-coupling-based dispersion engineering for integrated optical waveguide. *Optics Express* **26**, 2807–2816. ISSN: 1094-4087 (Feb. 5, 2018).
73. Lu, X., Rogers, S., Jiang, W. C. & Lin, Q. Selective engineering of cavity resonance for frequency matching in optical parametric processes. *Applied Physics Letters* **105**, 151104. ISSN: 0003-6951, 1077-3118 (Oct. 2014).
74. Yu, S.-P., Cole, D. C., Jung, H., Moille, G. T., Srinivasan, K. & Papp, S. B. Spontaneous pulse formation in edgeless photonic crystal resonators. *Nature Photonics* **15**, 461–467. ISSN: 1749-4893 (June 2021).
75. Helgason, Ó. B., Arteaga-Sierra, F. R., Ye, Z., Twayana, K., Andrekson, P. A., Karlsson, M., Schröder, J. & Victor Torres-Company. Dissipative solitons in photonic molecules. *Nature Photonics* **15**, 305–310. ISSN: 1749-4893 (Apr. 2021).
76. Ji, Q.-X., Jin, W., Wu, L., Yu, Y., Yuan, Z., Zhang, W., Gao, M., Li, B., Wang, H., Xiang, C., Guo, J., Feshali, A., Paniccia, M., Ilchenko, V. S., Matsko, A. B., Bowers, J. E. & Vahala, K. J. Engineered zero-dispersion microcombs using CMOS-ready photonics. *Optica* **10**, 279–285. ISSN: 2334-2536 (Feb. 20, 2023).
77. Kim, S., Han, K., Wang, C., Jaramillo-Villegas, J. A., Xue, X., Bao, C., Xuan, Y., Leaird, D. E., Weiner, A. M. & Qi, M. Dispersion engineering and frequency comb generation in thin silicon nitride concentric microresonators. *Nature Communications* **8**, 372. ISSN: 2041-1723 (Dec. 2017).
78. Kim, B. Y., Okawachi, Y., Jang, J. K., Yu, M., Ji, X., Zhao, Y., Joshi, C., Lipson, M. & Gaeta, A. L. Turn-key, high-efficiency Kerr comb source. *Optics Letters* **44**, 4475. ISSN: 0146-9592, 1539-4794 (Sept. 2019).
79. Xue, X., Xuan, Y., Wang, P.-H., Liu, Y., Leaird, D. E., Qi, M. & Weiner, A. M. Normal-dispersion microcombs enabled by controllable mode interactions. *Laser & Photonics Reviews* **9**, L23–L28. ISSN: 1863-8899 (2015).
80. Lucas, E., Yu, S.-P., Briles, T. C., Carlson, D. R. & Papp, S. B. Tailoring microcombs with inverse-designed, meta-dispersion microresonators. *Nature Photonics* **17**, 943–950. ISSN: 1749-4893 (Nov. 2023).
81. Moille, G., Lu, X., Stone, J., Westly, D. & Srinivasan, K. Fourier synthesis dispersion engineering of photonic crystal microrings for broadband frequency combs. *Communications Physics* **6**, 1–11. ISSN: 2399-3650 (June 19, 2023).
82. Boyd, R. W. *Nonlinear optics* Fourth edition. ISBN: 978-0-323-85057-5 (Academic Press, an imprint of Elsevier, London, United Kingdom, 2020).

Bibliography

83. Chembo, Y. K. & Menyuk, C. R. Spatiotemporal Lugiato-Lefever formalism for Kerr-comb generation in whispering-gallery-mode resonators. *Physical Review A* **87**. ISSN: 1050-2947, 1094-1622 (May 31, 2013).
84. Hansson, T., Modotto, D. & Wabnitz, S. On the numerical simulation of Kerr frequency combs using coupled mode equations. *Optics Communications* **312**, 134–136. ISSN: 0030-4018 (Feb. 1, 2014).
85. Ikeda, K. Multiple-valued stationary state and its instability of the transmitted light by a ring cavity system. *Optics Communications* **30**, 257–261. ISSN: 0030-4018 (Aug. 1979).
86. Leo, F., Gelens, L., Emplit, P., Haelterman, M. & Coen, S. Dynamics of one-dimensional Kerr cavity solitons. *Optics Express* **21**, 9180. ISSN: 1094-4087 (2013).
87. Godey, C., Balakireva, I. V., Coillet, A. & Chembo, Y. K. Stability analysis of the spatiotemporal Lugiato-Lefever model for Kerr optical frequency combs in the anomalous and normal dispersion regimes. *Physical Review A: Atomic, Molecular, and Optical Physics* **89**, 063814. ISSN: 1050-2947, 1094-1622 (June 2014).
88. Lugiato, L. A. & Lefever, R. Spatial Dissipative Structures in Passive Optical Systems. *Physical Review Letters* **58**, 2209–2211 (May 25, 1987).
89. Castelli, F., Brambilla, M., Gatti, A., Prati, F. & Lugiato, L. A. The LLE, pattern formation and a novel coherent source. *The European Physical Journal D* **71**, 84. ISSN: 1434-6060, 1434-6079 (2017).
90. Lugiato, L. A., Prati, F., Gorodetsky, M. L. & Kippenberg, T. J. *From the lugiato–Lefever equation to microresonator-based soliton kerr frequency combs* Dec. 2018.
91. Haelterman, M., Trillo, S. & Wabnitz, S. Dissipative modulation instability in a nonlinear dispersive ring cavity. *Optics Communications* **91**, 401–407. ISSN: 0030-4018 (1992).
92. Barashenkov, I. V. & Smirnov, Y. S. Existence and stability chart for the ac-driven, damped nonlinear Schrödinger solitons. *Physical Review E* **54**, 5707–5725 (Nov. 1, 1996).
93. Obrzud, E., Lecomte, S. & Herr, T. Temporal solitons in microresonators driven by optical pulses. *Nature Photonics* **11**, 600–607. ISSN: 1749-4893 (Sept. 2017).
94. Anderson, M. H., Bouchand, R., Liu, J., Weng, W., Obrzud, E., Herr, T. & Kippenberg, T. J. Photonic chip-based resonant supercontinuum via pulse-driven Kerr microresonator solitons. *Optica* **8**, 771–779. ISSN: 2334-2536 (June 20, 2021).
95. Matsko, A. B., Savchenkov, A. A., Strekalov, D., Ilchenko, V. S. & Maleki, L. Optical hyperparametric oscillations in a whispering-gallery-mode resonator: Threshold and phase diffusion. *Physical Review A* **71**, 033804 (2005).

96. Chembo, Y. K. & Yu, N. Modal expansion approach to optical-frequency-comb generation with monolithic whispering-gallery-mode resonators. *Physical Review A* **82**, 033801. ISSN: 1050-2947, 1094-1622 (Sept. 7, 2010).
97. Chembo, Y. K., Strekalov, D. V. & Yu, N. Spectrum and Dynamics of Optical Frequency Combs Generated with Monolithic Whispering Gallery Mode Resonators. *Physical Review Letters* **104**, 103902. ISSN: 0031-9007, 1079-7114 (Mar. 2010).
98. **Wildi, T.**, Gaafar, M. A., Voumard, T., Ludwig, M. & Herr, T. Dissipative Kerr Solitons in Integrated Fabry–Perot Microresonators. *Optica* **10**, 650–656. ISSN: 2334-2536 (June 2023).
99. Zakharov, V. E. & Ostrovsky, L. A. Modulation instability: The beginning. *Physica D: Nonlinear Phenomena* **238**, 540–548. ISSN: 0167-2789 (Mar. 2009).
100. Kippenberg, T. J., Spillane, S. M. & Vahala, K. J. Kerr-Nonlinearity Optical Parametric Oscillation in an Ultrahigh- Q Toroid Microcavity. *Physical Review Letters* **93**, 083904. ISSN: 0031-9007, 1079-7114 (Aug. 2004).
101. Hansson, T., Modotto, D. & Wabnitz, S. Dynamics of the modulational instability in microresonator frequency combs. *Physical Review A: Atomic, Molecular, and Optical Physics* **88**, 023819. ISSN: 1050-2947, 1094-1622 (Aug. 2013).
102. Pfeifle, J., Coillet, A., Henriot, R., Saleh, K., Schindler, P., Weimann, C., Freude, W., Balakireva, I. V., Larger, L., Koos, C. & Chembo, Y. K. Optimally Coherent Kerr Combs Generated with Crystalline Whispering Gallery Mode Resonators for Ultrahigh Capacity Fiber Communications. *Physical Review Letters* **114**, 093902 (Mar. 2015).
103. Ferdous, F., Miao, H., Leaird, D. E., Srinivasan, K., Wang, J., Chen, L., Varghese, L. T. & Weiner, A. M. Spectral line-by-line pulse shaping of on-Chip microresonator frequency combs. *Nature Photonics* **5**, 770–776. ISSN: 1749-4885, 1749-4893 (Dec. 2011).
104. Pfeifle, J., Brasch, V., Lauermann, M., Yu, Y., Wegner, D., Herr, T., Hartinger, K., Schindler, P., Li, J., Hillerkuss, D., Schmogrow, R., Weimann, C., Holzwarth, R., Freude, W., Leuthold, J., Kippenberg, T. J. & Koos, C. Coherent terabit communications with microresonator Kerr frequency combs. *Nature Photonics* **8**, 375–380. ISSN: 1749-4893 (May 2014).
105. Coulibaly, S., Taki, M., Bendahmane, A., Millot, G., Kibler, B. & Clerc, M. G. Turbulence-Induced Rogue Waves in Kerr Resonators. *Physical Review X* **9**, 011054. ISSN: 2160-3308 (2019).
106. Papp, S. B. & Diddams, S. A. Spectral and temporal characterization of a fused-quartz-microresonator optical frequency comb. *Physical Review A: Atomic, Molecular, and Optical Physics* **84**, 053833. ISSN: 1050-2947, 1094-1622 (Nov. 2011).

Bibliography

107. Li, J., Lee, H., Chen, T. & Vahala, K. J. Low-Pump-Power, Low-Phase-Noise, and Microwave to Millimeter-Wave Repetition Rate Operation in Microcombs. *Physical Review Letters* **109**, 233901. ISSN: 0031-9007, 1079-7114 (Dec. 2012).
108. Griffith, A. G., Yu, M., Okawachi, Y., Cardenas, J., Mohanty, A., Gaeta, A. L. & Lipson, M. Coherent mid-infrared frequency combs in silicon-microresonators in the presence of Raman effects. *Optics Express* **24**, 13044. ISSN: 1094-4087 (June 13, 2016).
109. *Dissipative solitons* (eds Akhmediev, N. N. & Ankiewicz, A.) (Springer, Berlin ; New York, 2005). ISBN: 978-3-540-23373-2.
110. Kippenberg, T. J., Gaeta, A. L., Lipson, M. & Gorodetsky, M. L. Dissipative Kerr solitons in optical microresonators. *Science* **361**, eaan8083. ISSN: 0036-8075, 1095-9203 (Aug. 10, 2018).
111. Wabnitz, S. Suppression of interactions in a phase-locked soliton optical memory. *Optics Letters* **18**, 601. ISSN: 0146-9592, 1539-4794 (Apr. 1993).
112. Leo, F., Coen, S., Kockaert, P., Gorza, S.-P., Emplit, P. & Haelterman, M. Temporal cavity solitons in one-dimensional Kerr media as bits in an all-optical buffer. *Nature Photonics* **4**, 471–476. ISSN: 1749-4893 (July 2010).
113. Engleburt, N., Mas Arabí, C., Parra-Rivas, P., Gorza, S.-P. & Leo, F. Temporal solitons in a coherently driven active resonator. *Nature Photonics* **15**, 536–541. ISSN: 1749-4893 (July 2021).
114. Guo, H., Karpov, M., Lucas, E., Kordts, A., Pfeiffer, M. H. P., Brasch, V., Lihachev, G., Lobanov, V. E., Gorodetsky, M. L. & Kippenberg, T. J. Universal dynamics and deterministic switching of dissipative Kerr solitons in optical microresonators. *Nature Physics* **13**, 94–102. ISSN: 1745-2481 (Jan. 2017).
115. Wang, J., Chen, D., Cai, H., Wei, F. & Qu, R. Fast optical frequency sweeping using voltage controlled oscillator driven single sideband modulation combined with injection locking. *Optics Express* **23**, 7038–7043. ISSN: 1094-4087 (Mar. 23, 2015).
116. Yi, X., Yang, Q.-F., Yang, K. Y., Suh, M.-G. & Vahala, K. Soliton frequency comb at microwave rates in a high-Q silica microresonator. *Optica* **2**, 1078–1085. ISSN: 2334-2536 (Dec. 2015).
117. Brasch, V., Geiselmann, M., Pfeiffer, M. H. P. & Kippenberg, T. J. Bringing short-lived dissipative Kerr soliton states in microresonators into a steady state. *Optics Express* **24**, 29312–29320. ISSN: 1094-4087 (Dec. 12, 2016).
118. Joshi, C., Jang, J. K., Luke, K., Ji, X., Miller, S. A., Klenner, A., Okawachi, Y., Lipson, M. & Gaeta, A. L. Thermally controlled comb generation and soliton mode-locking in microresonators. *Optics Letters* **41**, 2565. ISSN: 0146-9592, 1539-4794 (June 1, 2016).

119. Stern, B., Ji, X., Okawachi, Y., Gaeta, A. L. & Lipson, M. Battery-operated integrated frequency comb generator. *Nature* **562**, 401. ISSN: 1476-4687 (Oct. 2018).
120. Dutt, A., Joshi, C., Ji, X., Cardenas, J., Okawachi, Y., Luke, K., Gaeta, A. L. & Lipson, M. On-chip dual-comb source for spectroscopy. *Science Advances* **4**, e1701858 (Mar. 2, 2018).
121. Zhang, S., Silver, J. M., Bino, L. D., Copie, F., Woodley, M. T. M., Ghalanos, G. N., Svela, A. Ø., Moroney, N. & Del’Haye, P. Sub-milliwatt-level microresonator solitons with extended access range using an auxiliary laser. *Optica* **6**, 206–212. ISSN: 2334-2536 (Feb. 20, 2019).
122. **Wildi, T.**, Brasch, V., Liu, J., Kippenberg, T. J. & Herr, T. Thermally Stable Access to Microresonator Solitons via Slow Pump Modulation. *Optics Letters* **44**, 4447. ISSN: 0146-9592, 1539-4794 (Sept. 2019).
123. Vasil’ev, V. V., Velichansky, V. L., Gorodetskii, M. L., Il’chenko, V. S., Holberg, L. & Yarovitsky, A. V. High-coherence diode laser with optical feedback via a microcavity with ‘whispering gallery’ modes. *Quantum Electronics* **26**, 657. ISSN: 1063-7818 (Aug. 31, 1996).
124. Liang, W., Ilchenko, V. S., Savchenkov, A. A., Matsko, A. B., Seidel, D. & Maleki, L. Whispering-gallery-mode-resonator-based ultranarrow linewidth external-cavity semiconductor laser. *Optics Letters* **35**, 2822–2824. ISSN: 1539-4794 (Aug. 15, 2010).
125. Kondratiev, N. M., Lobanov, V. E., Cherenkov, A. V., Voloshin, A. S., Pavlov, N. G., Koptyaev, S. & Gorodetsky, M. L. Self-injection locking of a laser diode to a high-Q WGM microresonator. *Optics Express* **25**, 28167. ISSN: 1094-4087 (Nov. 13, 2017).
126. Ulanov, A. E., **Wildi, T.**, Bhatnagar, U. & Herr, T. *Laser Diode Self-Injection Locking to an Integrated High-Q Fabry-Pérot Microresonator* Aug. 2024. arXiv: [2408.08679](https://arxiv.org/abs/2408.08679) [physics].
127. Gorodetsky, M. L., Pryamikov, A. D. & Ilchenko, V. S. Rayleigh scattering in high-Q microspheres. *Journal of the Optical Society of America B: Optical Physics* **17**, 1051. ISSN: 0740-3224, 1520-8540 (June 2000).
128. Jin, W., Yang, Q.-F., Chang, L., Shen, B., Wang, H., Leal, M. A., Wu, L., Gao, M., Feshali, A., Paniccia, M., Vahala, K. J. & Bowers, J. E. Hertz-linewidth semiconductor lasers using CMOS-ready ultra-high-Q microresonators. *Nature Photonics* **15**, 346–353. ISSN: 1749-4885, 1749-4893 (May 2021).
129. Pavlov, N. G., Koptyaev, S., Lihachev, G. V., Voloshin, A. S., Gorodnitskiy, A. S., Ryabko, M. V., Polonsky, S. V. & Gorodetsky, M. L. Narrow-linewidth lasing and soliton Kerr microcombs with ordinary laser diodes. *Nature Photonics* **12**, 694–698. ISSN: 1749-4893 (Nov. 2018).

Bibliography

130. Raja, A. S., Voloshin, A. S., Guo, H., Agafonova, S. E., Liu, J., Gorodnitskiy, A. S., Karpov, M., Pavlov, N. G., Lucas, E., Galiev, R. R., Shitikov, A. E., Jost, J. D., Gorodetsky, M. L. & Kippenberg, T. J. Electrically pumped photonic integrated soliton microcomb. *Nature Communications* **10**, 680. ISSN: 2041-1723 (Feb. 8, 2019).
131. Shen, B., Chang, L., Liu, J., Wang, H., Yang, Q.-F., Xiang, C., Wang, R. N., He, J., Liu, T., Xie, W., Guo, J., Kinghorn, D., Wu, L., Ji, Q.-X., Kippenberg, T. J., Vahala, K. & Bowers, J. E. Integrated turnkey soliton microcombs. *Nature* **582**, 365–369. ISSN: 1476-4687 (June 2020).
132. Voloshin, A. S., Kondratiev, N. M., Lihachev, G. V., Liu, J., Lobanov, V. E., Dmitriev, N. Y., Weng, W., Kippenberg, T. J. & Bilenko, I. A. Dynamics of soliton self-injection locking in optical microresonators. *Nature Communications* **12**, 235. ISSN: 2041-1723 (Jan. 11, 2021).
133. Xiang, C., Liu, J., Guo, J., Chang, L., Wang, R. N., Weng, W., Peters, J., Xie, W., Zhang, Z., Riemensberger, J., Selvidge, J., Kippenberg, T. J. & Bowers, J. E. Laser soliton microcombs heterogeneously integrated on silicon. *Science* **373**, 99–103 (July 2021).
134. Ulanov, A. E., **Wildi, T.**, Pavlov, N. G., Jost, J. D., Karpov, M. & Herr, T. Synthetic Reflection Self-Injection-Locked Microcombs. *Nature Photonics*, 1–6. ISSN: 1749-4893 (Jan. 2024).
135. Lu, X., McClung, A. & Srinivasan, K. High-Q slow light and its localization in a photonic crystal microring. *Nature Photonics* **16**, 66–71. ISSN: 1749-4893 (Jan. 2022).
136. Black, J. A., Brodnik, G., Liu, H., Yu, S.-P., Carlson, D. R., Zang, J., Briles, T. C. & Papp, S. B. Optical-parametric oscillation in photonic-crystal ring resonators. *Optica* **9**, 1183. ISSN: 2334-2536 (Oct. 2022).
137. **Wildi, T.**^{*}, Ulanov, A.^{*}, Voumard, T., Ruhnke, B. & Herr, T. Phase-Stabilised Self-Injection-Locked Microcomb. *Nature Communications* **15**, 7030. ISSN: 2041-1723 (Aug. 2024).
138. Herr, T., Brasch, V., Jost, J. D., Mirgorodskiy, I., Lihachev, G., Gorodetsky, M. L. & Kippenberg, T. J. Mode Spectrum and Temporal Soliton Formation in Optical Microresonators. *Physical Review Letters* **113**, 123901 (Sept. 15, 2014).
139. Gaeta, A. L., Lipson, M. & Kippenberg, T. J. Photonic-chip-based frequency combs. *Nature Photonics* **13**, 158. ISSN: 1749-4893 (Mar. 2019).
140. Cole, D. C., Lamb, E. S., Del’Haye, P., Diddams, S. A. & Papp, S. B. Soliton crystals in Kerr resonators. *Nature Photonics* **11**, 671–676. ISSN: 1749-4893 (Oct. 2017).

141. Weng, W., Bouchand, R., Lucas, E., Obrzud, E., Herr, T. & Kippenberg, T. J. Heteronuclear soliton molecules in optical microresonators. *Nature Communications* **11**, 2402. ISSN: 2041-1723 (May 14, 2020).
142. Jang, J. K., Klenner, A., Ji, X., Okawachi, Y., Lipson, M. & Gaeta, A. L. Synchronization of coupled optical microresonators. *Nature Photonics* **12**, 688–693. ISSN: 1749-4893 (Nov. 2018).
143. Taheri, H., Matsko, A. B., Maleki, L. & Sacha, K. All-optical dissipative discrete time crystals. *Nature Communications* **13**, 848. ISSN: 2041-1723 (Feb. 14, 2022).
144. Marin-Palomo, P., Kemal, J. N., Karpov, M., Kordts, A., Pfeifle, J., Pfeiffer, M. H. P., Trocha, P., Wolf, S., Brasch, V., Anderson, M. H., Rosenberger, R., Vijayan, K., Freude, W., Kippenberg, T. J. & Koos, C. Microresonator-based solitons for massively parallel coherent optical communications. *Nature* **546**, 274–279. ISSN: 1476-4687 (June 2017).
145. Tan, M., Xu, X., Wu, J., Morandotti, R., Mitchell, A. & Moss, D. J. RF and microwave photonic temporal signal processing with Kerr micro-combs. *Advances in Physics: X* **6**, 1838946. ISSN: null (Jan. 1, 2021).
146. Trocha, P., Karpov, M., Ganin, D., Pfeiffer, M. H. P., Kordts, A., Wolf, S., Krockenberger, J., Marin-Palomo, P., Weimann, C., Randel, S., Freude, W., Kippenberg, T. J. & Koos, C. Ultrafast optical ranging using microresonator soliton frequency combs. *Science* **359**, 887–891. ISSN: 0036-8075, 1095-9203 (Feb. 23, 2018).
147. Suh, M.-G. & Vahala, K. J. Soliton microcomb range measurement. *Science* **359**, 884–887. ISSN: 0036-8075, 1095-9203 (Feb. 23, 2018).
148. Lucas, E., Brochard, P., Bouchand, R., Schilt, S., Südmeyer, T. & Kippenberg, T. J. Ultralow-noise photonic microwave synthesis using a soliton microcomb-based transfer oscillator. *Nature Communications* **11**, 374. ISSN: 2041-1723 (Jan. 17, 2020).
149. Suh, M.-G., Yang, Q.-F., Yang, K. Y., Yi, X. & Vahala, K. J. Microresonator soliton dual-comb spectroscopy. *Science* **354**, 600–603. ISSN: 0036-8075, 1095-9203 (Nov. 4, 2016).
150. Obrzud, E., Rainer, M., Harutyunyan, A., Anderson, M. H., Liu, J., Geiselmann, M., Chazelas, B., Kundermann, S., Lecomte, S., Cecconi, M., Ghedina, A., Molinari, E., Pepe, F., Wildi, F., Bouchy, F., Kippenberg, T. J. & Herr, T. A microphotonic astrocomb. *Nature Photonics* **13**, 31. ISSN: 1749-4893 (Jan. 2019).
151. Suh, M.-G., Yi, X., Lai, Y.-H., Leifer, S., Grudinin, I. S., Vasisht, G., Martin, E. C., Fitzgerald, M. P., Doppmann, G., Wang, J., Mawet, D., Papp, S. B., Diddams, S. A., Beichman, C. & Vahala, K. Searching for exoplanets using a microresonator astrocomb. *Nature Photonics* **13**, 25. ISSN: 1749-4893 (Jan. 2019).

Bibliography

152. Jang, J. K., Erkintalo, M., Murdoch, S. G. & Coen, S. Observation of dispersive wave emission by temporal cavity solitons. *Optics Letters* **39**, 5503–5506. ISSN: 1539-4794 (Oct. 1, 2014).
153. Bao, C. & Yang, C. Stretched cavity soliton in dispersion-managed Kerr resonators. *Physical Review A* **92**, 023802 (Aug. 3, 2015).
154. Dong, X., Yang, Q., Spiess, C., Bucklew, V. G. & Renninger, W. H. Stretched-Pulse Soliton Kerr Resonators. *Physical Review Letters* **125**, 033902 (July 17, 2020).
155. Turitsyn, S. K., Bogdanov, S. & Redyuk, A. Soliton-sinc optical pulses. *Optics Letters* **45**, 5352. ISSN: 0146-9592, 1539-4794 (Oct. 1, 2020).
156. Xue, X., Grelu, P., Yang, B., Wang, M., Li, S., Zheng, X. & Zhou, B. Dispersion-less Kerr solitons in spectrally confined optical cavities. *Light: Science & Applications* **12**, 19. ISSN: 2047-7538 (Jan. 9, 2023).
157. Zhang, S., Bi, T. & Del’Haye, P. Quintic Dispersion Soliton Frequency Combs in a Microresonator. *Laser & Photonics Reviews* **17**, 2300075. ISSN: 1863-8899 (2023).
158. Tikan, A., Riemensberger, J., Komagata, K., Hönl, S., Churaev, M., Skehan, C., Guo, H., Wang, R. N., Liu, J., Seidler, P. & Kippenberg, T. J. Emergent nonlinear phenomena in a driven dissipative photonic dimer. *Nature Physics* **17**, 604–610. ISSN: 1745-2481 (May 2021).
159. Szipöcs, R., Ferencz, K., Spielmann, C. & Krausz, F. Chirped multilayer coatings for broadband dispersion control in femtosecond lasers. *Optics Letters* **19**, 201–203. ISSN: 1539-4794 (Feb. 1, 1994).
160. Kärtner, F. X., Matuschek, N., Schibli, T., Keller, U., Haus, H. A., Heine, C., Morf, R., Scheuer, V., Tilsch, M. & Tschudi, T. Design and fabrication of double-chirped mirrors. *Optics Letters* **22**, 831–833. ISSN: 1539-4794 (June 1, 1997).
161. Braje, D., Hollberg, L. & Diddams, S. Brillouin-Enhanced Hyperparametric Generation of an Optical Frequency Comb in a Monolithic Highly Nonlinear Fiber Cavity Pumped by a cw Laser. *Physical Review Letters* **102**, 193902 (May 14, 2009).
162. Yu, S.-P., Jung, H., Briles, T. C., Srinivasan, K. & Papp, S. B. Photonic-Crystal-Reflector Nanoresonators for Kerr-Frequency Combs. *ACS Photonics* **6**, 2083–2089 (Aug. 21, 2019).
163. Ahn, G. H., Yang, K. Y., Trivedi, R., White, A. D., Su, L., Skarda, J. & Vučković, J. Photonic Inverse Design of On-Chip Microresonators. *ACS Photonics*, acsphotronics.2c00020. ISSN: 2330-4022, 2330-4022 (May 17, 2022).
164. Liu, J., Huang, G., Wang, R. N., He, J., Raja, A. S., Liu, T., Engelsen, N. J. & Kippenberg, T. J. High-yield, wafer-scale fabrication of ultralow-loss, dispersion-engineered silicon nitride photonic circuits. *Nature Communications* **12**, 2236. ISSN: 2041-1723 (Apr. 16, 2021).

165. Ji, X., Roberts, S., Corato-Zanarella, M. & Lipson, M. Methods to achieve ultra-high quality factor silicon nitride resonators. *APL Photonics* **6**, 071101. ISSN: 2378-0967 (July 1, 2021).
166. Palamaru, M. & Lalanne, P. Photonic crystal waveguides: Out-of-plane losses and adiabatic modal conversion. *Applied Physics Letters* **78**, 1466–1468. ISSN: 0003-6951 (Mar. 8, 2001).
167. Lalanne, P. & Hugonin, J. P. Bloch-wave engineering for high-Q, small-V microcavities. *IEEE Journal of Quantum Electronics* **39**, 1430–1438. ISSN: 1558-1713 (Nov. 2003).
168. Sauvan, C., Lecamp, G., Lalanne, P. & Hugonin, J. P. Modal-reflectivity enhancement by geometry tuning in Photonic Crystal microcavities. *Optics Express* **13**, 245–255. ISSN: 1094-4087 (Jan. 10, 2005).
169. Cole, D. C., Gatti, A., Papp, S. B., Prati, F. & Lugiato, L. Theory of Kerr frequency combs in Fabry-Perot resonators. *Physical Review A* **98**, 013831 (July 18, 2018).
170. Lobanov, V. E., Lihachev, G., Kippenberg, T. J. & Gorodetsky, M. L. Frequency combs and platicons in optical microresonators with normal GVD. *Optics Express* **23**, 7713–7721. ISSN: 1094-4087 (Mar. 23, 2015).
171. Xue, X., Xuan, Y., Liu, Y., Wang, P.-H., Chen, S., Wang, J., Leaird, D. E., Qi, M. & Weiner, A. M. Mode-locked dark pulse Kerr combs in normal-dispersion microresonators. *Nature Photonics* **9**, 594–600. ISSN: 1749-4893 (Sept. 2015).
172. Parra-Rivas, P., Gomila, D., Knobloch, E., Coen, S. & Gelens, L. Origin and stability of dark pulse Kerr combs in normal dispersion resonators. *Optics Letters* **41**, 2402–2405. ISSN: 1539-4794 (June 1, 2016).
173. Bruch, A. W., Liu, X., Surya, J. B., Zou, C.-L. & Tang, H. X. On-chip $\chi^{(2)}$ microring optical parametric oscillator. *Optica* **6**, 1361–1366. ISSN: 2334-2536 (Oct. 20, 2019).
174. Wolf, R., Jia, Y., Bonaus, S., Werner, C. S., Herr, S. J., Breunig, I., Buse, K. & Zappe, H. Quasi-phase-matched nonlinear optical frequency conversion in on-chip whispering galleries. *Optica* **5**, 872–875. ISSN: 2334-2536 (July 20, 2018).
175. Perego, A. M., Turitsyn, S. K. & Staliunas, K. Gain through losses in nonlinear optics. *Light: Science & Applications* **7**, 43. ISSN: 2047-7538 (Aug. 1, 2018).
176. Bale, B. G., Kutz, J. N., Chong, A., Renninger, W. H. & Wise, F. W. Spectral filtering for mode locking in the normal dispersive regime. *Optics Letters* **33**, 941. ISSN: 0146-9592, 1539-4794 (May 1, 2008).
177. Dong, X., Spiess, C., Bucklew, V. G. & Renninger, W. H. Chirped-pulsed Kerr solitons in the Lugiato-Lefever equation with spectral filtering. *Physical Review Research* **3**, 033252 (Sept. 15, 2021).

Bibliography

178. Haus, H. A. *Waves and fields in optoelectronics* 402 pp. ISBN: 978-0-13-946053-1 (Prentice-Hall, Englewood Cliffs, NJ, 1984).
179. Kippenberg, T. J., Holzwarth, R. & Diddams, S. A. Microresonator-Based Optical Frequency Combs. *Science* **332**, 555–559. ISSN: 0036-8075, 1095-9203 (Apr. 29, 2011).
180. Pasquazi, A., Peccianti, M., Razzari, L., Moss, D. J., Coen, S., Erkintalo, M., Chembo, Y. K., Hansson, T., Wabnitz, S., Del’Haye, P., Xue, X., Weiner, A. M. & Morandotti, R. Micro-combs: A novel generation of optical sources. *Physics Reports. Micro-combs: A novel generation of optical sources* **729**, 1–81. ISSN: 0370-1573 (Jan. 27, 2018).
181. Diddams, S. A., Vahala, K. & Udem, T. Optical frequency combs: Coherently uniting the electromagnetic spectrum. *Science* **369**. ISSN: 0036-8075, 1095-9203 (July 17, 2020).
182. Lilienfein, N., Hofer, C., Högner, M., Saule, T., Trubetskov, M., Pervak, V., Fill, E., Riek, C., Leitenstorfer, A., Limpert, J., Krausz, F. & Pupeza, I. Temporal solitons in free-space femtosecond enhancement cavities. *Nature Photonics* **13**, 214–218. ISSN: 1749-4885, 1749-4893 (Mar. 2019).
183. Jørgensen, A. A., Kong, D., Henriksen, M. R., Klejs, F., Ye, Z., Helgason, Ò. B., Hansen, H. E., Hu, H., Yankov, M., Forchhammer, S., Andrekson, P., Larsson, A., Karlsson, M., Schröder, J., Sasaki, Y., Aikawa, K., Thomsen, J. W., Morioka, T., Galili, M., Torres-Company, V. & Oxenløwe, L. K. Petabit-per-second data transmission using a chip-scale microcomb ring resonator source. *Nature Photonics* **16**, 798–802. ISSN: 1749-4893 (Nov. 2022).
184. Riemensberger, J., Lukashchuk, A., Karpov, M., Weng, W., Lucas, E., Liu, J. & Kippenberg, T. J. Massively parallel coherent laser ranging using a soliton microcomb. *Nature* **581**, 164–170. ISSN: 1476-4687 (May 2020).
185. Feldmann, J., Youngblood, N., Karpov, M., Gehring, H., Li, X., Stappers, M., Le Gallo, M., Fu, X., Lukashchuk, A., Raja, A. S., Liu, J., Wright, C. D., Sebastian, A., Kippenberg, T. J., Pernice, W. H. P. & Bhaskaran, H. Parallel convolutional processing using an integrated photonic tensor core. *Nature* **589**, 52–58. ISSN: 1476-4687 (Jan. 2021).
186. Taheri, H., Matsko, A. B. & Maleki, L. Optical lattice trap for Kerr solitons. *The European Physical Journal D* **71**, 153. ISSN: 1434-6079 (June 15, 2017).
187. Lu, Z., Chen, H.-J., Wang, W., Yao, L., Wang, Y., Yu, Y., Little, B. E., Chu, S. T., Gong, Q., Zhao, W., Yi, X., Xiao, Y.-F. & Zhang, W. Synthesized soliton crystals. *Nature Communications* **12**, 3179. ISSN: 2041-1723 (May 26, 2021).

188. Fortier, T. M., Kirchner, M. S., Quinlan, F., Taylor, J., Bergquist, J. C., Rosenband, T., Lemke, N., Ludlow, A., Jiang, Y., Oates, C. W. & Diddams, S. A. Generation of ultrastable microwaves via optical frequency division. *Nature Photonics* **5**, 425–429. ISSN: 1749-4893 (July 2011).
189. Papp, S. B., Del’Haye, P. & Diddams, S. A. Parametric seeding of a microresonator optical frequency comb. *Optics Express* **21**, 17615–17624. ISSN: 1094-4087 (July 29, 2013).
190. Taheri, H., Eftekhar, A. A., Wiesenfeld, K. & Adibi, A. Soliton Formation in Whispering-Gallery-Mode Resonators via Input Phase Modulation. *IEEE Photonics Journal* **7**, 1–9. ISSN: 1943-0655 (Apr. 2015).
191. Hansson, T. & Wabnitz, S. Bichromatically pumped microresonator frequency combs. *Physical Review A* **90**, 013811 (July 10, 2014).
192. Jang, J. K., Erkintalo, M., Coen, S. & Murdoch, S. G. Temporal tweezing of light through the trapping and manipulation of temporal cavity solitons. *Nature Communications* **6**, 7370. ISSN: 2041-1723 (June 24, 2015).
193. Erkintalo, M., Murdoch, S. G. & Coen, S. Phase and intensity control of dissipative Kerr cavity solitons. *Journal of the Royal Society of New Zealand* **52**, 149–167. ISSN: 0303-6758, 1175-8899 (Mar. 15, 2022).
194. Kim, B. Y., Jang, J. K., Okawachi, Y., Ji, X., Lipson, M. & Gaeta, A. L. Synchronization of nonsolitonic Kerr combs. *Science Advances* **7**, eabi4362 (Oct. 20, 2021).
195. Moille, G., Menyuk, C., Chembo, Y. K., Dutt, A. & Srinivasan, K. *Synthetic Frequency Lattices from an Integrated Dispersive Multi-Color Soliton* Oct. 17, 2022. arXiv: [2210.09036](https://arxiv.org/abs/2210.09036) [physics].
196. Del’Haye, P., Beha, K., Papp, S. B. & Diddams, S. A. Self-Injection Locking and Phase-Locked States in Microresonator-Based Optical Frequency Combs. *Physical Review Letters* **112**, 043905 (Jan. 29, 2014).
197. Taheri, H., Del’Haye, P., Eftekhar, A. A., Wiesenfeld, K. & Adibi, A. Self-synchronization phenomena in the Lugiato-Lefever equation. *Physical Review A* **96**, 013828 (July 14, 2017).
198. Wang, Y., Leo, F., Fatome, J., Erkintalo, M., Murdoch, S. G. & Coen, S. Universal mechanism for the binding of temporal cavity solitons. *Optica* **4**, 855–863. ISSN: 2334-2536 (Aug. 20, 2017).
199. Englebert, N., Simon, C., Arabí, C. M., Leo, F. & Gorza, S.-P. *Cavity Solitons Formation Above the Fundamental Limit Imposed by the Raman Self-frequency Shift* in *CLEO 2023 (2023)*, paper SW3G.3 CLEO: Science and Innovations (Optica Publishing Group, May 7, 2023), SW3G.3.

Bibliography

200. Taheri, H., Savchenkov, A. & Matsko, A. B. *Stable Kerr frequency combs excited in the vicinity of strong modal dispersion disruptions in Laser Resonators, Microresonators, and Beam Control XXV* Laser Resonators, Microresonators, and Beam Control XXV. **12407** (SPIE, Mar. 15, 2023), 35–43.
201. Suzuki, R., Fujii, S., Hori, A. & Tanabe, T. Theoretical Study on Dual-Comb Generation and Soliton Trapping in a Single Microresonator with Orthogonally Polarized Dual Pumping. *IEEE Photonics Journal* **11**, 1–11. ISSN: 1943-0655 (Feb. 2019).
202. Yang, Q.-F., Yi, X., Yang, K. Y. & Vahala, K. Counter-propagating solitons in microresonators. *Nature Photonics* **11**, 560–564. ISSN: 1749-4893 (Sept. 2017).
203. Yang, Q.-F., Shen, B., Wang, H., Tran, M., Zhang, Z., Yang, K. Y., Wu, L., Bao, C., Bowers, J., Yariv, A. & Vahala, K. Vernier spectrometer using counterpropagating soliton microcombs. *Science* **363**, 965–968 (Mar. 1, 2019).
204. Wang, Y., Yang, C. & Bao, C. Vernier Frequency Locking in Counterpropagating Kerr Solitons. *Physical Review Applied* **20**, 014015 (July 10, 2023).
205. Taheri, H., Matsko, A. B., Herr, T. & Sacha, K. Dissipative discrete time crystals in a pump-modulated Kerr microcavity. *Communications Physics* **5**, 1–10. ISSN: 2399-3650 (June 22, 2022).
206. Weng, W., Lucas, E., Lihachev, G., Lobanov, V. E., Guo, H., Gorodetsky, M. L. & Kippenberg, T. J. Spectral Purification of Microwave Signals with Disciplined Dissipative Kerr Solitons. *Physical Review Letters* **122**, 013902 (Jan. 3, 2019).
207. Brasch, V., Obrzud, E., Lecomte, S. & Herr, T. Nonlinear filtering of an optical pulse train using dissipative Kerr solitons. *Optica* **6**, 1386. ISSN: 2334-2536 (Nov. 20, 2019).
208. Karpov, M., Guo, H., Kordts, A., Brasch, V., Pfeiffer, M. H. P., Zervas, M., Geiselmann, M. & Kippenberg, T. J. Raman Self-Frequency Shift of Dissipative Kerr Solitons in an Optical Microresonator. *Physical Review Letters* **116**, 103902. ISSN: 0031-9007, 1079-7114 (Mar. 11, 2016).
209. Yi, X., Yang, Q.-F., Yang, K. Y. & Vahala, K. Theory and measurement of the soliton self-frequency shift and efficiency in optical microcavities. *Optics Letters* **41**, 3419. ISSN: 0146-9592, 1539-4794 (Aug. 1, 2016).
210. Adler, R. A Study of Locking Phenomena in Oscillators. *Proceedings of the IRE* **34**, 351–357. ISSN: 2162-6634 (June 1946).
211. Del’Haye, P., Arcizet, O., Gorodetsky, M. L., Holzwarth, R. & Kippenberg, T. J. Frequency comb assisted diode laser spectroscopy for measurement of microcavity dispersion. *Nature Photonics* **3**, 529–533. ISSN: 1749-4893 (Sept. 2009).

-
212. Matsko, A. B. & Maleki, L. Feshbach resonances in Kerr frequency combs. *Physical Review A* **91**, 013831. ISSN: 1050-2947, 1094-1622 (Jan. 22, 2015).
213. Lucas, E., Karpov, M., Guo, H., Gorodetsky, M. L. & Kippenberg, T. J. Breathing dissipative solitons in optical microresonators. *Nature Communications* **8**, 736. ISSN: 2041-1723 (Sept. 29, 2017).
214. Hadley, G. Injection locking of diode lasers. *IEEE Journal of Quantum Electronics* **22**, 419–426. ISSN: 1558-1713 (Mar. 1986).
215. Xue, X., Qi, M. & Weiner, A. M. Normal-dispersion microresonator Kerr frequency combs. *Nanophotonics* **5**, 244–262. ISSN: 2192-8614 (June 1, 2016).
216. Del’Haye, P., Papp, S. B. & Diddams, S. A. Hybrid Electro-Optically Modulated Microcombs. *Physical Review Letters* **109**, 263901. ISSN: 0031-9007, 1079-7114 (Dec. 26, 2012).
217. Kondratiev, N. M., Lobanov, V. E., Shitikov, A. E., Galiev, R. R., Chermoshentsev, D. A., Dmitriev, N. Y., Danilin, A. N., Lonshakov, E. A., Min’kov, K. N., Sokol, D. M., Cordette, S. J., Luo, Y.-H., Liang, W., Liu, J. & Bilenko, I. A. Recent advances in laser self-injection locking to high-Q microresonators. *Frontiers of Physics* **18**, 21305. ISSN: 2095-0470 (Mar. 7, 2023).
218. Xiang, C., Guo, J., Jin, W., Wu, L., Peters, J., Xie, W., Chang, L., Shen, B., Wang, H., Yang, Q.-F., Kinghorn, D., Paniccia, M., Vahala, K. J., Morton, P. A. & Bowers, J. E. High-performance lasers for fully integrated silicon nitride photonics. *Nature Communications* **12**, 6650. ISSN: 2041-1723 (Nov. 17, 2021).
219. Del’Haye, P., Arcizet, O., Schliesser, A., Holzwarth, R. & Kippenberg, T. J. Full Stabilization of a Microresonator-Based Optical Frequency Comb. *Physical Review Letters* **101**, 053903 (July 31, 2008).
220. Del’Haye, P., Coillet, A., Fortier, T., Beha, K., Cole, D. C., Yang, K. Y., Lee, H., Vahala, K. J., Papp, S. B. & Diddams, S. A. Phase-coherent microwave-to-optical link with a self-referenced microcomb. *Nature Photonics* **10**, 516–520. ISSN: 1749-4893 (Aug. 2016).
221. Briles, T. C., Stone, J. R., Drake, T. E., Spencer, D. T., Fredrick, C., Li, Q., Westly, D., Ilic, B. R., Srinivasan, K., Diddams, S. A. & Papp, S. B. Interlocking Kerr-microresonator frequency combs for microwave to optical synthesis. *Optics Letters* **43**, 2933. ISSN: 0146-9592, 1539-4794 (June 15, 2018).
222. Papp, S. B., Del’Haye, P. & Diddams, S. A. Mechanical Control of a Microrod-Resonator Optical Frequency Comb. *Physical Review X* **3**, 031003 (July 8, 2013).
223. Liu, J., Tian, H., Lucas, E., Raja, A. S., Lihachev, G., Wang, R. N., He, J., Liu, T., Anderson, M. H., Weng, W., Bhawe, S. A. & Kippenberg, T. J. Monolithic piezoelectric control of soliton microcombs. *Nature* **583**, 385–390. ISSN: 1476-4687 (July 2020).

Bibliography

224. Wang, J., Liu, K., Harrington, M. W., Rudy, R. Q. & Blumenthal, D. J. Silicon nitride stress-optic microresonator modulator for optical control applications. *Optics Express* **30**, 31816–31827. ISSN: 1094-4087 (Aug. 29, 2022).
225. He, Y., Lopez-Rios, R., Javid, U. A., Ling, J., Li, M., Xue, S., Vahala, K. & Lin, Q. High-speed tunable microwave-rate soliton microcomb. *Nature Communications* **14**, 3467. ISSN: 2041-1723 (June 12, 2023).
226. Papp, S. B., Beha, K., Del’Haye, P., Quinlan, F., Lee, H., Vahala, K. J. & Diddams, S. A. Microresonator frequency comb optical clock. *Optica* **1**, 10–14. ISSN: 2334-2536 (July 22, 2014).
227. Li, J., Yi, X., Lee, H., Diddams, S. A. & Vahala, K. J. Electro-optical frequency division and stable microwave synthesis. *Science* **345**, 309–313 (July 18, 2014).
228. Jost, J. D., Herr, T., Lecaplain, C., Brasch, V., Pfeiffer, M. H. P. & Kippenberg, T. J. Counting the cycles of light using a self-referenced optical microresonator. *Optica* **2**, 706–711. ISSN: 2334-2536 (Aug. 20, 2015).
229. Jost, J. D., Lucas, E., Herr, T., Lecaplain, C., Brasch, V., Pfeiffer, M. H. P. & Kippenberg, T. J. All-optical stabilization of a soliton frequency comb in a crystalline microresonator. *Optics Letters* **40**, 4723–4726. ISSN: 1539-4794 (Oct. 15, 2015).
230. Brasch, V., Lucas, E., Jost, J. D., Geiselmann, M. & Kippenberg, T. J. Self-referenced photonic chip soliton Kerr frequency comb. *Light: Science & Applications* **6**, e16202–e16202. ISSN: 2047-7538 (Jan. 2017).
231. Wu, K., O’Malley, N. P., Fatema, S., Wang, C., Girardi, M., Alshaykh, M. S., Ye, Z., Leaird, D. E., Qi, M., Torres-Company, V. & Weiner, A. M. Vernier microcombs for high-frequency carrier envelope offset and repetition rate detection. *Optica* **10**, 626–633. ISSN: 2334-2536 (May 20, 2023).
232. Moille, G., Stone, J., Chojnacky, M., Shrestha, R., Javid, U. A., Menyuk, C. & Srinivasan, K. Kerr-induced synchronization of a cavity soliton to an optical reference. *Nature* **624**, 267–274. ISSN: 1476-4687 (Dec. 2023).
233. Voumard, T., Darvill, J., **Wildi, T.**, Ludwig, M., Mohr, C., Hartl, I., Herr, T. & Herr, T. 1-GHz Dual-Comb Spectrometer with High Mutual Coherence for Fast and Broadband Measurements. *Optics Letters* **47**, 1379–1382. ISSN: 1539-4794 (Mar. 2022).
234. Gaafar, M. A., Ludwig, M., Wang, K., **Wildi, T.**, Voumard, T., Sinobad, M., Lorenzen, J., Francis, H., Carreira, J., Zhang, S., Bi, T., Del’Haye, P., Geiselmann, M., Singh, N., Kärtner, F. X., Garcia-Blanco, S. M. & Herr, T. Femtosecond Pulse Amplification on a Chip. *Nature Communications* **15**, 8109. ISSN: 2041-1723 (Sept. 16, 2024).

235. Carlson, D. R., Hickstein, D. D., Lind, A., Droste, S., Westly, D., Nader, N., Codrington, I., Newbury, N. R., Srinivasan, K., Diddams, S. A. & Papp, S. B. Self-referenced frequency combs using high-efficiency silicon-nitride waveguides. *Optics Letters* **42**, 2314–2317. ISSN: 1539-4794 (June 15, 2017).
236. Okawachi, Y., Yu, M., Desiatov, B., Kim, B. Y., Hansson, T., Lončar, M. & Gaeta, A. L. Chip-based self-referencing using integrated lithium niobate waveguides. *Optica* **7**, 702–707. ISSN: 2334-2536 (June 20, 2020).
237. Obrzud, E., Denis, S., Sattari, H., Choong, G., Kundermann, S., Dubochet, O., Despont, M., Lecomte, S., Ghadimi, A. H. & Brasch, V. Stable and compact RF-to-optical link using lithium niobate on insulator waveguides. *APL Photonics* **6**, 121303. ISSN: 2378-0967 (Dec. 7, 2021).
238. Riley, W. J. Handbook of Frequency Stability Analysis, 136 (2008).
239. Nardi, A., Davydova, A., Kuznetsov, N., Anderson, M. H., Möhl, C., Riemensberger, J., Seidler, P. & Kippenberg, T. J. *Soliton Microcomb Generation in a III-V Photonic Crystal Cavity* Apr. 27, 2023. arXiv: [2304.12968](https://arxiv.org/abs/2304.12968) [physics].
240. Campbell, G. N., Hill, L., Del’Haye, P. & Oppo, G.-L. Dark solitons in Fabry-Pérot resonators with Kerr media and normal dispersion. *Physical Review A* **108**, 033505 (Sept. 8, 2023).
241. Bunel, T., Conforti, M., Lumeau, J., Moreau, A. & Mussot, A. Broadband Kerr frequency comb in fiber Fabry-Perot resonators induced by switching waves. *Physical Review A* **109**, 063521. ISSN: 2469-9926, 2469-9934 (June 27, 2024).
242. Xiao, Z., Wu, K., Zhang, H., Li, T., Cai, M., Huang, Y. & Chen, J. Modeling the Kerr Comb of a Pulse Pumped F-P Microresonator With Normal Dispersion. *Journal of Lightwave Technology* **41**, 7408–7417. ISSN: 1558-2213 (Dec. 2023).
243. Ziani, Z., Bunel, T., Perego, A. M., Mussot, A. & Conforti, M. Theory of modulation instability in Kerr Fabry-Perot resonators beyond the mean-field limit. *Physical Review A* **109**, 013507 (Jan. 16, 2024).
244. Hill, L., Hirmer, E.-M., Campbell, G., Bi, T., Ghosh, A., Del’Haye, P. & Oppo, G.-L. Symmetry broken vectorial Kerr frequency combs from Fabry-Pérot resonators. *Communications Physics* **7**, 1–9. ISSN: 2399-3650 (Mar. 6, 2024).
245. Bunel, T., Conforti, M., Ziani, Z., Lumeau, J., Moreau, A., Fernandez, A., Llopis, O., Bourcier, G. & Mussot, A. 28 THz soliton frequency comb in a continuous-wave pumped fiber Fabry-Pérot resonator. *APL Photonics* **9**, 010804. ISSN: 2378-0967 (Jan. 25, 2024).
246. Ye, C., Liu, Y., Kim, C., Yvind, K. & Pu, M. *Singly-Resonant Four-Wave Mixing Based on an On-Chip Fabry-Perot Bragg Grating Cavity* in *2023 IEEE Photonics Conference (IPC) 2023 IEEE Photonics Conference (IPC)* (Nov. 2023), 1–2.

Bibliography

247. Zhou, L., Cheng, Y., Wang, B. & Zhang, W. *On-Chip Reconfigurable Silicon Photonic Fabry-Perot Resonator* in *2023 Asia Communications and Photonics Conference/2023 International Photonics and Optoelectronics Meetings (ACP/POEM)* 2023 Asia Communications and Photonics Conference/2023 International Photonics and Optoelectronics Meetings (ACP/POEM) (Nov. 2023), 1–4.
248. Musgrave, J., Huang, S.-W. & Nie, M. Microcombs in fiber Fabry–Pérot cavities. *APL Photonics* **8**, 121101. ISSN: 2378-0967 (Dec. 7, 2023).
249. Bi, T., Zhang, S., Ghosh, A., Lohse, O., Harder, I., Yang, K. Y. & Del’Haye, P. *On-Chip Inverse Designed Fabry-Pérot Resonators* in *2023 Conference on Lasers and Electro-Optics Europe & European Quantum Electronics Conference (CLEO/Europe-EQEC)* (IEEE, 2023), 1–1.
250. Yang, J., Guidry, M. A., Lukin, D. M., Yang, K. & Vučković, J. Inverse-designed silicon carbide quantum and nonlinear photonics. *Light: Science & Applications* **12**, 201. ISSN: 2047-7538 (Aug. 22, 2023).
251. Spektor, G., Zang, J., Dan, A., Briles, T. C., Brodник, G. M., Liu, H., Black, J. A., Carlson, D. R. & Papp, S. B. Photonic bandgap microcombs at 1064 nm. *APL Photonics* **9**, 021303. ISSN: 2378-0967 (Feb. 27, 2024).
252. Moille, G., Shandilya, P., Stone, J., Menyuk, C. & Srinivasan, K. *All-Optical Noise Quenching of An Integrated Frequency Comb* May 2, 2024. arXiv: [2405.01238](#) [physics].
253. Sun, S., Harrington, M. W., Tabatabaei, F., Hanifi, S., Liu, K., Wang, J., Wang, B., Yang, Z., Liu, R., Morgan, J. S., Bowers, S. M., Morton, P. A., Nelson, K. D., Beling, A., Blumenthal, D. J. & Yi, X. *Kerr optical frequency division with integrated photonics for stable microwave and mmWave generation* Feb. 18, 2024. arXiv: [2402.11772](#) [physics].
254. Moille, G., Shandilya, P., Niang, A., Menyuk, C., Carter, G. & Srinivasan, K. *Versatile Optical Frequency Division with Kerr-induced Synchronization at Tunable Microcomb Synthetic Dispersive Waves* Feb. 29, 2024. arXiv: [2403.00109](#) [physics].
255. Zhao, Y., Jang, J. K., Beals, G. J., McNulty, K. J., Ji, X., Okawachi, Y., Lipson, M. & Gaeta, A. L. All-optical frequency division on-chip using a single laser. *Nature* **627**, 546–552. ISSN: 1476-4687 (Mar. 2024).
256. Javid, U. A., Chojnacky, M., Srinivasan, K. & Moille, G. *Terahertz Voltage-controlled Oscillator from a Kerr-Induced Synchronized Soliton Microcomb* Apr. 25, 2024. arXiv: [2404.16597](#) [physics].

-
257. Moille, G., Javid, U. A., Chojnacky, M., Shandilya, P., Menyuk, C. & Srinivasan, K. *AC-Josephson Effect and Sub-Comb Mode-Locking in a Kerr-Induced Synchronized Cavity Soliton* Feb. 12, 2024. arXiv: [2402.08154](https://arxiv.org/abs/2402.08154)[physics].
258. Werle, P., Slemr, F., Maurer, K., Kormann, R., Mücke, R. & Jänker, B. Near- and mid-infrared laser-optical sensors for gas analysis. *Optics and Lasers in Engineering. Optical Methods in Earth Sciences* **37**, 101–114. ISSN: 0143-8166 (Feb. 1, 2002).
259. Wang, C. & Sahay, P. Breath Analysis Using Laser Spectroscopic Techniques: Breath Biomarkers, Spectral Fingerprints, and Detection Limits. *Sensors (Basel, Switzerland)* **9**, 8230–8262. ISSN: 1424-8220 (Oct. 19, 2009).
260. Werle, P. A review of recent advances in semiconductor laser based gas monitors. *Spectrochimica Acta Part A: Molecular and Biomolecular Spectroscopy* **54**, 197–236. ISSN: 1386-1425 (Feb. 1, 1998).
261. Ricci, L., Weidemüller, M., Esslinger, T., Hemmerich, A., Zimmermann, C., Vuletic, V., König, W. & Hänsch, T. W. A compact grating-stabilized diode laser system for atomic physics. *Optics Communications* **117**, 541–549. ISSN: 0030-4018 (June 15, 1995).
262. Sasada, H. & Yamada, K. Calibration lines of HCN in the 1.5-microm region. *Applied Optics* **29**, 3535–3547. ISSN: 1559-128X (Aug. 20, 1990).
263. Swann, W. C. & Gilbert, S. L. Line centers, pressure shift, and pressure broadening of 1530-1560 nm hydrogen cyanide wavelength calibration lines. *JOSA B* **22**, 1749–1756. ISSN: 1520-8540 (Aug. 1, 2005).
264. Hrabina, J., Hosek, M., Rerucha, S., Cizek, M., Pilat, Z., Zucco, M., Lazar, J. & Cip, O. Absolute frequencies of H¹³C¹⁴N hydrogen cyanide transitions in the 1.5- μ m region with the saturated spectroscopy and a sub-kHz scanning laser. *Optics Letters* **47**, 5704–5707. ISSN: 1539-4794 (Nov. 1, 2022).
265. Weiner, A. M., Heritage, J. P., Hawkins, R. J., Thurston, R. N., Kirschner, E. M., Leaird, D. E. & Tomlinson, W. J. Experimental Observation of the Fundamental Dark Soliton in Optical Fibers. *Physical Review Letters* **61**, 2445–2448. ISSN: 0031-9007 (Nov. 1988).